

STUDYING CLIMATE CHANGE, PRESENT GLACIER LANDSCAPES AND  
FUTURE LAKE FORMATION IN SWISS  
SOUTHWESTERN ALPS

by

Saeideh Gharehchahi, M.S.

A dissertation submitted to the Graduate Council of  
Texas State University in partial fulfillment  
of the requirements for the degree of  
Doctor of Philosophy  
with a Major in Geographic Information Science  
December 2019

Committee Members:

Jennifer L.R. Jensen, Chair

David R. Butler

Thomas J. Ballinger

Russel C. Weaver

Jan Klimeš

**COPYRIGHT**

by

Saeideh Gharehchahi

2019

## **FAIR USE AND AUTHOR'S PERMISSION STATEMENT**

### **Fair Use**

This work is protected by the Copyright Laws of the United States (Public Law 94-553, section 107). Consistent with fair use as defined in the Copyright Laws, brief quotations from this material are allowed with proper acknowledgement. Use of this material for financial gain without the author's express written permission is not allowed.

### **Duplication Permission**

As the copyright holder of this work I, Saeideh Gharehchahi, authorize duplication of this work, in whole or in part, for educational or scholarly purposes only.

## DEDICATION

Dedicated to my parents and my friends: David and Ann Womer, and Vida Khalilian!

ماحصل آموخته هایم را تقدیم می کنم به پدر و مادرم، به پاس موی سفیدشان،

و

دوستانم ویدا خلیلیان، دیوید وامر و همسرش، به پاس قلب های بزرگشان!

## ACKNOWLEDGEMENTS

I would like to express my gratitude to all my committee members, and Mrs. Allison Glass-Smith, who enduringly encouraged and supported me. My greatest thanks go to Dr. David Butler who accepted me as his PhD student at Texas State University and gave me this opportunity to study abroad. I am very grateful for having Dr. Jennifer Jensen, who wisely advised me through this challenging path, Dr. Russel Weaver who taught me statistical methods and supported me during my job applications, and Dr. Klimeš who gave us this honor to be part of the team. I also acknowledge the efforts and contributions of Dr. Thomas Ballinger who integrated my activities into his projects and helped me to develop my own research idea, which were essential for the success of this dissertation and the corresponding outcomes. The contribution of Drs. William James and Anshuman Bhardwaj to this work cannot be neglected as well. Last but not least, I am thankful for having the continued support of Dr. Thomas Larsen at the beginning of my academic job.

In addition, this work would not have been possible without the encouragement and fellow-feeling of friends at Texas State, Zoe Zell and Kenzie Maddison, Zahra Ghaffari, Dr. Francisco Zignol, Dr. Yunuen Reygadas-Langarica, Matthew Washburn, Dr. Niaz Morshed, Dr. Mark Deka, Mujahid Hussein, David Mills, Kate Landers, Mael Le Noc, Brandon Rose, David Szpakowski, Dr. Xujiao Wang, Drs. Maedeh Dabbaghian-Amiri and Javad Gatabi, Shadi Maleki, Dr. Chunhong Zhao, and other friends, Adeleh Aghaei and Azin Kamali-Rousta. I also appreciate the technical assistance of Mr. Charles Robinson during my analysis.

Above all, I am indebted to my family members, who have constantly supported me since I started my first grade and taught me all strong morals and work ethics. Any omission in this brief acknowledgement does not mean lack of gratitude.

## TABLE OF CONTENTS

	<b>Page</b>
ACKNOWLEDGEMENTS .....	v
LIST OF TABELS .....	viii
LIST OF FIGURES .....	x
LIST OF ABBREVIATIONS .....	xiii
ABSTRACT .....	xvi
CHAPTER	
1 INTRODUCTION .....	1
1.1 Background .....	1
1.2 Overall problem .....	4
1.3 Relevant theoretical basis .....	10
1.4 Research study area.....	16
1.5 Overall research objectives and questions.....	18
2 ANALYSIS OF SWISS GLACIER MASS BALANCE AND RESPONSE TO RECENT CLIMATE CHANGE AND REGIONAL ATMOSPHERIC CIRCULATION.....	20
2.1 Introduction .....	20
2.2 Case study .....	24
2.3 Data.....	28
2.4 Methodology .....	31
2.5 Results and discussion .....	36
2.6 Conclusions .....	57
3 GLACIER FACIES AND DEBRIS-COVERED SURFACES OF BERNESE ALPS – REMOTE SENSING APPLICATION: LANDSAT 8 OLI & TIRS .....	60
3.1 Introduction .....	60
3.2 Case study .....	63
3.3 Data and methodology .....	64

3.4 Results and discussion .....	67
3.5 Conclusion.....	75
<b>4 POTENTIAL SITES OF FUTURE LAKES IN SWISS SOUTHWESTERN ALPS WITH VOLTA .....</b>	<b>77</b>
4.1 Introduction .....	77
4.2 Case study .....	81
4.3 Data.....	82
4.4 Methodology .....	83
4.5 Results.....	86
4.6 Discussion .....	96
4.7 Conclusions .....	99
<b>5 SUMMARY &amp; LIMITATIONS.....</b>	<b>102</b>
5.1 Chapter 2 .....	102
5.2 Chapter 3 .....	103
5.3 Chapter 4 .....	104
5.4 Implications for hazard and risk management and future research.....	105
<b>REFERENCES .....</b>	<b>107</b>

## LIST OF TABELS

<b>Table</b>	<b>Page</b>
<b>Table 1-1</b> Main concepts in multi-hazard risk discipline. ....	9
<b>Table 2-1</b> Overview of the characteristics of selected glaciers in this study. ....	26
<b>Table 2-2</b> The magnitude of trends associated with the seasonal and annual glacier mass-balance trends in time series for common period 1970-2017. All values are significant at the 0.05 level. ....	38
<b>Table 2-3</b> Correlation matrix of $B_a$ for selected glaciers, values in bold are significant at the 0.01 level (for consistency I would put $p < 0.01$ instead of the 0.01 level). ....	39
<b>Table 2-4</b> Correlation coefficients of $B_a$ versus $B_w$ and $B_s$ , and values in bold are significant at the 0.01 level. ....	41
<b>Table 2-5</b> Mean and standard deviation of $B_a$ , $B_s$ , $B_w$ and AAR (%) in the common period 1970-2017. The significantly different values in each category are bolded. ....	42
<b>Table 2-6</b> Correlation (a, b) and multiple regression (c) coefficients of $B_a$ versus air temperature and precipitation of summer and winter seasons. a-c indicates significance at the 0.01, 0.05, and 0.10 levels, respectively. ....	48
<b>Table 2-7</b> Spearman correlation coefficients of $B_w$ , $B_s$ and $B_a$ versus seasonal and annual indices, a-b specifies the significance level of correlations at 0.05 and 0.10 levels, respectively. ....	50
<b>Table 2-8.</b> HI and glacier categories. ....	56
<b>Table 3-1</b> Details of Landsat 8 data. ....	64
<b>Table 3-2</b> Pixel ranges for mapping glacier surfaces. ....	74
<b>Table 4-1</b> Ice thickness classes and the corresponding area and ice volume resulted from VOLTA model and SGI2010. ....	88
<b>Table 4-2</b> Total area and volume of glaciers using different elevation models and outlines as input into the VOLTA model. The total volume of glaciers for the year of 2000 using ITEM is also included. ....	88
<b>Table 4-3</b> The glacier parameters including area ( $\text{km}^2$ ), elevation range ( $\Delta H$ (m)), mean slope ( $\alpha$ ( $^\circ$ )), for glaciers $> 5 \text{ km}^2$ located in Rhone catchment, and comparison of the individual glacier mean ice thickness ( $h_{\text{mean}}$ (m)), maximum ice thickness ( $h_{\text{max}}$ (m)) using VOLTA model with ITEM for SGI2000 outlines. ....	90

**Table 4-4** Modelled future lakes and their corresponding possibility based on the morphological criteria. The total area, volume and mean of depth for each possibility class is also calculated.....93

**Table 4-5** Mean ice thickness (m) for three glaciers using SGI2000 and three different models. ....97

## LIST OF FIGURES

Figure	Page
<b>Figure 1-1</b> The complex nonlinear dynamics vs. complexity and nonlinear dynamics (Phillips, 2003). .....	14
<b>Figure 1-2</b> A conceptual model of hazard interactions related to climate and geomorphic processes (modified from Gill, 2017). .....	16
<b>Figure 1-3</b> Rhone catchment is located in Valais canton, Switzerland. The investigated glaciers in this catchment are located within the Bernese (Fig 1-3a) and Valais (Fig 1-3b) Alps in the southwestern part of Switzerland (Source: SGI2010 and swissALT <sup>3D</sup> ). .....	17
<b>Figure 2-1</b> Overview maps of the research study area and the glaciers with mass balance measurements analyzed in this work (Google Earth imagery, DHM25/200) a) Grosser Altesch b) Gietro c) Hohlaub, Allalin, Schwarzberg (left to right) d) Gries e) Rhone f) Clariden g) Silvretta h) Rhone catchment.....	25
<b>Figure 2-2</b> Drastic ablation, reduction in elevation surface and width, that has occurred over the course of the 20th and into the 21st Century; 2009 picture taken by co-author D. Butler. ....	27
<b>Figure 2-3</b> Data coverage of annual mass balances ( $B_a$ ) for the selected glaciers from 1884 to 2017.....	29
<b>Figure 2-4</b> Estimates of the significant break dates (shown in crossed circles) for annual mass balance Swiss glaciers since starting date (see Fig 2-3). Each dashed line represents the time period of 95% confidence interval (Gries and Schwarzberg have experienced two structural changes). .....	38
<b>Figure 2-5</b> Annual mass balance of glaciers forecasted by Holt's exponential smoothing up to the year 2030. (*two glaciers outside the study area). .....	40
<b>Figure 2-6</b> A heatmap representation of the Spearman correlation matrix of $B_a$ and dendrogram of similar groups of glaciers associated to the Table 2-3 (group 1: Silvretta, Clariden, Gries and Gietro; group 2: Allalian, Schwarzberg and Hohlaub). The right bar shows the color code of coefficients corresponding to Spearman correlations. ....	40
<b>Figure 2-7</b> Number of days with the temperature above 0°C over the glaciers per year..	44
<b>Figure 2-8</b> Accumulation season (October- April) air temperature anomalies in a) southern Rhone (including Gietro, Hohlaub, Allalin, and Schwarzberg glaciers), c) northern Rhone (including Grosser Altesch, Gries, and Rhone glaciers), e) Silvretta, g)	

Clariden. Ablation season (May-Sep) air temperature anomalies in b) southern Rhone (including Gietro, Hohlaub, Allalin, and Schwarzberg glaciers), d) northern Rhone (including Grosser Altesch, Gries, and Rhone glaciers), f) Silvretta, h) Clariden .....	46
<b>Figure 2-9</b> October- April (winter) total precipitation anomalies in <b>a)</b> southern Rhone (including Gietro, Hohlaub, Allalin, and Schwarzberg glaciers), <b>c)</b> northern Rhone (including Grosser Altesch, Gries, and Rhone glaciers), <b>e)</b> Silvretta, <b>g)</b> Clariden. May-Sept (summer) total precipitation anomalies in <b>b)</b> southern Rhone (including Gietro, Hohlaub, Allalin, and Schwarzberg glaciers), <b>d)</b> northern Rhone (including Grosser Altesch, Gries, and Rhone glaciers), <b>f)</b> Silvretta, <b>h)</b> Clariden .....	47
<b>Figure 2-10</b> The relationship between the summer Atlantic Multidecadal Atlantic Ocean (AMO) (a) and annual East Atlantic (EA) (b) indices versus summer mass balance from 1970 to 2017, with strong correlations coefficients of -0.88 and -0.86 ( $p < 0.05$ ), respectively.....	51
<b>Figure 2-11</b> Comparable hypsometric profiles for all the glaciers. The colored boxes for each profile mark the ELA for the respective glacier. The dashed curves represent the two glaciers outside the Rhone catchment.....	53
<b>Figure 2-12.</b> The elevation maps of the selected glaciers. ....	55
<b>Figure 2-13.</b> Hypsometric curves of selected glaciers. ....	56
<b>Figure 3-1</b> The six selected glaciers of the Bernese Alps are located in Rhone catchment, southwestern Switzerland (Source: SGI 2010 and swissALT <sup>3D</sup> ). ....	63
<b>Figure 3-2</b> A flow chart of processing steps for mapping the glacier facies and debris cover area. ....	66
<b>Figure 3-3</b> An overview of the glacier facies a) Snow in accumulation area b) Crevasses/slush zone c) Clean ice d) Mixed ice with debris; and e) Debris-covered surface. ....	69
<b>Figure 3-4</b> Spatial profiles of Landsat 8 band 10, 6 and 1 for the selected glacier area (see Fig 3-3), the Y-axis shows the TOA reflectance of each pixel. ....	70
<b>Figure 3-5</b> a) Band 5, showing low reflectance, versus b) Band 6, showing high reflectance of debris-covered surfaces. ....	71
<b>Figure 3-6</b> Sequence in glacier facies (modified from Williams et al. 1991). ....	72
<b>Figure 3-7</b> Google Earth image of the western arm of Oberaletsch Glacier: a) Snow facies close to an arête in the accumulation zone, b) Crevasses over steep slopes turning clean snow into dark slush, c) Clean ice, d) Mix of ice and debris, e) Supraglacial debris cover with red arrow showing the position of ice wall at the tongue. ....	73

<b>Figure 3-8</b> b) The classified map with five surface types; a) Red ellipse shows a correct classification corresponding to the western arm of Oberaletsch Glacier (Fig 3-3); and b) shows misclassified snow class examples. ....	74
<b>Figure 4-1</b> Linear-log plot illustrating the relationship between the area of glaciers and the elevation bands within the Rhone catchment. ....	82
<b>Figure 4-2</b> Ice thickness distribution (a) and bed elevation (b) of glaciers using VOLTA model and SGI2010. ....	87
<b>Figure 4-3</b> Linear-log plot showing the relation between average ice thickness and area of glaciers. ....	89
<b>Figure 4-4</b> Profile of modelled beds (dashed line) and surfaces (solid line) of four large glaciers in Rhone catchment for the outlines of SGI2010. The inset map shows the location of these glaciers. ....	91
<b>Figure 4-5</b> The hypsometric curves of glacier mean ice thickness, area and volume for SGI 2010.....	92
<b>Figure 4-6</b> Morphological criteria that determines the possibility of sites for future lakes: a) the modelled overdeepenings over Mont Miné Glacier in Valais Alps using VOLTA and SGI2010, b) slope increase over the glacier direction, c) decrease in glacier width, and d) crevasses-free area followed by heavy crevasses formation (Frey et al. 2010; Colonia et al. 2017). ....	93
<b>Figure 4-7</b> Gorner glacier tongue, where the ice calving process has been initiated at the end (Source: Google Earth Imagery, 09/29/2016).....	94
<b>Figure 4-8</b> The spatial distribution of overdeepenings with the corresponding total volumes: a) Bernese Alps, b) Valais Alps.....	95
<b>Figure 4-9</b> The linear-log plot showing the distribution of mean volume of potential lakes against the corresponding areas for SGI2010.....	96

## LIST OF ABBREVIATIONS

<b>Abbreviation</b>	<b>Description</b>
AAR	Accumulation Area Ratio
AMO	Atlantic Multidecadal Oscillation
ACF	Autocorrelation Function
B <sub>a</sub>	Annual Mass Balance
B <sub>s</sub>	Summer Mass Balance
B <sub>w</sub>	Winter Mass Balance
CPC	Climatic Prediction Center
CUSUM	Cumulated Sum of Standard OLS residuals
DEM	Digital Elevation Model
DHM25	Digital Height Model 25
DNs	Digital Numbers
DTM	Digital Terrain Model
EA	East Atlantic
efp	Empirical Fluctuation Process
EOF	Empirical Orthogonal Function
GIS	Geographic Information System
GlabTop	Glacier Bed Topography
GLOFs	Glacier Lake Outburst Floods

GPR - Ground Penetrating Radar

GPS - Global Positioning System

GBI - Greenland Blocking Index

GTNG - Global Terrestrial Network for Glaciers

ITEM - Ice Thickness Estimation Method

IDNDR - International Decade of Natural Disaster Reduction

ISDR - International Strategy for Disaster Reduction

ITEM - Ice Thickness Estimation Method

VAW/ETHZ - Laboratory of Hydraulics, Hydrology and Glaciology at ETH Zürich

MSF - Modified Single Flow

MSS - Multi-Spectral Scanner

NIR- Near Infrared

NAO - North Atlantic Oscillation

$P_w$  - Winter Precipitation

OLI - Operational Land Imager

TIRS - Thermal Infrared Sensor

PACF - Partial Autocorrelation Function

SCA - Scandinavian Pattern

SST - Sea Surface Temperature

SLP - Sea-level Pressure

SRTM - Shuttle Radar Topography Mission

SWIR - Shortwave Infrared

SGI - Swiss Glacier Inventory

NBCN - Swiss National Basic Climatological Network

Ts - Summer Temperature

TOA - Top-Of-Atmosphere

VOLTA - Volume and Topography Automation

WGMS – World Glacier Monitoring Service

## ABSTRACT

Accelerated ice loss has been the most pronounced sign of climate change in high-mountain regions around the world. One of the outcomes of such changes is the formation of new lakes upon unstable slopes, a process that frequently observed in the Swiss Alps and poses threats to downstream settlements in the form of Glacier Lake Outburst Floods (GLOFs). Here, we first investigated the interactions between local meteorological variables, distant large-scale atmospheric and oceanic patterns, and glacier mass balance components to understand the response of the Swiss southwestern glaciers to observed climatic trends. The results show that all selected glaciers have lost their equilibrium condition in the recent decades with the persistent negative annual mass balance trends, and decreasing accumulation area ratios (AARs), accompanied by increasing air temperatures by  $+0.45^{\circ}\text{C decade}^{-1}$ , under the influence of Atlantic Multidecadal Oscillation (AMO), Greenland Blocking Index (GBI) and East Atlantic (EA) teleconnections. Forecasting results out to 2030 suggest that the smaller glaciers will continue to melt faster because of their inability to adjust to warming climate conditions as well as increases in long-wave heat input from the bare slopes. We also observed the current glacier landscapes and mapped the glacier facies and debris-covered surfaces using Landsat 8 OLI and TIRS data, which can eventually advance the accurate selection of future lake sites and associated hazards. With improvements in the spatial resolution of satellite images, and geomorphometry-related approaches, we could also estimate glacier ice thickness and simulate the glacier bed topography after glaciers decline. By linking three morphological criteria to the modelled overdeepenings over glacier bed topography, the possibility of these sites for future lake formation were determined. This study is a contribution to advance lake hazard management under the influence of climate change in high-mountain regions.

# **1 INTRODUCTION**

## **1.1 Background**

The term natural hazards refer to the incidence of any threatening condition from natural phenomenon in a spatial and temporal scale. About 790 million people dwelling on 3.8 million km<sup>2</sup>, are subject to more than one hazard (World Development Report 2010; Gallina et al. 2016). With ongoing climate change and global warming, dramatic losses and fatalities have increased in the last several decades and prompted international attention for new hazards and risk mitigation strategies. According to observations, atmospheric CO<sub>2</sub> concentrations have reached 408.53 ppm, correlating with an increase in global temperature up to 2.3°C, with a mean 0.8°C increase since preindustrial times (US Department of Commerce 2019). There is general agreement that this warming process leads to wetter climates, which increases the number of extreme events. The Northern Hemisphere has experienced an increase in annual maximum daily rainfall amounts, and corresponding snow cover decreases of 1.6 percent per decade for March and April, and 11.7 percent per decade for June, since 1967 (IPCC 2013). Projections also indicate that spring snow cover will decrease by 7 to 25 percent throughout the 21st century (IPCC 2013). The consequences of such changes will result in a wide range of environmental impacts including alteration of hazards' behavior. The perturbation in magnitude and frequency of hazards arising from climate change are likely to alter the spatial and temporal distribution of hazards and increase the exposure to multi-hazard events.

From a systematic approach, hazards are triggered from geological and hydro-meteorological components of the Earth's surface systems. Since these hazards are influenced by climate change, and can disturb land-surface processes and landform

stability, they also need to be considered and analyzed in an integrated framework from both geomorphic and hydro-meteorological perspectives (Alcántara-Ayala and Goudie 2010). A geomorphic hazard is, therefore, the result of any change in land-surface features that adversely influences the stability of landforms in combination with impacts to human assets and socio-economic systems.

Some geomorphic systems are susceptible to more than one hazard and respond faster to any environmental changes, like 'geomorphological hotspots' (Goudie 1996). These geosystems are sensitive to the exceedance of critical thresholds because they can only exist under certain climatic conditions. For example, if temperature crosses the 0°C threshold, it will cause degradation of permafrost, glaciers, and ice caps, which eventually alter the related processes and interlinkages and can eventually lead to the imbalance of corresponding geosystems. In this era, climate change is likely to accelerate the exposure of these areas to multiple hazards by affecting soil moisture, retreating permafrost and snow lines, rising sea level, and consequently landform instability. Since these areas recover very slowly from such impacts, it is important to assess and monitor them closely from a holistic view.

Due to different degrees of landscape sensitivity to the changes in interactions between landscape elements and processes, hazards cannot be assessed, investigated, and modeled individually anymore (Brunsden 2001). Despite well-established single hazard approaches, this consideration is rarely taken into account in the hazard literature (Gill and Malamud 2014; Gallina et al. 2016). Against this background, the need for a standard approach towards the multi-hazard risk assessment under the influence of recent climate change impacts and adaptation strategies have received special attention from international

organizations. On this subject, the concept of multi-hazard has been defined as “all potential hazards and their interrelationships, in a given spatial and temporal scale” (Gallina et al. 2016). However, with the dramatic ongoing progress and consequent changes in land use and climate, a dynamic perspective needs to be embedded in emerging frameworks for an accurate assessment of all related processes.

To understand the interlinkage between hazards under the influence of climate change and to bring them together under an integrated framework, it is critical to use Geographic Information Systems (GIS) and earth observation products to conduct hazard risk assessment studies. In recent decades, advancements in satellite remote sensing, GIS analysis techniques and Global Positioning System (GPS) for land surface mapping have guided data monitoring and warning system designs. Moreover, the application of GIS in solving environmental problems has been expanded and has facilitated hazard mitigation to identify stable landforms for human development (Gares et al. 1994). Hazard and risk studies are conducted at different scales, ranging from global to local extents. Depending on the research objectives, each of these scales requires its own data quality for varying components of hazard risk assessment including: different hazard inventories, environmental factors, trigger variables, risk exposure, and vulnerability. Additionally, spatial visualization of hazard assessment as a component of risk governance for the communication of results in an interactive manner between planners, engineers, managers, authorities, and the communities can only be addressed through web-based GIS tools. Therefore, due to the inherent spatial characteristics of each element in the process of hazard management, especially multiple hazards, GIS and remote sensing approaches are

the standard supportive tools that offer the advantage of using ‘what if’ to develop different possibilities if system variables change (Van Westen 2013).

## **1.2 Overall problem**

High mountain systems, specifically glaciers, are uniquely suitable demonstrations of climate change because of the intensification of climate feedbacks related to high-elevation snow cover, albedo, and water and energy budgets (Haeberli et al. 2007; Keiler et al. 2010). The volume of glaciers depends on the amount of snow that receives within the accumulation zone, the rate of mass loss due to melting within the ablation zone, and the characteristics of the underlying geology that can partly control the ice flow (Cuffey and Paterson 2010). The recent observations of glaciers around the world present a general retreat, which is associated with a global temperature increase (Ohmura 2011; Marzeion et al. 2014).

Due to the strong dependency of these environments on climate conditions at the ground–atmosphere interaction (Fuchs et al. 2013), small variations in this environment can result in slope processes change. These slope processes are very sensitive to temperature and precipitation change, where glacier shrinkage exposes a large amount of glacial sediment, rock walls, and deposits (Fernández and Mark 2016). The instability of such glacial environments has been increased by degradation of permafrost. More specifically, large quantities of destabilized, unconsolidated, unvegetated, ice-cored materials can be flushed out following a heavy rainfall event, snow and ice melt, or Glacier Lake Outburst Floods (GLOFs) to downstream landscapes (Clague 2000; Huggel et al. 2004; Anaconda et al. 2015).

The European Alps have shown strong evidence of responding to climate change, which makes them the best proxy for investigating climate controls on multiple hazards and their interactions. Stoffel et al. (2014) reported that over the last few decades, the change in spatial distribution of both snow and rainfall has impacted snow line elevation and duration in this region. It is projected that rain-on-snow events will become much more common and accelerate the glacier retreat in a warming climate. Therefore, any changes in the volume and extent of glaciers can lead to hydrological impacts since they influence the atmospheric circulation and the land surface temperature.

One of these impacts is the formation of new lakes, which are frequently being observed all over the world (Mergili et al. 2017). With warm winters and an increase in the ratio of rainfall on snow events, glacier-melting processes have been accelerated. This process consequently destabilizes ice cored moraine-dammed lakes, for which sudden draining can cause catastrophic floods and debris flows in downslope. Rapid mass movements like ice/rock avalanches are most likely to impact these lakes and cause the overtopping of the dams and lake depletion (Schaub et. al, 2015; Jawaid et. al, 2017). These cascading processes and the location of new lakes in such a dynamic environment can be problematic for downslope settlements and have serious socioeconomic impacts, especially in densely populated valleys.

The process chains from lakes have led to historic disasters in many high mountain regions worldwide. No systematic study examining prediction of lake outbursts was conducted until the dam failure of Lake Palcacoch in 1941 that killed 5,000 people and demolished one-third of Huaraz City in the Callejón de Huaylas, Peru (Carey 2010). The Cordillera Blanca in Peru is one of the largest tropical mountain ranges, consisting of 24%

of tropical ice mass (Schaub et al. 2015). These mountains have lost 30% of their glacier mass since the mid-19<sup>th</sup> century, which has resulted in new lake formations in deglaciated areas (Rabatel et al. 2013). The outburst floods in this area, which has a total human population of 267,000, have frequently been reported with extensive damage to properties. Examples include Lake Safuna Alta in 2002, which activated by a rock avalanche; Lake Palcacocha in 2003, which was triggered by a landslide and led to dam overtopping; and a flood from Lake 513 which was induced by an ice avalanche in 2010 (Mergili et al. 2017). The most recent event in the Cordillera Blanca was triggered by a landslide from a steep moraine wall into Lake Artizón Alto, and involved four other lakes in a process chain with entraining material through the Artizón and Santa Cruz valleys in 2012 (Mergili et al. 2017).

The temperate glaciers of Swiss Alps are also susceptible to similar catastrophic events and have been the focus of research since they are amongst the most densely populated high-mountain regions (Huggel et al. 2003). The total ice volume in this area was estimated to be  $74 \pm 9 \text{ km}^3$  in year 1999, from which about 12% was lost between 1999 and 2008 (Farinotti et al. 2009a). Therefore, the increase in the number of new lakes over the last three decades has been the result of glacier recession. From previous studies, it is also projected that the Swiss Alps will lose 75% of their ice by the middle of this century (Zemp et al. 2006; Linsbauer et al. 2013; Schaub et al., 2015), and new lakes will develop in the place of exposed overdeepenings. This will lead to a hazardous situation in active deglaciated areas, where the lakes are prone to rapid mass movement from instable dynamic slopes.

To reduce the arising risk in this area, understanding the high-mountain geosystem components, fundamentals of cascading hazards, and employing a new framework is required. Switzerland is one of the leading countries in taking risk-based measures towards hazards management instead of purely technical policies (Bischof, Romang, and Bründl 2009; Bründl et al. 2009). While attempts for developing an integrated risk management framework for glacier hazards have been already examined, they are still based on the current events with a static view of both natural and human systems.

With the development of the International Decade of Natural Disaster Reduction (IDNDR) and the following International Strategy for Disaster Reduction (ISDR), the concept of multi-hazard analysis was first introduced in the agenda of the 21 Conference in Rio de Janeiro and subsequently followed by the Johannesburg Plan (UN, 2002), which proposed a multi-hazard approach for disaster management and risk reduction (Gallina et al. 2016). Correspondingly, the initiatives for analyzing multiple risks, derived by multiple hazards, and the associated exposed elements at risk have widely increased over the last decade. Table 1 summarizes the main concepts in this emerging discipline. The IDNDR document also calls for an integrated multi-hazard approach to address the different components of risk and disaster management as a program for a safe and sustainable world in the twenty-first century.

In light of this, it is essential to have a holistic perspective of all hazards that pose a risk to environmental assets and communities. To address this new approach in hazard studies, Hewitt and Burton (1971) suggested a break point for related hazards based on the corresponding scale. In addition, the European Commission guidelines (2011) for risk assessment and mapping at a national scale suggested the consideration of only those

threats with the annual probability of greater 1%, and the significant potential impacts, i.e., affected more than 50 people, economic and environmental costs about € 100 million, and considerable political/social impacts.

In some areas, the integrated framework of two or more processes is imperative, such as when a hazard causes multiple hazards (i.e., earthquakes or floods that result in subsequent rapid mass movements). Further, this approach is necessary due to intrinsic characteristics of such processes. For instance, rapid mass movements from GLOFs have the potential to span large areas and convert into debris flow hazards or vice versa, in a sediment, hazard cascade (Butler 1989).

The approaches related to single hazards and processes have been adequately developed, while the methodology for integrating hazards in a joint scheme have not been well established. The main challenges for multi-hazard integrations can be categorized into four groups (Kappes et al. 2012b):

1. Hazards have different characteristics and behave differently, thus, they are not directly comparable.
2. Hazards are components of earth system and are not separated, but linked and connected. They can cause subsequent hazards or change the behavior of other hazards in another system. Therefore, single hazard values cannot be accumulated for overall-risk.
3. Since hazard behaviors differ, their degrees of impact on elements at risk differ as well.
4. It is a challenge to adapt quantitative methods from single hazard analysis and apply them for multi-hazard comparison.

**Table 1-1** Main concepts in multi-hazard risk discipline.

<b>Concept</b>	<b>Definition</b>	<b>Reference</b>
<b>Hazard</b>	Represents the threatening phenomenon arising from climate change impacts, which cause the damage and loss to human properties and environmental resources.	(Alcántara-Ayala and Goudie 2010; Kappes et al. 2012ab; Gallina et al. 2016)
<b>Multi-hazard</b>	Refers to: several hazardous events occurring in a given area with or without temporal coincidence, One process triggers the next one (cascade, coincidence) This concept considers all the relevant hazards in space and time.	(Kappes et al. 2012ab; Gill and Malamud 2014; Gallina et al. 2016)
<b>Risk</b>	The potential consequences of a hazard, which can be reported in probabilistic or semi-quantitative terms.	(Alcántara-Ayala and Goudie 2010; Kappes et al. 2012ab; Gallina et al. 2016)
<b>Multi-hazard risk</b>	The total risk from multiple hazards.	(Kappes et al. 2012ab; Gallina et al. 2016; Liu et al. 2016)
<b>Exposure</b>	Refers to all the elements at risk including environmental, economic and cultural assets.	(Kappes et al. 2012ab; Gallina et al. 2016; Liu, Siu et al. 2016)

The first two challenges are related to multi-hazard analysis while the last two items refer to multi-hazard risk assessment. There are two approaches to overcome the problems related to different units and characteristics of hazards: 1) the qualitative approach, which classifies hazards through ranking scores, and 2) quantitative and semi-quantitative approaches that compare indices. Regardless of these approaches, to date, only single hazard values are accumulated for multi-hazard assessment (Kappes et al. 2010; Kappes et al. 2012b). However, most hazards interact nonlinearly and trigger the second hazard or increase/decrease the probability of other events by changing the system state. Ignoring these relationships may lead to the misevaluation of arising risk level; therefore, the interactions need to be addressed in multi-hazard studies.

Despite concentrated efforts to mitigate risks in mountain areas, hazards are still serious threats to communities, as considerable losses are related to climate change, land-

use change, and increasing population density. Notwithstanding the ample research on mountain hazards, there is still a gap in knowledge related to spatiotemporal dynamics of the high-mountain systems as the inherent characteristics of geosystems.

### **1.3 Relevant theoretical basis**

The study of natural hazards has a long history in geography research because they are the result of conflicts between natural processes and human systems (Montz and Tobin 2011). Since one of the aspects of these processes involves landform development that can result in catastrophic events on human systems, different concepts have been developed in Geography to address the complex interactions of them with physical systems. Geomorphologists explain landscape evolution and geomorphic hazards by endogenic-exogenic forces, destructive and constructive processes, erosional and depositional forms, stress-strength relationships, and polygenesis and inheritance concepts (Alcántara-Ayala and Goudie 2010).

In this fashion, the agents associated with geomorphic hazards can be classified into three main groups including endogenous and exogenous forces, climate, and land-use change. Neotectonics and volcanic processes are considered as endogenous forces, while glacier hazards, floods, snow avalanches, mass movements and coastal hazards are due to exogenous forces, which can then be linked to climate and land-use change (Slaymaker 1996). Processes like mass movements can also be explained by stress-strength relationships, where gravity reduces the strength and changes hillslope systems. By constructive and destructive concepts, hazards and processes like flooding, weathering, and debris flows, can be defined in terms of erosion and deposition forms.

Most geographers accredit Barrows' student, Gilbert White, with inaugurating the research directions and foundational approaches that remain as the contemporary orientation of hazard subject (Kirby 1990; Cutter 2001). White's research (1973) can be summarized as the perception of floodplain occupants to the risks of living there and the spatiotemporal adjustments ranging from the cause modification to loss modification and distribution (Chorley 1973). His research aimed at two basic objectives, one was oriented towards the policy development and the other was about the conception of "hazard" from a human perspective in terms of hazard creation and mitigation. White concluded that flooding losses had increased between 1942 and 1956 although the investments on flood control plans like dams and levees and channel infrastructures have increased over US\$ 5 billion (White 1974; Rosenfeld 1994). Therefore, the research findings indicated that growing population in hazards-prone areas would result in increased damage as a result of hazard events despite significant investment in hazard prevention. These discoveries led to the development of a framework consisting of five major components, which classifies hazards, people affected by those hazards, and the range of responses (adjustments) to the hazards. Hewitt (1983) asserted that White's framework focusing on extreme events and physical phenomenon would result in misunderstanding and underestimation of the elements that influence the hazard response. In fact, Hewitt emphasized the socio-economic aspect of hazards rather than monitoring and predicting them (Gares et al. 1994). Rosenfeld refers the Hewitt's perspective and progress in human aspects of natural hazards to the Marxist theories. From this perspective, it is economic systems that force people to live in hazardous areas.

In physical geography, the system approach became one of the most popular theories in the 1960s, through which geomorphologists attempted to explain landscape evolution, complex system dynamics, and instability principals. With this idea, the elements are mechanical entities (slope angles, aspect, sediments,) which interact in a complex way (Oguchi and Butler 2017). The state of the system was then defined by the attribute-values of all the elements. Following that, the concept of system was defined as (Scheidegger 1992):

1. A set of elements identified with attribute values
2. A set of relationships between these attributes
3. A set of relationship between these elements and the other systems

In this way, a system is a collection of interlinked elements which operate together as an enclosed feature of the environment, while geomorphic systems are open to the other systems that mass and energy cascade through the system and exit to another one. Therefore, it is the best approach to employ for explaining multiple hazards since each element and the corresponding relationship cannot be considered separately, and from these interconnections the accurate combined influences can be calculated.

However, a geomorphic system does not necessarily function as a linear system (Phillips 2003). It operates nonlinearly if the outputs are not in proportion to the inputs throughout the entire system inputs. In the context of earth surface science, nonlinearity has been defined by chaos, fractals, and complex self-organization concepts. These concepts enabled geomorphologists to explain complexity behavior in the system (Malanson et al. 1992). In fact, complexity is a subset of nonlinearity that poses limitations in the path of prediction in geomorphic systems (Phillips 1992). In geomorphology, there

is a perception that this type of complexity established by system equations, models, and controlled experiments have not been widely identified in the real world of geomorphic processes and landforms. In addition, some of these concepts prohibit the ability of predicting and understanding the nature due to the meta-explanation contributions (Phillips 2003; Temme et al. 2015).

Phillips (2003) considers complex nonlinear dynamics not only as an artifact of models but also as observed and documented pieces of evidence in many geomorphic phenomena (Fig 1-1). The sources of nonlinearity in geomorphic systems has been well identified by Phillips in geomorphic processes, controls, and interactions in the form of “thresholds, storage effects, saturation and depletion, self-reinforcing feedback, self-limiting processes, competitive feedbacks, multiple modes of adjustment and self-organization.” Phillips also concludes that both nonlinear dynamics and complexity are not intrinsic to geomorphic systems when dynamical instabilities in the form of short-term perturbations are able to change the phase of system. For example, Knox and Kundzewicz (1997) used paleoflood indicators and found that even moderate climate changes can result in extreme responses and that changes in the magnitude and frequency of extreme floods is an indication of nonlinear dynamical instability in the system due to climate change. Moreover, there is no one-to-one equilibrium between the phase of the system and the environmental controls; multiple equilibria may occur.

Therefore, geomorphic response can change from linear or nonlinear according to the intrinsic structure and evolution history. Based on this view, Pöpl (2010) identified the complex nonlinearity in fluvial systems under the influence of dams to reconstruct geomorphic system behavior.

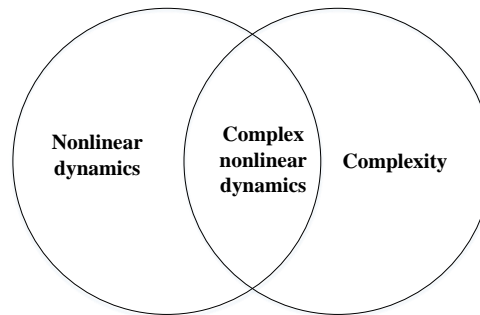


**Figure 1-1** The complex nonlinear dynamics vs. complexity and nonlinear dynamics (Phillips, 2003).

Fuchs (2017) addressed the significant drivers of natural hazards risk in high mountain regions under the impact of climate dynamics from a coevolution perspective. This view includes two independent evolving systems in order to analyze and understand the coevolutionary changes in the interaction of systems, where dynamic paths are dependent on each other. Fuchs includes social dynamics and adjustments to environmental change into this approach. In this context, institutions play an essential role in the development of social and economic behaviors, and consequent exposure evolution and decision-making processes in the European Alps (Fuchs et al. 2017). There are two systems that are attempted to be coupled. First, the system that is defined by population behavior and attributes like the increase in the number of single households since 1960. The second system is determined by the changes in natural hazard management strategies. The evolution in these strategies started with the engineering hazards in 1890 to nonstructural policies (e.g., land use planning) in the 1970s. The recent policies are a combination of both strategies, both structural and nonstructural approaches, to manage the hazards. However, they are still influencing the population behavior by motivating people to increase building densities in hazard-prone areas.

Gill and Malamud (2014) defined the interactions between 21 natural hazards and classified them into six groups according to physical occurrence mechanism including

geophysical, hydrological, shallow Earth processes, atmospheric, biophysical and space hazards. Gill et al. (2017) developed a framework to address the role of anthropogenic processes on natural hazards triggers and to integrate these processes into a multi-hazard approach. These interactions can be summarized where anthropogenic processes (i) trigger natural hazards and (ii) activate/impede natural hazard interactions. In fact, the processes can lead to primary hazards which may or may not develop secondary or tertiary hazards into a chain of interactions. For example, disturbing drainage networks by constructing roads may trigger landslides or floods as a result (Gill and Malamud 2017). In addition, the processes can accelerate or decelerate the incidence of hazards and their interactions. Since triggers act in time and space, they can cause reaction before (t1), during (t2) or after the primary hazards (t3).

Herein, we can modify this approach for climate and geomorphic systems to explain the interaction network of hazards in time and space (Fig 1-2). Nevertheless, the hazards and risk evolution cannot be sufficiently explained by existing concepts, especially when the interactions between different systems, landscapes, and humans are unknown. Therefore, the development of the theoretical basis for interaction between landscape processes is essential. In this context, the application of complexity theory is a promising tool for studying these interactions and relationships in the Earth's surface systems under the influence of climate change.

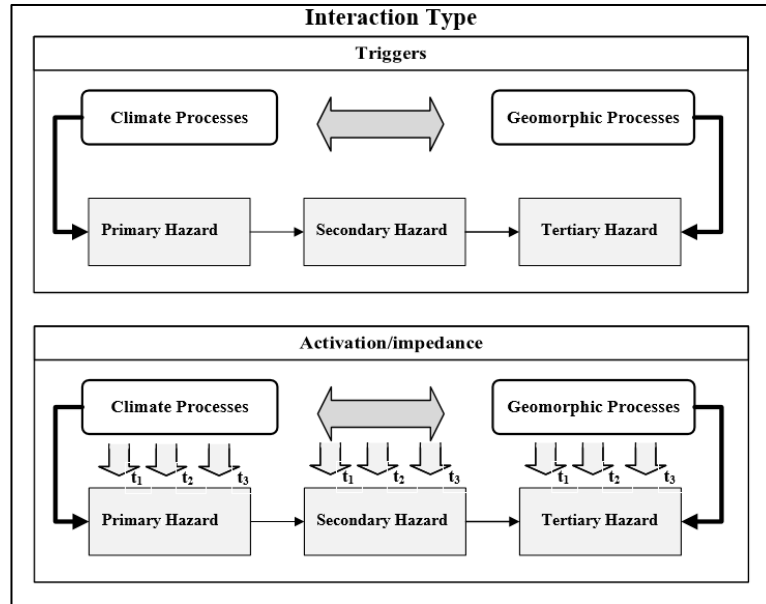


**Figure 1-2** A conceptual model of hazard interactions related to climate and geomorphic processes (modified from Gill, 2017).

#### 1.4 Research study area

Rhone catchment is one of the main case study areas located in the European Alpine areas, in the Canton Valais in Switzerland, hosting a human population of around 300,000 (Fig 1-3). It has an elevation range from about 373 m up to 4631 m above sea-level (a.s.l.) and a mean elevation of about 3,141 m, with a total area of 5,290 km<sup>2</sup>, of which 53.8% is infertile land. Precipitation within the area varies from dry valleys receiving less than 600 mm per year on average to the orographic precipitation in the mountains averaging more than 2500 mm per year (Clarvis et al. 2014; Cantonal Office of Statistics and Equalization 2019). The hydrologic regime of the Rhone catchment is characterized as nivo-glacial, with lower runoff in winter compared to summer (Clarvis et al. 2014; Rahman et al. 2015; Cantonal Office of Statistics and Equalization 2019). Glaciers cover 569 km<sup>2</sup> of the landscape, which is approximately 10% of the area and provide 10% annual runoff of the catchment on average. The area has been affected by anthropogenic infrastructure projects

(e.g., fourteen significant reservoirs and hundreds of substantial river diversions) that change the natural hydrologic regime in the catchment.

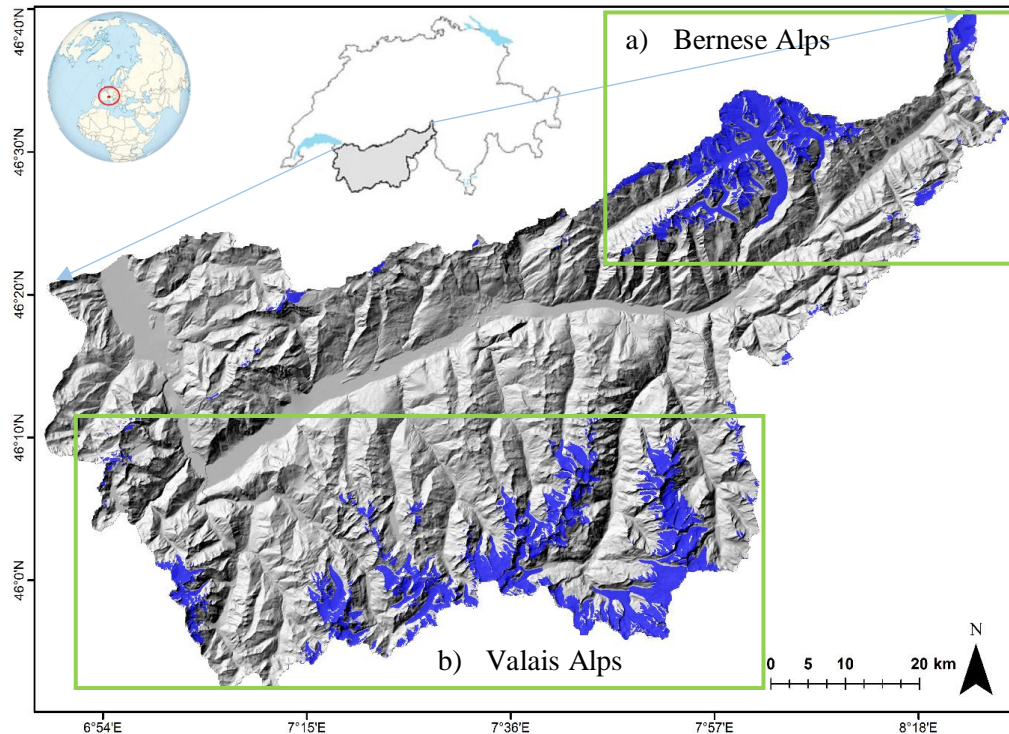


**Figure 1-3** Rhone catchment is located in Valais canton, Switzerland. The investigated glaciers in this catchment are located within the Bernese (Fig 1-3a) and Valais (Fig 1-3b) Alps in the southwestern part of Switzerland (Source: SGI2010 and swissALT<sup>3D</sup>).

In addition, the catchment is prone to different types of natural hazards. It is projected that the maximum hourly and daily discharge will increase. Debris flows are likely to decrease in many sub-basins as a result of a decrease in summer precipitation; however, the magnitude and intensity of events will increase due to increase in heavy precipitation and availability of larger sediment supplies (Stoffel et al. 2014). The period during which debris flows occur is likely to increase as well, so that events will become more frequent from May to late October in the future (Stoffel et al. 2014). Under the control of climate change and permafrost degradation, rockfalls are controlled by permafrost in altitude above

2500 m, and it is expected that they become more dominant in this elevation range (Stoffel and Huggel 2012) leading to increase in risk values for infrastructure and transportation networks at higher elevations. All the described hazards have the potential to convert into multiple hazards in glaciated areas and break the moraine dams in front of glacier lakes. Therefore, monitoring such environments is vital for protecting settlements located downstream.

### **1.5 Overall research objectives and questions**

This study is a contribution to advance lake formation and future hazard and risk assessment associated to lakes under the influence of climate change in high-mountain regions. Therefore, the first objective is to understand the response of the Swiss glaciers to the observed climatic trends.

The main focus of this objective will be to address these primary research questions:

- Have the glaciers been highly sensitive to the fluctuations of air temperature during the ablation season (May-September) and the precipitation during the accumulation season (October-April)?
- Are significant trends in temperature/ablation or precipitation/accumulation observed over the past three decades?

The second objective is to investigate limitations and strengths of Landsat 8 OLI and TIRS data for classification of glacier surfaces in alpine valley glaciers, in order to be used as an input for locating potential future lake formation and associated hazards.

- Which glacier facies can be accurately delineated using the combination of Landsat 8 OLI and TIRS?

The third objective is to expand the knowledge of potential hotspots for future lake formation in the Swiss Alps.

- How the future lakes will be spatially distributed within the glaciers of the Rhone catchment?

## **2 ANALYSIS OF SWISS GLACIER MASS BALANCE AND RESPONSE TO RECENT CLIMATE CHANGE AND REGIONAL ATMOSPHERIC CIRCULATION**

### **2.1 Introduction**

Glacier mass balance, the difference between accumulation and ablation, is an important prerequisite for monitoring direct and immediate impact of climate forcing on the cryosphere (Fischer et al., 2015). Glaciers react to climatic conditions by losing or gaining mass (Zemp et al. 2015; Carturan et al. 2016; Medwedeff and Roe 2017). This reaction is mainly controlled by two processes: snowfall precipitation within the accumulation zone in winter and snow-ice melt, runoff, and sublimation during the summer. In connection with ongoing global atmospheric warming and rising air temperatures, the ablation season has prolonged, resulting in acceleration of glacier volume loss (Zemp et al. 2015; Naegeli and Huss 2017). Therefore, changes in seasonal mass balance can be considered a clear indicator of climatic variations in high-mountain regions (Huss and Bauder 2009). As glacier mass balance is linked directly to local meteorological conditions, large-scale atmospheric circulation, as well as glacier dynamics and hydrology, a thorough understanding of glacier mass balance and the interactions with climatic variables is critical to local communities and regions because of hydropower supply (Miller et al. 2012; Schleiss and Oberrauch 2014; Rahman et al. 2015; Milner et al. 2017; Piot 2017; Rasul and Molden 2019), irrigation systems (Immerzeel et al. 2010; Chevallier et al. 2011), hazard monitoring (Huggel et al. 2004; Haeberli et al. 2016; Klimeš et al. 2016; Harrison et al. 2018), and opportunities like geotourism (Koenig and Abegg 1997; Demiroglu et al. 2018; Spandre et al. 2018, 2019).

The first mass balance study involved a series of measurements on Nordic glaciers

in the 1920s and 1930s by the Swedish glaciologist H.W. Ahlmann (Braithwaite 2002). However, glacier monitoring started in 1894 with a more simplified focus on glacier length changes (Hall 1895). After the late 1940s, interests were shifted to collecting data on glacier-wide mass balance (Haeberli et al. 1998). The first standardized data publication on change in glacier length, area, volume, and mass started with the ‘Fluctuations of Glaciers’ series in the late 1960s (Zemp et al. 2015; World Glacier Monitoring Service (WGMS) 2017). Since the 1980s, data on glacial change has been documented in a relational database, Worldwide Glacier Monitoring, for access by scientists, policy makers, and the public (Hoelzle and Trindler, 1998; Zemp et al. 2015). The World Glacier Monitoring Service (WGMS) plays a critical role by compiling available data through a scientific and international network based on contributions from thousands of observers from all over the world. These archives are based on common measurement protocols and are currently available through the WGMS and Global Terrestrial Network for Glaciers (GTNG) as part of the Global Climate Observing System. Mass balance data are obtained either from direct glaciological methods (field measurements) or from satellite/aerial monitoring change on glacier surface topography which converts the volume to mass change using a density assumption (e.g. Abermann et al. 2009; Carturan et al. 2013).

Compared to other mountain ranges around the world, the European Alps have the longest record of mass balance data. According to available reports and previous studies, these glaciers have demonstrated great mass loss since the Little Ice Age. Zemp et al. (2008) modeled glacier mass balance fluctuations for the European Alps dating back to 1850 using the inventory from the WGMS and the Swiss Glacier Inventory of 2000. They reported an overall estimated loss of 35% in glaciated areas from 1850 to the 1970s,

followed by a 50% acceleration in mass loss from 1970s to 2000 mainly due to terminus retreat. It has been suggested that such fluctuations in glaciers are the indirect, and lagged response to past climatic conditions (Huss et al. 2010a; Huss et al. 2010b; Zemp et al. 2015). Huss et al. et al. (2010b) re-analyzed seasonal glacier-wide mass balance in the south-eastern Swiss Alps from 1900 to 2008 based on field measurements. Using a distributed accumulation and temperature-index model, the authors concluded that the rate of mass loss in this time frame varied significantly between adjacent glaciers because of the dynamic adjustment to the post-Little Ice Age climate change, namely warm air temperatures. Their study also projected a 63% decrease in glacier extent through 2050 and increased annual runoff over the next three decades for the deglaciated catchments. Fischer et al. (2015) extended a re-evaluated inventory of geodetic mass balance, surface elevation change, and volume change for the entire glaciers in the Swiss Alps from 1980 to 2010. The estimated average mass balance was  $-0.62 \pm 0.07$  m w.e.  $\text{yr}^{-1}$ , with an overall volume loss of  $-22.51 \pm 1.76$  km<sup>3</sup>. The findings of this research also revealed the mass change for glaciers in Valais Alps (Rhône) to be less ( $-0.59$  m w.e.  $\text{yr}^{-1}$ ), and the southern glaciers (e.g. Maggia, Ticino, Maira, Poschiavino) to be greater, than the entire Swiss Alps. Following that study, Huss et al. (2015) re-evaluated 19 series of glacier-wide seasonal mass balance for the Swiss Alps based on point observations to establish a homogenous mass balance series. This dataset, which includes winter (1 October–30 April) and summer (1 May–30 September) observations back to the 1980s, offers a strong basis for analyzing the response of glacier mass balance components to climate variability and change.

Previously, numerous studies have addressed the sensitivity of mass balance to various climatic factors including changes in surface air temperature and precipitation

(Oerlemans et al. 1998; Braithwaite and Zhang 2000; Oerlemans and Reichert 2000; Klok and Oerlemans 2002; Woul and Hock 2005; Carturan et al. 2016; Zhu et al. 2018). Huss and Fischer (2016) also developed a model, Glacier Evolution Runoff model, to evaluate the response of very small glaciers ( $<0.5 \text{ km}^2$ ) in Switzerland to current and future atmospheric warming. According to their study, Swiss glaciers are projected to disappear in the next 25 years. Glacier mass balance, in general, has also been linked to oceanic and atmospheric variability through various climate indices (e.g. North Atlantic Oscillation (NAO), East Atlantic (EA) pattern, and the Atlantic Multidecadal Oscillation (AMO)) (McCabe et al. 2000; Shahgedanova 2005; Marzeion and Nesje 2012; Thibert et al. 2013; Carturan et al. 2016). The impact of such climate forcings on Swiss glaciers have been addressed in a few studies (Beniston 1997; Huss and Bauder 2009; Huss, Hock, et al. 2010). Huss et al. (2010a) associated North Atlantic climate variability with the 100-year surface mass balance record for thirty Swiss glaciers. The results found the AMO index inversely correlated with glacier mass balance, suggesting that positive AMO values (warm sea surface temperatures) impacted significant mass loss from 1908 to 2008.

Despite these efforts, there is a further need to perform the time series analysis on Swiss glacier mass balance changes and linkage to local and remote climatic conditions, specifically for glaciers whose geodetic measurement are included in newly developed datasets (Huss et al. 2015). It is essential in particular for studying the development and evolution of catchments through ice melt and associated elements such as new lakes, trigger factors (e.g. slope movements) of Glacial Lake Outburst Floods (GLOFs), since they are closely tied to glacier ice loss (Clague et al. 2012). Therefore, monitoring glacier behavior is critical for detecting these types of hazards within catchments. In this study, we

analyze the behaviors of the south-western Swiss glaciers in the context of post-Little Ice Age climate change. We also present a long-term (1970-2017) time series analysis of annual glacier mass balance (1 October–30 September), as well as winter (1 October–30 April) and summer (1 May–30 September) mass balances, derived from glaciological reports (1881–2014) contained in the WGMS (2017). Additionally, we analyze and compare the time series data to identify trends, fluctuations, and similarities in glacier annual and seasonal mass balances. We further provide hypsometric characteristics of these glaciers using swissALTI3D DEM and Advanced Spaceborne Thermal Emission and Reflection Radiometer (ASTER) Global DEM (GDEM) Version 3 (V3) and examine the possible impacts of their geometry on the recorded responses. The proposed study considers Holt’s exponential smoothing to make short-term forecasts of the future annual mass balance values. We further explore impacts of local climatic variations, including the air temperature fluctuations during ablation season (May-September) and precipitation during accumulation season (October-April), and the influence of regional atmosphere-ocean patterns, through the AMO, NAO, EA, Scandinavian pattern (SCA), and Greenland Blocking Index (GBI), on the mass balance characteristics of surveyed Swiss glaciers.

## **2.2 Case study**

This study focuses on seven glaciers (Grosser Aletschgletscher, Allalin, Hohlaub, Schwarzberg, Gries, Gietro, Rhone) of varying size, shape, hypsometry, aspect, and slope, located in Rhone catchment (Fig 2-1). Two additional glaciers located outside of Rhone catchment, with the longest records in the Swiss glacier database since the 1900s (Figure 2-3), are included to understand the regional variations between the glaciers and provide

information on the temporal and spatial patterns of mass-balance fluctuations within the Swiss Alps. These two glaciers, Silvretta and Clariden, are located in Central and Glarus Alps, respectively (see Fig 2-1 & Table 2-1).

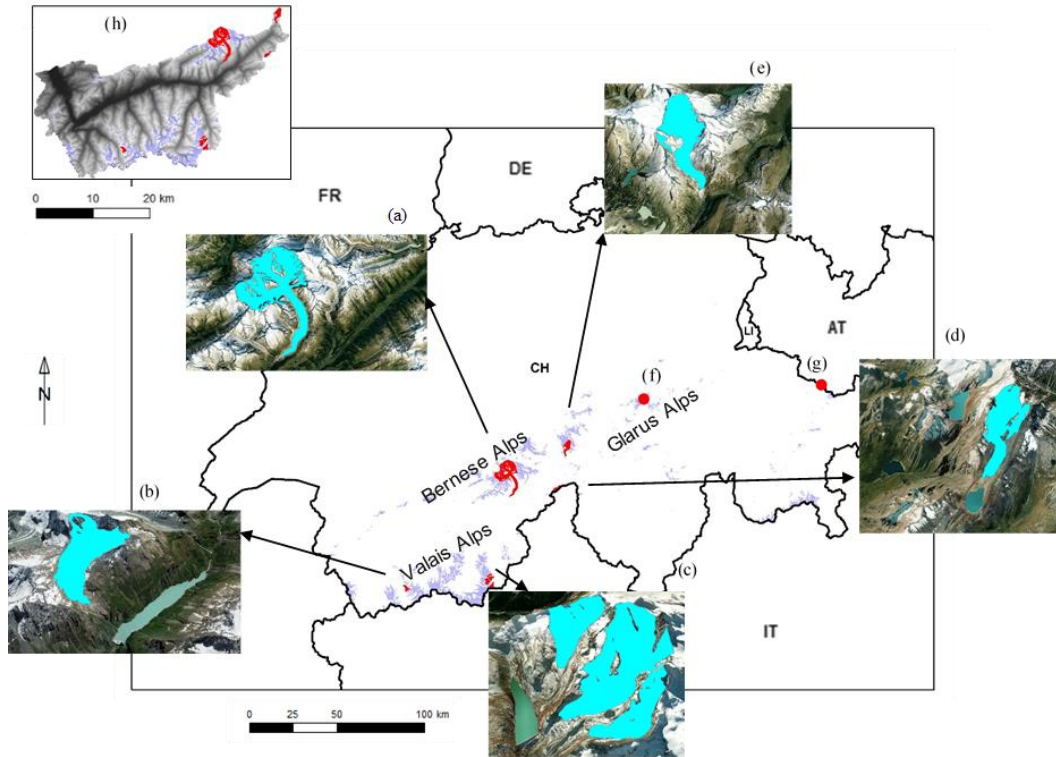


**Figure 2-1** Overview maps of the research study area and the glaciers with mass balance measurements analyzed in this work (Google Earth imagery, DHM25/200) a) Grosser Aletsch b) Gietro c) Hohlaub, Allalin, Schwarzberg (left to right) d) Gries e) Rhone f) Clariden g) Silvretta h) Rhone catchment.

The glaciers vary in size from 2 to 83 km<sup>2</sup> as documented by a geophysical dataset from glaciological reports (1881–2014) by the Laboratory of Hydraulics, Hydrology and Glaciology at ETH Zürich (VAW/ETHZ), which includes stake-derived mass balance measurements as well as geometries, aspects, and local climatic conditions of individual glaciers. Grosser Aletschgletscher, which is located within the Bernese Alps, is the longest (22.6 km) and largest (83.0 km<sup>2</sup>) ice body in the European Alps with an extensive archive

of climate data and glaciological records dating back to 1841 (Holzhauser 2009; Kropáček et al. 2014).

**Table 2-1** Overview of the characteristics of selected glaciers in this study.

Glacier	Location (Alps)	Period	$\Delta t$	Elev.range (m a.s.l.)	ELA (m a.s.l.)	Area (km <sup>2</sup> )	AAR (%)	Prevailing aspect
Allalin	Valais	1956-2018	62	2693-4180	3575	9.64	27	NE
Hohlaub	Valais	1956-2018	62	2843-4030	3365	2.12	30	E
Schwarzberg	Valais	1956-2018	62	2680-3566	3155	5.10	33	NE
Gries	Valais	1962-2018	56	2432-3307	3285	4.34	0	NE
Gietro	Valais	1966-2018	52	2751-3817	3315	5.20	22	NW
Rhone	Bernese	1885-2018	39	1775-3620	3085	15.10	35	S
Aletsch	Bernese	1940-1999	59	1560-4085	3055	83.02	56	SE
Silvretta*	Central	1918-2017	99	2474-3071	2925	2.60	1	W
Clariden*	Glarus	1914-2017	103	2534-3251	2935	4.50	25	NE

(\*two glaciers outside the study area)

The accumulation area of this glacier faces south and contains two summits, Jungfrau and Mönch. The main body is divided by three branches (Grosser Aletschfirn, Jungfrau firn and Ewig Schneefeld) at Konkordiaplatz with reported ice thickness of 890 m on its central point. According to the reports, it has lost significant volume since the Little Ice Age with a fast acceleration since the late 1980s (Fig 2-2) (GLAMOS 2017). The local climate of the glacier front is characterized as dry, whereas a high amount of precipitation has been noted in the accumulation area due to regional advection effects (Schwarb and Schär 2000).

Rhone is a south-facing valley glacier with a climatic condition similar to Aletsch. Gries is different in this regard than the other glaciers as it is placed south of the main Alpine crest at the border of Italy within a small valley exposed a north-eastern direction with relatively high precipitation.



**Figure 2-2** Drastic ablation, reduction in elevation surface and width, that has occurred over the course of the 20th and into the 21st Century; 2009 picture taken by co-author D. Butler.

According to Huss et al. (2009), Gries and Aletsch have lost 39% and 16% of their ice volume in the 20<sup>th</sup> century, respectively. Mass balance monitoring programs were established on Gries in the 1960s with hydropower projects whereas the data collections on Aletsch and Rhone were taken as part of glaciological research projects.

The Mattmark region includes three glaciers (Allalin, Hohlaub, Schwarzberg) with the longest mass balance record dating back to 1955, established during the construction of Mattmark dam in the Saas Valley. VAW/ETHZ has been observing the glaciers in corresponding catchments including Gietro and two other glaciers, Allalin and Schwarzberg in the Mattmark area (Saastal).

Allalin is a large valley glacier flowing in a north-east direction and covers 9.6 km<sup>2</sup> of the Saastal Valley. This glacier has the highest equilibrium line altitude (ELA) of 3575 m a.s.l., owing to the lack of solid precipitation in the valley (WGMS 2017). According to

the Swiss glaciers report in 2014/15, the least amount of mass loss, relative to the inventory, was recorded for this glacier with average thickness changes of approximately -0.6m w.e.

### 2.3 Data

For the Swiss Alps, two direct mass-balance series are available which span five continuous decades (Glaciological reports 1881–2014; Huss et al. 2015; Huss and Fischer 2016; World Glacier Monitoring Service (WGMS) 2017). The mass balance is calculated by glaciological field methods including dense snow probings and pits in April-May that measured the winter snow accumulation, and ablation stake readings in September (Huss and Fischer 2016). The longest mass balance time series (since 1900) for 50 glaciers in the Swiss Alps has been reconstructed by Huss et al. (2015) based on the combination of field measurements and ice volume changes by comparison of digital elevation models (DEMs). There are seven glaciers in the Rhone catchment with a long sequence of mass balance measurements recorded since 1884, and Figure 2-3 shows the length of available time series for each glacier (World Glacier Monitoring Service (WGMS) 2017) (Table 2-1, Fig 2-3). Monthly mean air temperature and precipitation data have been used to determine the relationships between the mass balance components and local climate. Long-term homogenized series of average daily air temperatures (two meters above surface) and total precipitation from the Swiss National Basic Climatological Network (NBCN) stations considering the underlying topography, which cover over 1961 to present throughout the entire Swiss Alps, was provided by MeteoSwiss in a  $2 \times 2$ km grid structure (MeteoSwiss 2019). The daily mean meteorological time series for individual glacier was extracted for the gridded area covering the glacier.

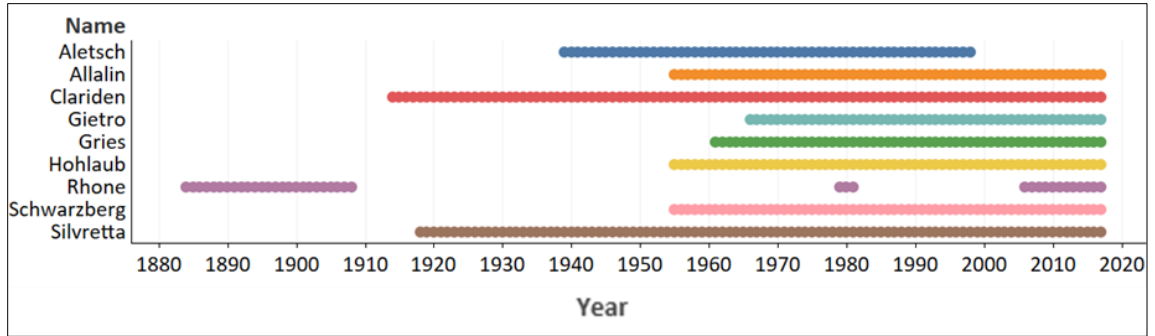


**Figure 2-3** Data coverage of annual mass balances ( $B_a$ ) for the selected glaciers from 1884 to 2017.

In order to assess the relationship between the components of mass balance and the larger-scale atmosphere and oceanic conditions, seasonal (Oct-April and May-September) and annual times series of the NAO, SCA, EA are obtained from the Climatic Prediction Center (CPC), and GBI (Hanna et al. 2014) and AMO are downloaded from the National Oceanic and Atmospheric Administration. The GBI represents the normalized 500 hPa mean GPH anomalies across Greenland, 60–80° N, 20–80° W (Fang 2004; Hanna et al. 2014, 2016, 2018). The NAO can be defined in several ways, and we use two versions here. The Hurrell NAO is based on an empirical orthogonal function (EOF) analysis of North Atlantic sea-level pressure (SLP) with the two action centers over Iceland and the Azores (Hurrell 1995). To evaluate the upper-air circulation features over a similar geographic area, the CPC NAO index is used supplementally and is based on the rotated EOF of North Atlantic 500 hPa anomalies. The second and third EOFs of the CPC analysis, the EA and SCA, are also analyzed to understand a broader array of North Atlantic synoptic settings potentially linked to Swiss glaciers variability and changes. The EA pattern tends to have action centers near 80°N and 20–35°W, while the SCA coincides with high pressure centers over Scandinavian countries during its positive phase (Wallace and Gutzler 1981; Barnston and Livezey 1987). The AMO index used here refers to detrended anomalies of

the sea surface temperature in the North Atlantic Ocean calculated from the Kaplan SST dataset (Kaplan et al. 1998; Enfield et al. 2001). Positive AMO values are associated with warm near-surface air temperature anomalies in Europe, and prevailing low-pressure anomalies over the Atlantic and Europe during the winter (DJF) (Knight et al. 2006). This teleconnection is linked to continental climate variations in both North America and Europe (Enfield et al. 2001).

For generating the hypsometric information and profiles, we used swissALTI<sup>3D</sup> DEM obtained from the Swiss Federal Office of Topography (Swisstopo) for the 7 glaciers in Rhone catchment (swisstopo Online Shop 2019), and the newly released Advanced Spaceborne Thermal Emission and Reflection Radiometer (ASTER) Global DEM (GDEM) Version 3 (V3) data for the 2 additional glaciers located in Central and Glarus Alps. This swissALTI<sup>3D</sup> DEM represents the surface of Switzerland without vegetation and infrastructure at a spatial resolution of 10 m. SwissALTI<sup>3D</sup> has been available since 2013 and is updated in a 6-year cycle based on aerial remote sensing datasets. swissALTI<sup>3D</sup> is derived by stereo correlation of 25 cm resolution of 2008–2011 SWISSIMAGE Level2 aerial orthophotographs for areas above 2000 m a.s.l., with a vertical accuracy of approximately  $\pm 1$  to 3 m at the  $1\sigma$  level. Terrain below 2000 m a.s.l. are generated using airborne laser scanning data with an accuracy of  $\pm 50$ cm at the  $1\sigma$  level (Möri and Wiederkehr 2013). In addition, the model consists of digitized lakes, break lines, and spot heights (i.e., elevations) with an average deviation of 25cm to  $\pm 1$  m. The ASTER GDEM V3 was released recently and displays similar level of accuracy as ASTER GDEM V2 (LP DAAC 2019). However, compared to V2, V3 has lesser void area due to the increase in ASTER stereo image data since the previous release and improved processing (LP DAAC

2019).

## **2.4 Methodology**

### **2.4.1 Exploratory Data Analysis**

Using the WGMS database, time series of annual mass balance ( $B_a$ ), winter mass balance ( $B_w$ ), summer mass balance ( $B_s$ ) and AAR (the ratio of accumulation area at the end of melt season to total glacier area) were calculated and assessed for inhomogeneities (i.e., missing values (Fig 2-3), and any change in unit measurements), testing assumptions to select the analysis strategy (e.g., presence of autocorrelation within the time series), trends and outliers, fluctuations and the general pattern of glacier behaviors (i.e mean and standard deviation of  $B_a$ ,  $B_s$ ,  $B_w$  and AAR of glaciers) within the common period of observation (1970-2017). Exploratory analyses are initially conducted including time series plots, boxplots, autocorrelation functions, correlation matrices and smoothing techniques (i.e., moving averages). To identify similarities between glaciers and address the seasonal aspect of mass balance, the  $B_a$  series of all the glaciers were intercompared and linked with  $B_w$  and  $B_s$  characteristics using Spearman correlation analysis. Prior to conducting correlation analyses, data series are detrended using a triangular moving average approach to detect and highlight intradecadal changes (Beniston 2005; Scherrer and Appenzeller 2006; Thibert et al. 2013). A 7-yr level of triangular average is applied as it yields optimal correlations between the annual and seasonal mass balance of all glaciers versus seasonal and annual climate indices.

### **2.4.2 Structural change model**

Various approaches have been developed in the literature for testing structural

changes and identifying breakpoints in time series. Most tests examine coefficient changes of a linear regression model where the assumption is a single change in time and the type of change are known (Zeileis et al. 2003). Another method referred to as multiple structural changes has been widely used (Bai 1997; Hawkins 2001; Sullivan 2002; Bai and Perron 2003; Zeileis et al. 2003), and tested the potential for multiple shifts in a data series.

If we consider a linear regression model as:

$$y_i = x_i^T \beta_i + \mu_i \quad (i = 1, \dots, n) \quad (1)$$

where at time  $i$ ,  $y_i$  is the observation of the dependent variable,  $x_i$  is a  $k \times 1$  vector of regressors, and  $\beta_i$  is the  $k \times 1$  vector of regression coefficients (Zeileis 2004). Here, the null hypothesis is that the regression coefficients are consistent, while the alternative hypothesis is that at least one coefficient changes over time.

$$H_0 : \beta_i = \beta_0 \quad (i = 1, \dots, n) \quad (2)$$

This assumes that there are  $m$  breakpoints, where the coefficients deviate from one stable regression relationship to a different one (Zeileis et al. 2003). Thus, there are  $m+1$  segment in which the regression coefficients are constant, and model (1) can be rewritten as:

$$y_i = x_i^T \beta_i + \mu_i \quad (i = i_{j-1} + 1, \dots, i_j, j = 1, \dots, m + 1) \quad (3)$$

where  $j$  is the segment index  $I_{m,n} = \{i_1, \dots, i\}$  refers to the set of breakpoints or the number of  $m$  partitions (Zeileis et al., 2003).

Two approaches for testing of structural change are used: (i)  $F$  statistics (Andrews and Ploberger 1994), and (ii) generalized fluctuation tests (Kuan and Hornik 1995); the former approach tests against a single-shift alternative of unknown timing, whereas the latter technique, also known as empirical fluctuation process (efp), is concerned with

constancy in a graphic method reflecting the fluctuations in residuals and coefficient estimates (Brown et al. 1975). The null hypothesis of the generalized fluctuation test is based on the central limit theorem and if the efp boundaries are crossed by fixed probability  $\alpha$ , the fluctuation is large and null hypothesis of no structural break is rejected. The efp function from the fluctuation test framework was employed in R and Cumulated Sum of Standard OLS residuals (CUSUM) was specified as the type of fluctuation process to be fitted in argument. Cumulated Sum of Standard OLS residuals (CUSUM) detects change points in time series that often result from structural changes based on the limiting process of standard Brownian motion (Ploberger and Krämer 1992). Since the number of breakpoints  $m$  is not known in advance, it is necessary to compute the optimal breakpoints for  $m = 0, 1, \dots$  breaks and choose the model that minimizes some information criterion such as Bayesian Information Criterion (Kleiber and Zeileis 2008). Following this exercise, a Chow test (Chow 1960) was also performed to confirm the statistical significance of resulting change points at the 95% confidence level when  $p \leq 0.05$ .

### **2.4.3 Trend analysis**

#### **2.4.3.1 Mann-Kendall and Sen's Slope estimators**

To evaluate whether mass balance values increase or decrease over time, the Mann-Kendall test was applied. This test, which is a nonparametric form of monotonic trend regression analysis, is robust to missing values and outliers in time series. The test assumes that the data are independent, and the distribution of data remains consistent (Helsel and Hirsch 1988). Therefore, autocorrelation (ACF) and partial autocorrelation (PACF) tests were conducted and serial correlation was not found in the series which further motivated application of the Mann-Kendall trend analysis.

The Mann-Kendall test calculates the difference between the later value and all previous values,  $(x_j - x_i)$ , where  $j > i$ , and assigns the value of 1, 0, or  $-1$  to positive, no differences, and negative differences, respectively (Mann, 1945; Kendall, 1975). The test statistic,  $S$ , is then calculated as:

$$S = \sum_{i=1}^{n-1} \sum_{j=i+1}^n \text{sgn}(x_j - x_i) \quad (4)$$

where  $\text{sgn}(x_j - x_i)$ , is equal to  $+1$ ,  $0$ , or  $-1$ . When  $S$  is greater than  $0$ ,  $x_j > x_i$ , an upward trend is indicated, while negative  $S$  values,  $x_j < x_i$ , indicates a downward trend. If  $x_j - x_i$  is  $0$  or very small, the trend is not present within the time series. The test statistic  $\tau$  can be computed as:

$$\tau = \frac{S}{n(n-1)/2} \quad (5)$$

which has a range of  $-1$  to  $+1$  and is analogous to the correlation coefficients in regression analysis.  $S$  and  $\tau$  values that are significantly different from zero indicates the presence of trend and rejects the null hypothesis of no trend. Following that, the rate of change or the power of trend can be obtained using the Sen's slope estimator (Helsel and Hirsch 1988):

$$\beta_1 = \text{median} \left( \frac{x_j - x_i}{y_j - y_i} \right) \quad (6)$$

in which the slope of all the pairs are computed and the median of these slopes is denoted.

#### 2.4.3.2 Multiple linear regression

We used multiple linear regression to account for the association of relevant variables including mean temperature (May-Sep) and precipitation (Oct-April), with the annual mass

balance response variable. The regression model that was estimated specified annual mass balance ( $B_a$ ) as a function of time ( $t$ ), (May-Sep) temperature ( $T_s$ ), and Oct-April precipitation ( $P_w$ ) is as follows:

$$B_a = \beta_0 + \beta_1 t + \beta_2 T_s + \beta_3 P_w + \varepsilon \quad (7)$$

where  $\beta_0$  is the intercept,  $\varepsilon$  is the remaining unexplained error in data, and  $\beta_1..3$  refers to the slope coefficients of time, summer temperature and winter precipitation, respectively. The null hypothesis related to time is that the parameter  $\beta_1 = 0$ . Rejecting this null hypothesis in favor of a nonzero  $\beta_1$  would indicate a trend. Similarly, the null hypotheses related to parameter  $\beta_2$  and  $\beta_3$  are that both equal zero. Evidence against these hypotheses (e.g.  $\beta_1 > 0$ ) suggests that they clarify temporal variation in annual mass balance. If the null hypotheses are not rejected, however, a simple regression model should be applied. The key assumptions in this model, include normal distribution of residuals, independent variables, and homoscedasticity (constant variance of residuals), which were tested and satisfied justifying use of this technique.

#### **2.4.4 Holt's exponential smoothing forecast modelling**

The exponential smoothing method has been widely used in environmental applications (e.g., climate forecasting) as it requires no assumption except for a detrended time series (Maia and de Carvalho 2011). Such methods are called self-explanatory since no other covariates are included and only structural changes in training data are considered. Holt's method (2004) has two components which must be updated each period—the level and the trend, which can be formulated as:

$$L_t = \alpha y_t + (1 - \alpha) (L_{t-1} + T_{t-1}), \quad (8)$$

$$T_t = \beta (L_t - L_{t-1}) + (1 - \beta) T_{t-1},$$

where  $0 < \alpha, \beta < 1$  are the smoothing parameters and  $\alpha$  controls the length of the average for the level estimation and  $\beta$  controls the trend smoothing (Holt 2004). The level component is a smoothed estimate of the value of the data at the end of each period, and trend is a smoothed estimate of the mean growth at the end of each period (Maia and de Carvalho 2011).

#### 2.4.5 Hypsometric Index (HI)

We used equation 9 as suggested by (Jiskoot et al. 2009) to perform the HI calculations.

$$HI = (H_{\max} - H_{\text{med}}) / (H_{\text{med}} - H_{\min}), \text{ If } 0 < HI \text{ then } HI = -1/HI \quad (9)$$

Here,  $H_{\max}$  and  $H_{\min}$  are the maximum and minimum elevations, respectively and  $H_{\text{med}}$  is the median elevation. Based on the thresholds suggested by Jiskoot et al. (2009) glaciers can be divided into five categories: (1) very top-heavy ( $HI < -1.5$ ), (2) top-heavy ( $-1.5 < HI < -1.2$ ), (3) equidimensional ( $-1.2 < HI < 1.2$ ), (4) bottom-heavy ( $1.2 < HI < 1.5$ ), and (5) very bottom-heavy ( $HI > 1.5$ ) (Jiskoot et al. 2009).

## 2.5 Results and discussion

### 2.5.1 Analysis of annual mass balance

The employed annual mass balance dataset for the selected glaciers in the Swiss Alps, from the early 1900s to 2017, reveals a negative downward trend and two significant breaks

in the 1980s and 2000s (Fig 2-4). However, the  $B_a$  of Gries and Schwarzberg glaciers show three break points. Accordingly, the series of Schwarzberg includes three phases : i) the years from 1956 to 1970 with a near-equilibrium condition ( $\mu_{Ba} = -69$  mm w.e.,  $\sigma = 344$  mm w.e., rate of change =  $-80$  mm w.e.), ii) the period 1971 to 1980 of mass gain ( $\mu_{Ba} = 621$  mm w.e.,  $\sigma = 933$  mm w.e., rate of change =  $686$  mm w.e.), and iii) after the 1980s with a strong imbalance ( $\mu_{Ba} = -640$  mm w.e.,  $\sigma = 650$  mm w.e., rate of change =  $-641$  mm w.e.). Similarly, Gries shows breaks in: i) the period from 1962 to 1980 with a nearly balanced condition ( $\mu_{Ba} = -91$  mm w.e.,  $\sigma = 704$  mm w.e., rate of change =  $-91$  mm w.e.), ii) from 1981 to 2000 ( $\mu_{Ba} = -885$  mm w.e. ,  $\sigma = 541$  mm w.e., rate of change =  $890$  mm w.e.), and iii) a rapid mass loss period from 2001 to 2017 ( $\mu_{Ba} = -1527$  mm w.e.,  $\sigma = 590$  mm w.e., rate of change =  $-1561$  mm w.e.). Among the other glaciers, the rates of change after break years (1980s) become negative for Allalin and Hohlaub. In Gietro and Silvretta, the rates have changed from  $-200$  to  $-1000$  mm w.e., indicating a trajectory toward disappearance of these glaciers in near future. Based on these results, we can conclude that the 1980s was a decade of mass gain and the 2000s were a decade of rapid mass loss for many of the glaciers in the Swiss Alps. According to Thibert (2018), the melt extremes of 2000s occurred under high shortwave irradiance and large downward latent, and sensible heat fluxes in association with increased atmospheric moisture content. In contrast, melt events at the end of 1980s were associated with lower downward turbulent heat fluxes explained by the high downwelling shortwave radiation under relatively dry and clear sky conditions.

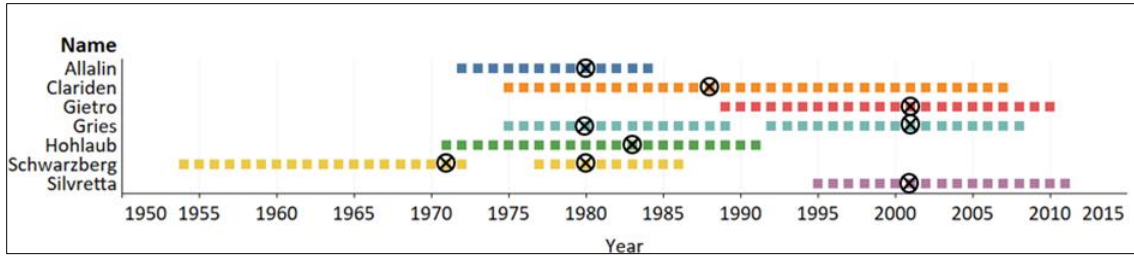


**Figure 2-4** Estimates of the significant break dates (shown in crossed circles) for annual mass balance Swiss glaciers since starting date (see Fig 2-3). Each dashed line represents the time period of 95% confidence interval (Gries and Schwarzberg have experienced two structural changes).

The forecasted annual mass balance of glaciers using Holt’s exponential smoothing up to the year 2030 distinguishes Gries from the other glaciers. The results indicate that Gries is in imminent threat of disappearance between the years of 2018 and 2030, which is also confirmed by strong negative trends since 1970 ( $B_a = -35.7$  and  $B_s = -40.4$ ) (Table 2-2). The glaciers of Gietro, Clariden and Silvretta will closely follow each other in the future with a negative downward trend, whereas Schwarzberg’s mass balance loss will slow down compared to Hohlaub and Allalin (Fig 2-4).

**Table 2-2** The magnitude of trends associated with the seasonal and annual glacier mass-balance trends in time series for common period 1970-2017. All values are significant at the 0.05 level.

Glaciers	$B_a$	$B_s$	$B_w$
Allalin	-18.90	-13.50	-5.45
Hohlaub	-26.50	-17.00	-6.90
Schwarzberg	-26.35	-27.20	-2.00
Gries	-35.74	-40.40	4.65
Gietro	-14.8	-17.40	0.69
Silvretta	-28.04	-38.30	7.17
Clariden	-26.17	-23.30	-0.93

The correlation analysis of glaciers reveals significant correlations between the  $B_a$  of

the glaciers (Table 2-3 & Fig 2-5). Accordingly, Silvretta, Clariden, Gries and Gietro can be categorized into one group, and Allalian, Schwarzberg and Hohlaub in another group.

**Table 2-3** Correlation matrix of  $B_a$  for selected glaciers, values in bold are significant at the 0.01 level (for consistency I would put  $p < 0.01$  instead of the 0.01 level).

<b>Variables</b>	<b>Gietro</b>	<b>Gries</b>	<b>Hohlaub</b>	<b>Schwarzberg</b>	<b>Silvretta</b>	<b>Allalin</b>	<b>Clariden</b>
Gietro	<b>1</b>						
Gries	<b>0.706</b>	<b>1</b>					
Hohlaub	0.461	<b>0.538</b>	<b>1</b>				
Schwarzberg	<b>0.561</b>	<b>0.748</b>	<b>0.797</b>	<b>1</b>			
Silvretta	<b>0.735</b>	<b>0.789</b>	<b>0.551</b>	<b>0.653</b>	<b>1</b>		
Allalin	<b>0.661</b>	<b>0.714</b>	<b>0.789</b>	<b>0.771</b>	<b>0.684</b>	<b>1</b>	
Clariden	<b>0.717</b>	<b>0.782</b>	<b>0.491</b>	<b>0.589</b>	<b>0.820</b>	<b>0.674</b>	<b>1</b>

The similarity of Allalian, Schwarzberg and Hohlaub can be attributed to the proximity of these glaciers and corresponding geomorphic (including elevation range, degree of debris- coverage, surface slope and surface facing) and local climatic (e.g. precipitation and temperature) factors. Although the first group of glaciers are located apart from each other, they have exhibited similar rapid rates of change in mass balance within the available series. In this group, the size of these glaciers, except Gietro, is less than 5 km<sup>2</sup> (Table 2-1), which makes them more sensitive to warming air temperatures.

### 2.5.2 Analysis of seasonal mass balance and accumulation Area

The analysis of  $B_s$  and  $B_w$  suggests that the changes in mass balance are primarily influenced by increases in ablation rates during summer (Table 2-4), which agrees with previous studies (Huss et al. 2015; Carturan et al. 2016). The comparison of summer mass balance and AAR series indicates that the glaciers' accumulation area has decreased at the expense of increased ablation rates and areas. Among the glaciers, the accumulation area of Gries approached zero from 2000 to 2007 and from 2014 to present. Gries is a medium-

sized steep glacier which is faced to the northeast.

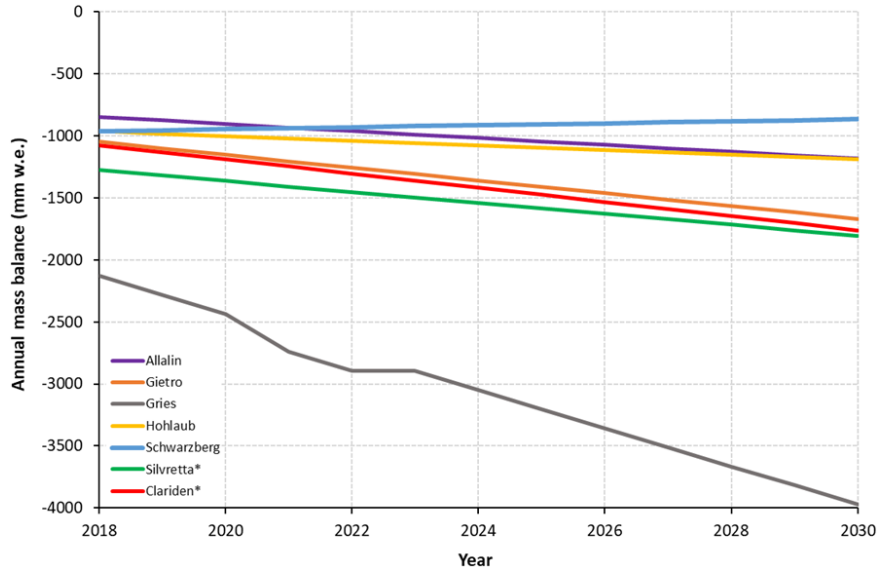


**Figure 2-5** Annual mass balance of glaciers forecasted by Holt’s exponential smoothing up to the year 2030. (\*two glaciers outside the study area).

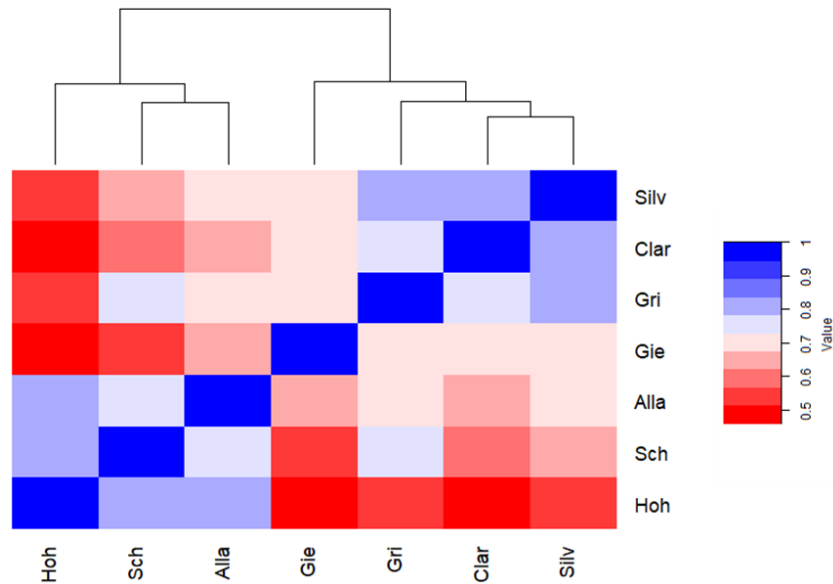


**Figure 2-6** A heatmap representation of the Spearman correlation matrix of  $B_a$  and dendrogram of similar groups of glaciers associated to the Table 2-3 (group 1: Silvretta, Clariden, Gries and Gietro; group 2: Allalian, Schwarzberg and Hohlaub). The right bar shows the color code of coefficients corresponding to Spearman correlations.

**Table 2-4** Correlation coefficients of  $B_a$  versus  $B_w$  and  $B_s$ , and values in bold are significant at the 0.01 level.

Glacier	$\Delta t$	$B_w$	$B_s$
Allalin	62	<b>0.42</b>	<b>0.90</b>
Hohlaub	62	<b>0.48</b>	<b>0.89</b>
Schwarzberg	62	<b>0.33</b>	<b>0.89</b>
Gries	56	0.12	<b>0.88</b>
Gietro	52	0.15	<b>0.85</b>
Rhone	39	<b>0.44</b>	<b>0.90</b>
Aletsch	59	<b>0.39</b>	<b>0.92</b>
Silvretta	99	<b>0.30</b>	<b>0.87</b>
Clariden	103	<b>0.46</b>	<b>0.88</b>

Unlike Gries, the highest increase in AAR has been observed in Clariden, which is likely related to the greater amount of solid precipitation received during the accumulation months. Overall, the accumulation areas of larger glaciers have been more consistent than smaller glaciers. For example, the Aletsch glacier (the largest of those surveyed) balanced its AAR around 50% through the entire period and has been less sensitive to climate fluctuations. The balanced state of larger glaciers can be explained by their ability to dynamically respond to the climate changes by retreating to higher elevations (Huss et al., 2015). In addition, ablation area reductions lead to glacier surface elevation lowering, which initiates a positive feedback resulting from the mass balance altitudinal gradient and reduction in surface albedo (Thibert et al. 2018). Further, this process increases upward longwave radiation from, and downward shortwave absorption into, the melting, low albedo glacier surface and exposed terrain at the terminus (Huss et al. 2015). The time series of glaciers is continuous within the common period of 1970 to 2017 (Fig 2-3). With the comparison of glaciers in this period, lower  $B_s$  mean and higher  $B_s$  variation are observed for Gries with -2232 mm w.e. and 838 mm w.e., respectively (Table 2-5).

**Table 2-5** Mean and standard deviation of Ba, Bs, Bw and AAR (%) in the common period 1970-2017. The significantly different values in each category are bolded.

Glacier	Mean (Ba)	SD(Ba)	Mean (Bs)	SD (Bs)	Mean (Bw)	SD (Bw)	Mean (AAR)	SD (AAR)
Allalin	-312.5	698.5	-1320.7	559.2	1008.1	345.4	47.2	26.7
Hohlaub	-352.04	<b>923.1</b>	-1530	720	1177.9	417.3	47.7	27.1
Schwarzberg	-367.8	866.2	-1570.3	685.9	1202.4	<b>442.6</b>	44.4	24.6
Gries	<b>-919.2</b>	831.2	<b>-2232.1</b>	<b>838.9</b>	1312.8	388.1	<b>26.3</b>	25.9
Gietro	-468.5	685.3	-1568.6	689.2	1100.1	333.3	43.5	27.7
Silvretta	-509.5	747.6	-1694.2	809	1184.6	351.5	<b>36.3</b>	28.4
Clariden	-311.1	792.3	-1696.5	776.1	<b>1385.4</b>	403.7	<b>56.1</b>	25

During the accumulation season, glaciers received an average of approximately 1000 mm w.e., with the highest value for Clariden (1385 mm w.e.). In the same period, the lowest average annual mass balance of -919 mm w.e. for Gries, and -509 mm w.e. for Silvretta were detected. Similarly, the mean AARs were significantly lower for Gries and Silvretta (26% and 36%) and higher for Clariden (56%). The comparison of seasonal and AAR values indicates that glaciers like Hohlaub, Allalin, Schwarzberg are roughly in equilibrium relative to other glaciers due to higher altitudinal ranges. Switzerland’s air temperatures are highly dependent on elevation; much of the observed warming has been focused at lower elevations due to increased incoming shortwave radiation under more frequent anticyclonic conditions (Rottler et al. 2019).

### 2.5.3 Climatic controls

#### 2.5.3.1 Local meteorological variables

During the period of 1970 to 2017, the air temperature of May to September indicates strong warming trends (Fig 2-8b, d, f and h). The weather station data indicate the highest trends during the summer for glaciers located in southern Rhone including Gietro,

Hohlaub, Allalin, and Schwarzberg ( $0.58^{\circ}\text{C decade}^{-1}$ ) (Fig 2-8b) and the lowest trend for Silvretta ( $0.46^{\circ}\text{C decade}^{-1}$ ) (Fig 2-8f). Similar to the findings from Carturan et al. (2016) for the Italian Alps, three discernible phases can be detected from an 11-year running mean applied to the time series. The first phase starts from 1970 with the mean air temperatures around  $-1^{\circ}\text{C}$ , then after 1985 the temperatures reached  $0^{\circ}\text{C}$  and remained stable until 2000s. Since the 2000s, air temperatures over glaciers have been accelerating beyond  $0^{\circ}\text{C}$  and approached to  $+1^{\circ}\text{C}$  in recent years with the unprecedented peak of roughly  $+3^{\circ}\text{C}$  for all glaciers in 2003. The warming trends during the accumulation season (Oct-April) vary from  $0.32$  to  $0.43^{\circ}\text{C decade}^{-1}$ , with the lowest trend associated with Silvretta and the highest to southern Rhone glaciers. The fluctuations in temperature values over the selected period were different for the glaciers located in southern Rhone during the accumulation season. The corresponding moving averages show a levelling off of the trend above  $0^{\circ}\text{C}$  which lasted up to 1985. Afterwards, a gradual drop continued for five years until it reached from  $0^{\circ}\text{C}$  to  $+1^{\circ}\text{C}$  above average in 1990s. Over the 2010s, the temperature of this group of glaciers oscillated between  $+2^{\circ}\text{C}$  and  $+3^{\circ}\text{C}$  during the winter months. The warmest peak of these glaciers happened in 1989 and 2014 /2015, whereas a dramatic drop (below  $1^{\circ}\text{C}$  for southern glaciers and below  $-1^{\circ}\text{C}$  for other groups) occurred in 2010. Despite the dissimilarity of Silvretta and Clariden (Fig 2-8h) in ablation season, the temperature trends are quite identical during the accumulation season. The overall analysis of days with the maximum temperature  $>0^{\circ}\text{C}$  per year for all selected glaciers indicates that the total number of days has considerably increased from 130 days in 1970 to 175 in 2015 with a change rate of  $8.8$  days  $\text{decade}^{-1}$  (Fig 2-7).

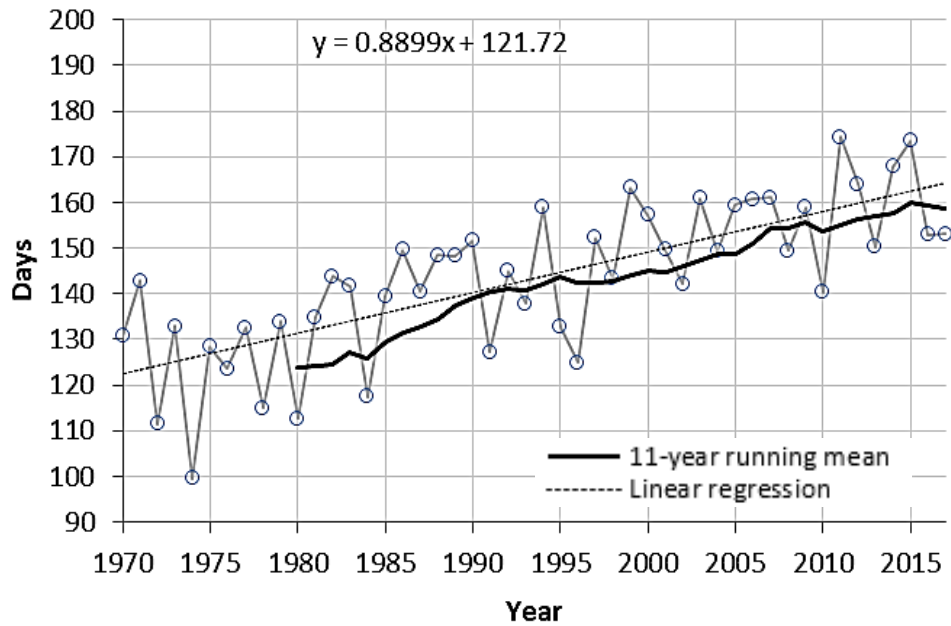


**Figure 2-7** Number of days with the temperature above 0°C over the glaciers per year.

The total precipitation anomalies do not reveal significant trends in accumulation season (Fig 2-9a, c, e and g). The moving averages of precipitation have fluctuated close to the long-term mean. However, for northern Rhone glaciers (Fig 2-9c), and Silvretta (Fig 2-9e) and Clariden glaciers (Fig 2-9g), two phases are apparent. In first phase, periods with above-average precipitation were frequent prior to the second half of the 2000s with the maximum of  $\approx 40\%$  and the minimum of  $\approx -40\%$  in 1985 and 2005, and the maximum of 50% at the beginning of the 1980s. In the second phase, running average precipitation remained steady prior 2010 and then followed by a  $\approx 10\%$  drop below the long-term mean after 2010 and has persisted up to present.

Precipitation during the ablation season showed a slightly different pattern (Fig 2-9b, d, f and h), especially for the glaciers located in the southern Rhone (Fig 2-9b). This group of glaciers has experienced an upward trend over the selected period, including three phases as highlighted by the moving average. The period of the 1970s and the first half of the 1980s with precipitation 10% below the average was followed by a drastic drop to 20%

below average and lasted for 20-25 years. From 2000-2015, only weak fluctuations in precipitation anomalies occurred as values remained around the long-term mean. The variability of precipitation in summer months is considerably higher in the northern Rhone glaciers (Fig 2-9d) compared to Silvretta (Fig 2-9f) and Clariden (Fig 2-9h). Maximum observed summertime precipitation, 50% and 90% above the mean, occurred in 2002 in northern and southern Rhone glaciers, respectively, while minimum precipitation, 40% below mean, is evident among all glaciers in 2003. The investigation of local meteorological time series supports the results in section 2.5.2 that indicated increased ablation duration and the associated feedbacks, surface elevation and albedo reduction, are the main culprits of the annual mass imbalance in the Swiss glaciers.

Reduction in snow/ice-albedo creates a positive feedback mechanism that amplifies snow melt as the temperature increases (Rottler et al. 2019). Exposed dark mountain surfaces absorb the incoming shortwave radiation which in turn results in augments near-surface air temperatures. This finding is supported by the higher significant correlation of  $B_a$  with May-Sep and annual air temperature than the annual and seasonal precipitation during Oct-April (Table 2-6a, b).

In contrast to this overall pattern,  $B_a$  of Clariden and Silvretta shows a higher correlation with May-Sep precipitation and Oct-April air temperature. Correlations may vary between glaciers as orographic precipitation and accumulation in higher elevations may largely differ from one glacier to another glacier. Therefore, the altitude differences between glaciers and the corresponding orographic effect, along with wind drift and avalanches from near slopes, appear responsible for the accumulation differences (Vincent 2002; Thibert et al. 2013).

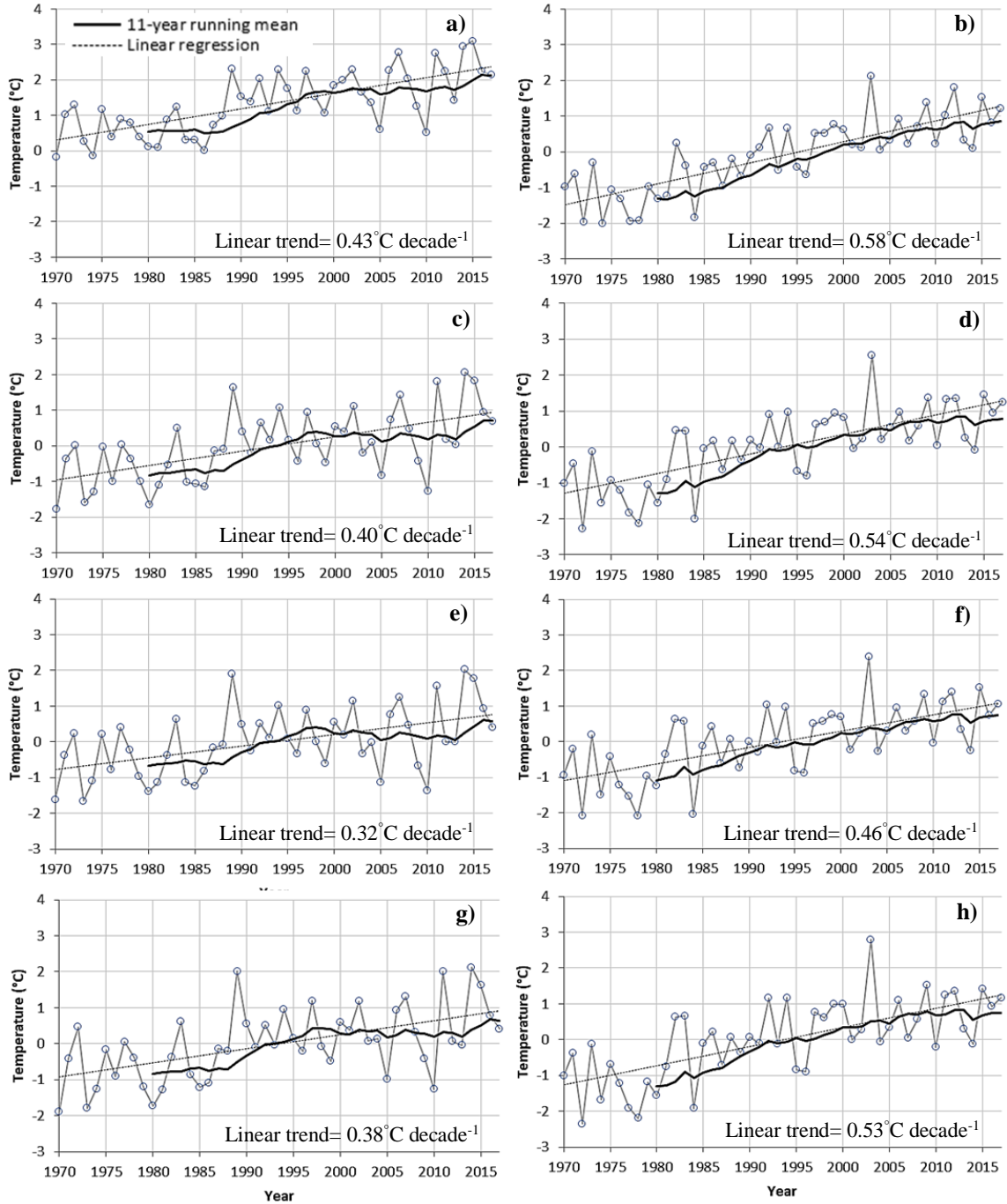


**Figure 2-8** Accumulation season (October- April) air temperature anomalies in a) southern Rhone (including Gietto, Hohlaub, Allalin, and Schwarzberg glaciers), c) northern Rhone (including Grosser Altesch, Gries, and Rhone glaciers), e) Silvretta, g) Clariden. Ablation season (May-Sep) air temperature anomalies in b) southern Rhone (including Gietto, Hohlaub, Allalin, and Schwarzberg glaciers), d) northern Rhone (including Grosser Altesch, Gries, and Rhone glaciers), f) Silvretta, h) Clariden

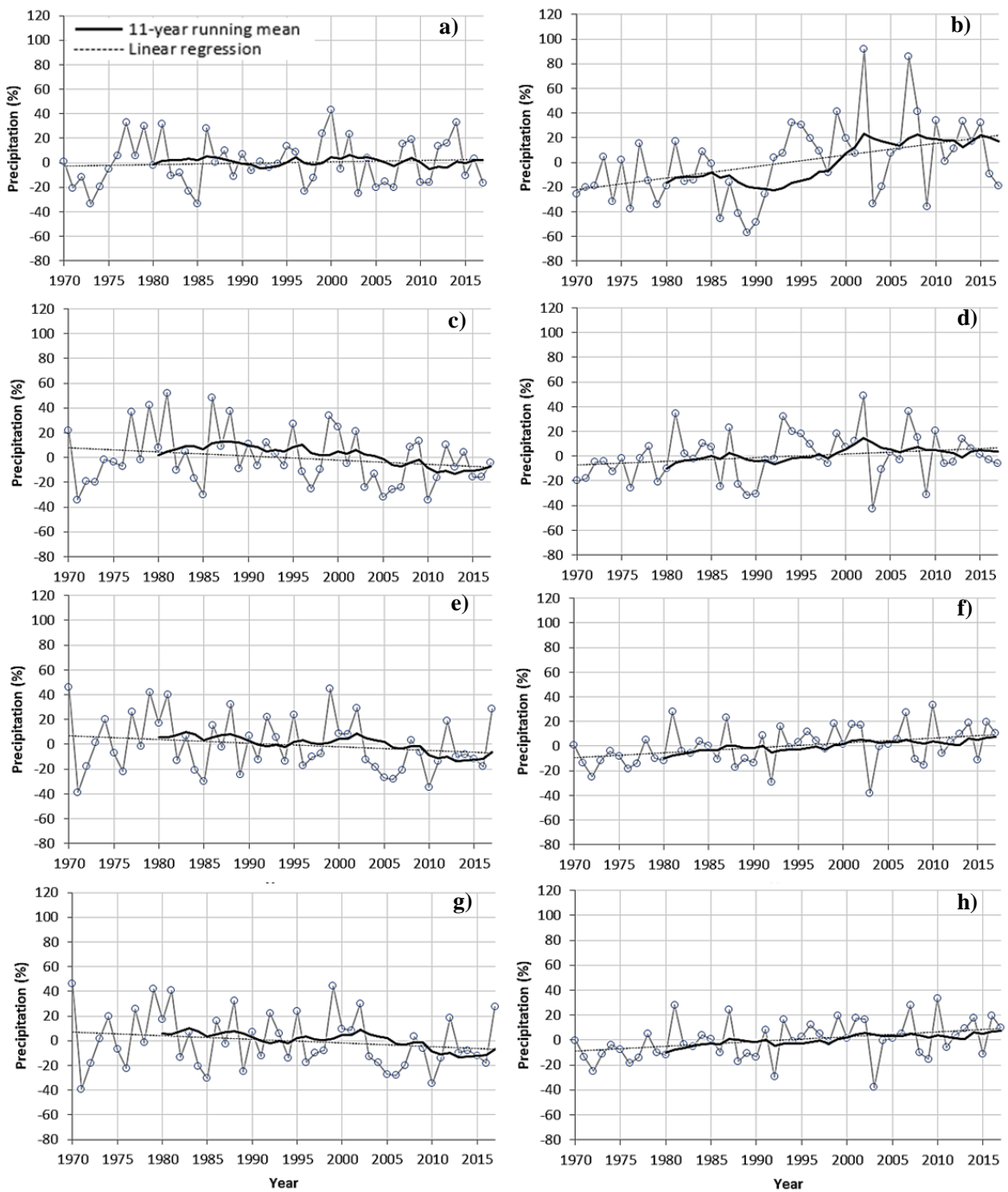


**Figure 2-9** October- April (winter) total precipitation anomalies in **a)** southern Rhone (including Gietro, Hohlaub, Allalin, and Schwarzberg glaciers), **c)** northern Rhone (including Grosser Altesch, Gries, and Rhone glaciers), **e)** Silvretta, **g)** Clariden. May-Sept (summer) total precipitation anomalies in **b)** southern Rhone (including Gietro, Hohlaub, Allalin, and Schwarzberg glaciers), **d)** northern Rhone (including Grosser Altesch, Gries, and Rhone glaciers), **f)** Silvretta, **h)** Clariden.

**Table 2-6** Correlation (a, b) and multiple regression (c) coefficients of Ba versus air temperature and precipitation of summer and winter seasons. a-c indicates significance at the 0.01, 0.05, and 0.10 levels, respectively.

	Allalin	Gietro	Gries	Hohlaub	Schawzberg	Silvretta	Clariden
Oct-April	0.15	0.15	<b>0.28<sup>c</sup></b>	0.05	0.11	0.22	<b>0.27<sup>b</sup></b>
May-Sep	0.01	-0.20	-0.16	-0.07	-0.14	<b>-0.37<sup>b</sup></b>	<b>-0.43<sup>a</sup></b>
Annual	0.16	0.01	0.13	-0.03	-0.01	0.00	0.00
a) Correlation coefficients of precipitation.							
	Allalin	Gietro	Gries	Hohlaub	Schawzberg	Silvretta	Clariden
Oct-April	-0.16	-0.19	<b>-0.43<sup>a</sup></b>	-0.18	<b>-0.29<sup>b</sup></b>	<b>-0.32<sup>a</sup></b>	<b>-0.35<sup>b</sup></b>
May-Sep	-0.20	-0.23	<b>-0.40<sup>a</sup></b>	-0.22	<b>-0.33<sup>b</sup></b>	-0.21	-0.06
Annual	<b>-0.25<sup>c</sup></b>	<b>-0.25<sup>c</sup></b>	<b>-0.51<sup>a</sup></b>	<b>-0.27<sup>c</sup></b>	<b>-0.40<sup>a</sup></b>	<b>-0.36<sup>a</sup></b>	<b>-0.27<sup>c</sup></b>
b) Correlation coefficients of air temperature.							
	Allalin	Gietro	Gries	Hohlaub	Schawzberg	Silvretta	Clariden
Oct-April precipitation	96.69	130.90	116.80	62.70	102.34	131.95	167.76
May-Sep temperature	<b>-174.30<sup>b</sup></b>	-123.60	<b>-325.32<sup>a</sup></b>	<b>-231.5<sup>c</sup></b>	<b>-317.78<sup>a</sup></b>	-175.38	-58.68
Intercept	-318	-648.60	-409.60	-89.46	567.42	-500.80	-776.65
% of explained variability	10.00	6.00	23.00	9.00	19.00	9.00	5.00
c) Coefficients of multiple regression.							

A multiple linear regression model is applied to Oct-April precipitation and May-Sep temperature to assess the combined impact of these two components on annual mass balance. The results indicate that the Oct-April precipitation effect is weaker than the May-Sep temperature effect (Table 2-6c), meaning that at a given precipitation level, the temperature has a stronger, more negative association with the annual balance. Among the glaciers, Ba of Clariden is more highly influenced by Oct-April precipitation ( $r= 0.27$ ,  $p<0.05$ ) than May-Sep air temperature ( $r= -0.06$ ), whereas Ba of Gries and Schwarzberg glaciers have a significantly inverse relationship with May-Sep temperature,  $r= -0.40$

( $p < 0.01$ ) and  $r = -0.33$  ( $p < 0.05$ ), respectively. This is also indicated by the percentage of explained variance.

### **2.5.3.2 Large-scale atmospheric circulation**

The selected glaciers and the two other glaciers in the central and eastern Alps, Clariden and Silvretta, showed a regional consistency of mass loss throughout 20th century. Therefore, it is important to further examine the relationships between seasonal components of glaciers mass balance and large-scale North Atlantic atmospheric circulation and ocean surface temperature conditions. Due to high frequency variations in the atmospheric indices, a 7-year triangular moving average smoothing technique is applied prior to calculating the correlations.

The correlation analysis indicates that there is predominantly positive relationship between winter mass balance and seasonal and the annual teleconnection patterns (Table 2-7). Although the corresponding values are not highly significant, there are negative correlations between winter mass balance and Oct-April GBI and May-Sep Hurrell NAO. The correlation between summer balance and the selected indices are mostly significant ( $p < 0.05$ ). A strong relationship is found between seasonal and annual components of AMO and EA indices and summer mass balance with the correlation coefficients of -0.86 and -0.88 ( $p < 0.05$ ), respectively. The ten lowest  $B_s$  had summer AMO and EA mean values of 0.22 and 0.46, respectively. Further, summer GBI index is significantly anticorrelated with summer mass balance patterns in Switzerland. The summer GBI tends to direct the North Atlantic storm track and associated moisture over Northern Europe and concurrently

influence a warming and drying effect over much of the central/southern continent (Hanna et al. 2016).

In contrast to other indices, both May-Sep  $NAO_{CPC}$  and SCA show a positive correlation with summer mass balances,  $r_s = 0.69$  and  $0.66$  ( $p < 0.05$ ), respectively. However, the lagged associations between the teleconnections and summer and annual mass balance should be taken into account, as cold season precipitation (presumably snow) influences the melt rates the following summer.

**Table 2-7** Spearman correlation coefficients of  $B_w$ ,  $B_s$  and  $B_a$  versus seasonal and annual indices, a-b specifies the significance level of correlations at 0.05 and 0.10 levels, respectively.

Index	$B_w$			$B_s$			$B_a$		
	Oct-April	May-Sep	Annual	Oct-April	May-Sep	Annual	Oct-April	May-Sep	Annual
AMO	-0.08	0.01	-0.05	<b>-0.80<sup>a</sup></b>	<b>-0.86<sup>a</sup></b>	<b>-0.86<sup>a</sup></b>	<b>-0.79<sup>a</sup></b>	<b>-0.82<sup>a</sup></b>	<b>-0.85<sup>a</sup></b>
NAO_CPC	<b>0.30<sup>a</sup></b>	-0.16	<b>0.26<sup>b</sup></b>	<b>-0.41<sup>a</sup></b>	<b>0.69<sup>a</sup></b>	0.06	<b>-0.26<sup>b</sup></b>	<b>0.61<sup>a</sup></b>	0.17
NAO_Hurrell	<b>0.35<sup>a</sup></b>	<b>-0.25<sup>b</sup></b>	<b>0.30<sup>a</sup></b>	-0.15	<b>0.39<sup>a</sup></b>	-0.04	-0.02	<b>0.31<sup>a</sup></b>	0.06
GBI	<b>-0.34<sup>a</sup></b>	0.13	-0.15	<b>0.33<sup>a</sup></b>	<b>-0.68<sup>a</sup></b>	<b>-0.51<sup>a</sup></b>	<b>-0.44<sup>a</sup></b>	<b>-0.61<sup>a</sup></b>	<b>-0.55<sup>a</sup></b>
SCA	-0.03	-0.21	-0.17	<b>0.33<sup>a</sup></b>	<b>0.66<sup>a</sup></b>	<b>0.56<sup>a</sup></b>	<b>0.25<sup>b</sup></b>	<b>0.59<sup>a</sup></b>	<b>0.47<sup>a</sup></b>
EA	0.14	0.03	0.07	<b>-0.86<sup>a</sup></b>	<b>-0.82<sup>a</sup></b>	<b>-0.88<sup>a</sup></b>	<b>-0.79<sup>a</sup></b>	<b>-0.77<sup>a</sup></b>	<b>-0.81<sup>a</sup></b>

In addition to the correlation between summer and winter balances, we also examined the relationship between annual balance and teleconnection patterns. In general, seasonal and annual AMO, GBI, and EA are negatively related to the annual balance of the Swiss glaciers. In comparison with the other indices, we conclude that the summer and annual balance of the Swiss glaciers are largely driven by AMO and EA behaviors (Table 2-7). Figure 2-10 highlights this strong association between summer mass balance and summer AMO ( $r = -0.86$ ), and annual EA ( $r = -0.88$ ). This is well corroborated by Huss's (2010a) findings showing that the decadal AMO and mass balance exhibit a strong, negative

correlation of -0.78. Our findings similarly suggest that the positive (warm) North Atlantic sea surface temperature (SST) anomalies amplify glacier mass losses, perhaps through warmer regional air temperatures and increased rain versus snow at high altitudes, whereas negative (cool) SST anomalies are associated with cooler air temperatures, more snowfall, and periods of positive mass balance.

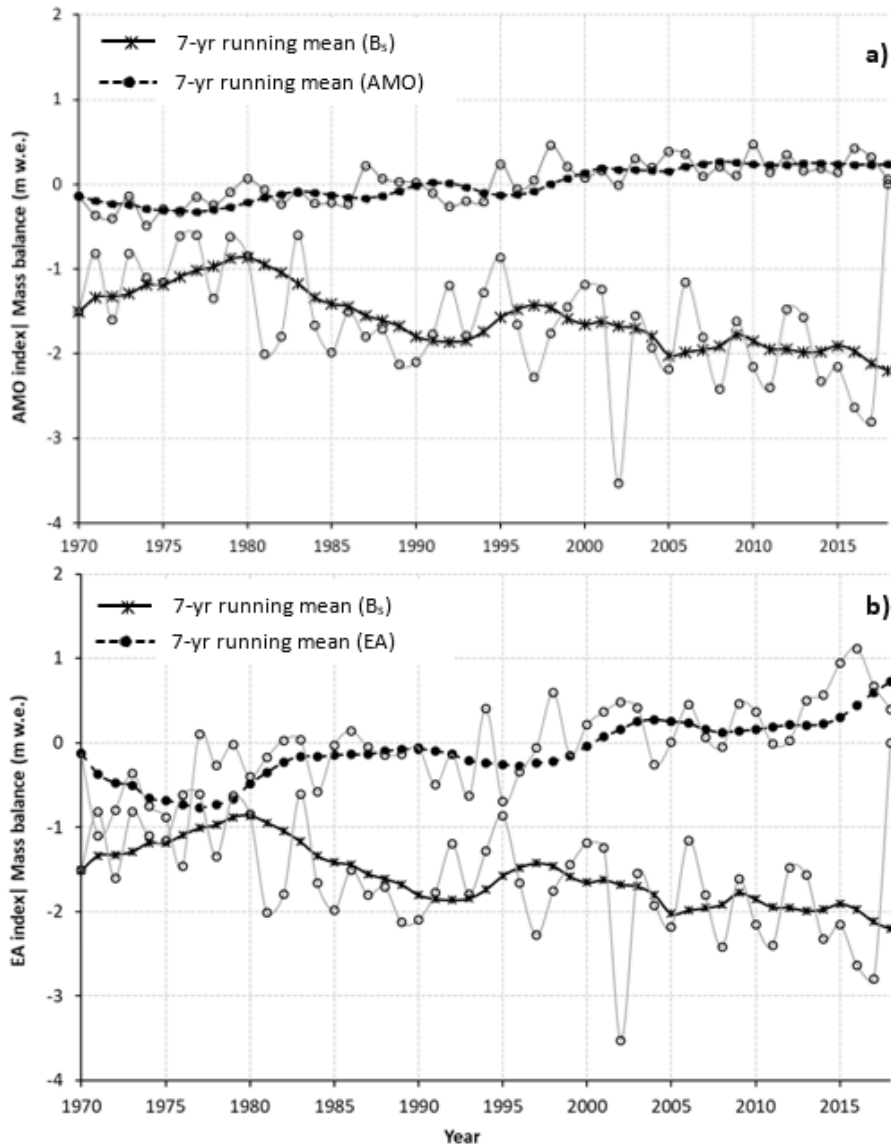


**Figure 2-10** The relationship between the summer Atlantic Multidecadal Atlantic Ocean (AMO) (a) and annual East Atlantic (EA) (b) indices versus summer mass balance from 1970 to 2017, with strong correlations coefficients of -0.88 and -0.86 ( $p < 0.05$ ), respectively.

The oceanic surface temperature conditions are linked to the mass balance of the Swiss glaciers through atmospheric circulation. For instance, under a positive NAO regime, low pressure over Iceland and high pressure over the Azores work in tandem to promote a zonal jet stream and westerly winds that transport warm, moist air from the North Atlantic Ocean to continental Europe. Comas-Bru and McDermott (2014) noted the association of positive NAO, EA and SCA indices with below-normal winter precipitation and colder winters in southern Europe. The authors also examined the relationship between the indices and found that winter precipitation patterns are affected by the state and combination of NAO with either the EA or the SCA; NAO and EA patterns of the same sign coincide with poleward migration of the Icelandic Low and Azores High over North Atlantic waters.

When positive phasing occurs between the patterns, the northward shifted jet stream leads to decreased precipitation over central and southern Europe. On the other hand, in-phase NAO and the SCA patterns tend to coincide with low pressure atop Greenland with the subtropical high situated over Western Europe. This meridional jet stream configuration produces southwesterly flow and increased precipitation across Scotland and northern Scandinavia while drier conditions persist across much of central Europe (Comas-Bru and McDermott 2014). These spatial precipitation patterns, in part modulated by the aforementioned ocean-atmosphere climate modes, explain the strong anticorrelation found herein between the EA pattern and Swiss glaciers' mass balance characteristics (e.g. positive EA tends to yield less precipitation to the region). Future work will further explore observed seasonal mass balance responses to teleconnection phasing and related ocean-atmosphere interactions.

## 2.5.4 Hypsometric characteristics

Hypsometric analyses of the studied glaciers provided some new insights. Figure 2-11 provides the comparable hypsometric profiles, Figure 2-12 presents the DEMs, and Figure 2-13 provides the detailed hypsometric distribution of the glaciers. In Table 8, we compile their HI and corresponding shapes. Before we start the discussion on these results, we would like to reiterate that the two DEMs used for this analysis based on availability defer in their origin and base data, spatial resolutions, accuracy, and processing steps and the results should be analyzed accordingly.

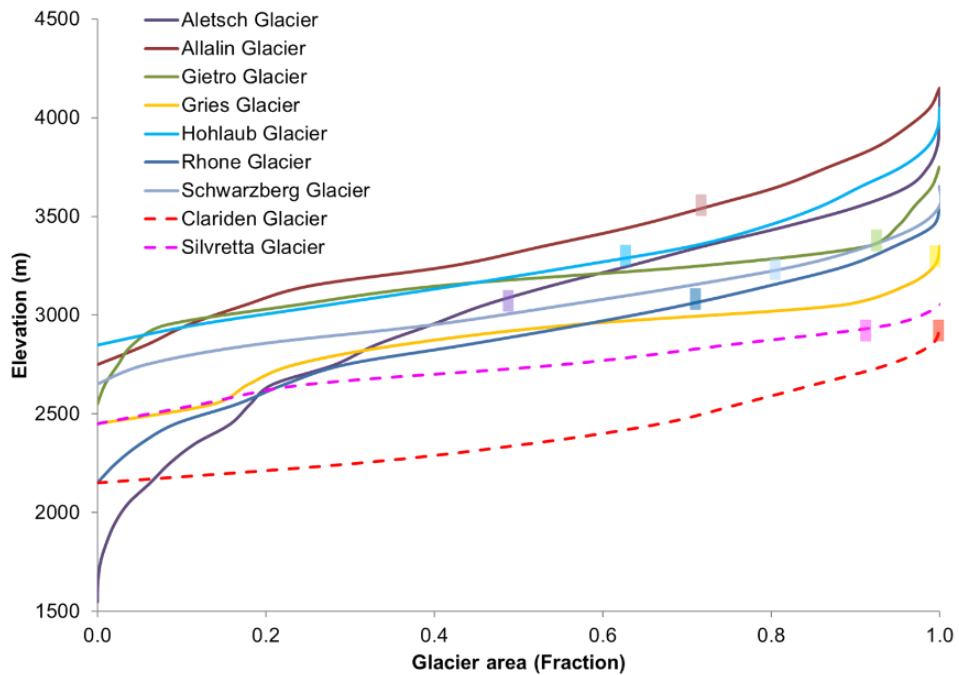


**Figure 2-11** Comparable hypsometric profiles for all the glaciers. The colored boxes for each profile mark the ELA for the respective glacier. The dashed curves represent the two glaciers outside the Rhone catchment.

The outcomes of this analysis support several of the results discussed above. For example, as explained in Section 2.5.1, the rates of change in mass balance after break years (1980s) become negative for Allalin and Hohlaub. Both of them are bottom-heavy

glaciers with N-NE facing aspects (Figure 2-11, Figure 2-13, and Table 2-8). For Gietro and Silvretta, the rates significantly changed from -200 to -1000 mm w.e., indicating heavy mass-loss for these glaciers in near future. Interestingly, these two are the only equidimensional glaciers in our study sample and both have N-NW aspect (**Error! Reference source not found.**, Table 2-8).

Similarly, the correlation analysis for  $B_a$  of glaciers as presented in Section 2.5.1 reveals significant correlations and two distinct classes. Silvretta, Gries, and Gietro can be categorized into one group as per these correlations and these glaciers show equidimensional or top-heavy morphologies. Allalin, Schwarzberg, and Hohlaub show better correlations with each other and interestingly all three of them display bottom-heavy or very bottom-heavy morphologies. Aletsch is the only glacier with ELA below the mean elevation (Figure 2-11) and the balanced state of this glacier is well-supported by its very top-heavy morphology (Table 2-8). The dashed curves in Figure 2-11 represent the two glaciers outside the Rhone catchment and the remarkably distinct morphologies of these two glaciers (Figure 2-12) are apparent in the shapes of the curves. Silvretta, in particular, is located in a very narrow elevation range of 672 m and its hypsometric curve is nearest to a straight line, highlighting its equidimensional shape. Figure 2-13 displays more detailed hypsometric curves for the glaciers and the three glaciers with highest AAR (Table 1), i.e., Aletsch, Rhone, and Schwarzberg, have similar S-shaped curve distinct from rest of the glaciers. A comparative analysis between Clariden and Gries reveal another interesting facet. Both of these glaciers are within ~2400-3300 m, have similar area, and NE facing aspect (Table 2-1). Clariden displays a convex curve making it very bottom-

heavy while Gries has a distinct concave profile for majority of its middle elevations, thus making it a top-heavy glacier (Figure 2-13).

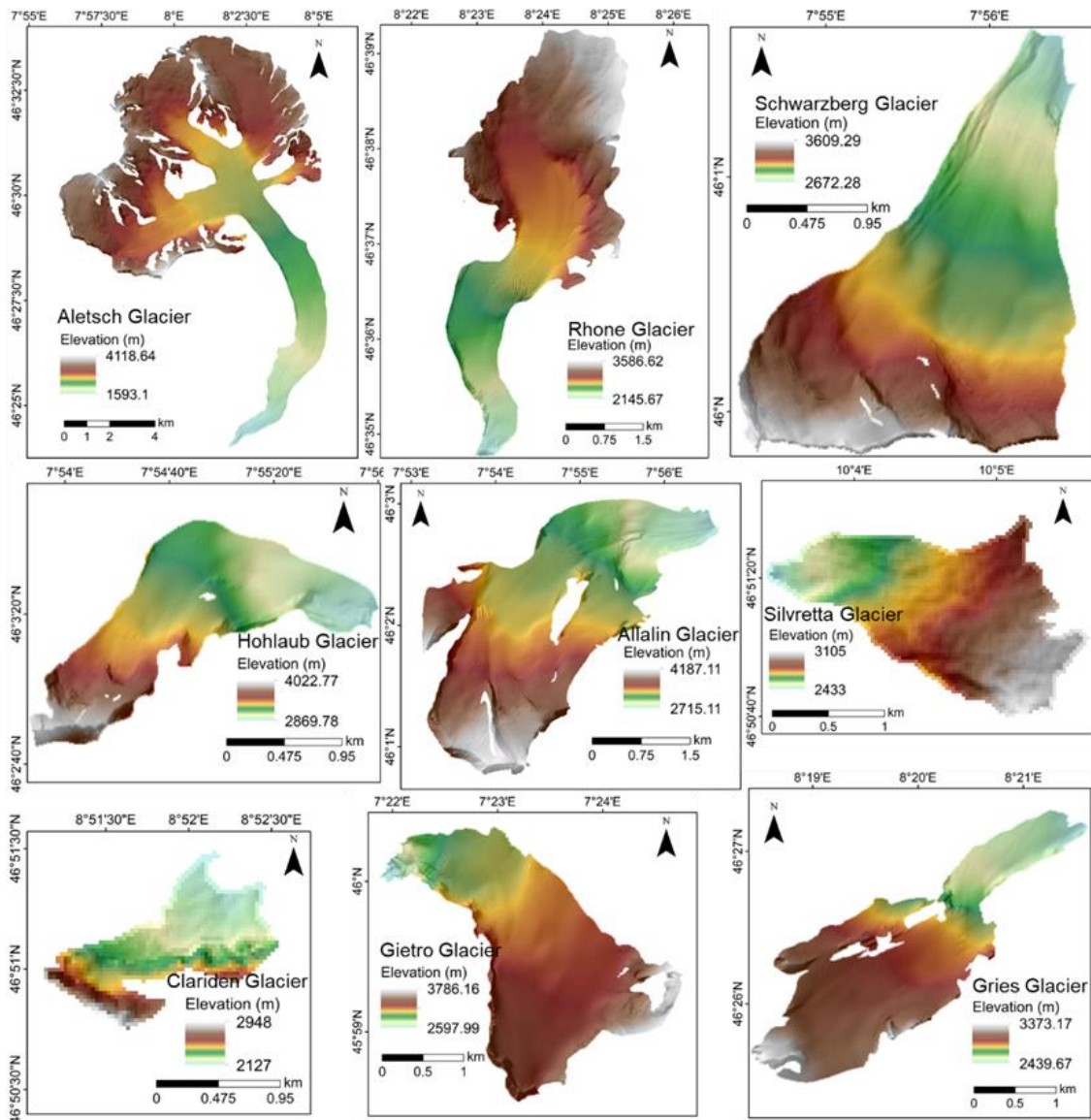


**Figure 2-12.** The elevation maps of the selected glaciers.

During the accumulation season, Clariden on an average showed highest accumulation of 1385 mm w.e. while in the same period, the lowest average annual mass balance of -919 mm w.e. was recorded for Gries. Similarly, the mean AAR in this period was least for Gries 26% and highest for Clariden (56%). The very bottom-heavy

morphology of Clariden combined with its significantly gentler slopes than Gries (Figure 2-12) for majority of the glacier area and significant winter accumulation translates into one of the best coupling between  $B_a$  and  $B_w$  among the studied glaciers (Table 2-4).

**Table 2-8.** HI and glacier categories.

Glaciers	HI	Glacier Category
Aletsch	-1.62	very top-heavy
Allalin	1.26	bottom-heavy
Gietro	-1.16	equidimensional
Gries	-1.32	top-heavy
Hohlaub	2.06	very bottom-heavy
Rhone	-1.24	top-heavy
Schwarzberg	1.41	bottom-heavy
Clariden	3.11	very bottom-heavy
Silvretta	-1.06	equidimensional

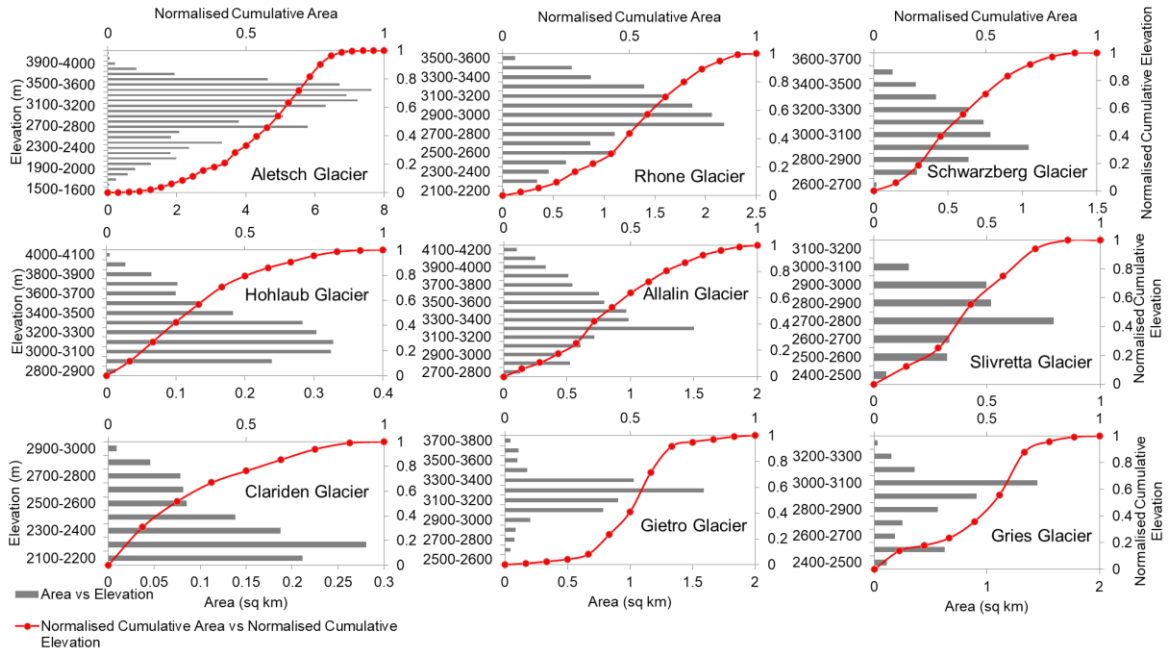


**Figure 2-13.** Hypsometric curves of selected glaciers.

Thus, these observations highlight that although local climate parameters are playing a significant role in determining the glacier mass balance in the region, the observed correlations and mass balance trends are in agreement with the hypsometric distribution and morphologies of the glaciers. The morphological changes in future due to continued mass loss in these glaciers have the potential to further accelerate the rate and trend of negative mass balance.

## **2.6 Conclusions**

This study investigated and provided updated analyses of long-term annual and seasonal mass balance time series of glaciers across the Swiss Alps. The purpose of this analysis was to identify trends/changes in the mass balance series and study the relationship between the components of mass balance, and local climatic variables and large-scale oceanic and atmospheric patterns. The most prominent result of this research is the significant glacier mass loss and acceleration in ablation due to the warming signals influenced by local and regional climatic patterns. According to the results emerging from the analysis, the following conclusions can be reached:

- All selected glaciers have lost their equilibrium condition in the recent century and the persistent negative annual mass balance trends, accompanied by decreasing AARs, have been observed for the glaciers located in the south of Switzerland. However, the Ba of largest glacier, Aletsch, has fluctuated close to “balance” in comparison with the other glaciers surveyed.
- Such imbalanced behavior is substantially the product of increase in ablation induced by warmer temperatures, increased melting, and acceleration of the ice-

albedo feedback process. Although the precipitation trends are not significant, the increase in the number of days with the air temperature above 0°C signifies reduction in solid precipitation over the glaciers.

- The glaciers analyzed reveal that the annual mass balances are mainly controlled by the summer mass balance, which is statistically attributed to the significant anticorrelation with May-Sep air temperature.
- Forecasting results suggest that the smaller glaciers are reacting faster due to the inability to adjust to the mass balance losses as well as increases in longwave heat input from adjacent bare slopes.
- Atmosphere-ocean teleconnection patterns and their behaviors, including AMO and EA, are strongly linked through the time to mass balance characteristics of the southern Swiss Alps and these large-scale climatic forcings will likely continue to influence surface mass balance regime.
- Most of the observed glaciers are losing accumulation area given that AAR percent has dropped from approximately 75% in 1970 to 25% in recent years, stressing the rate of melt acceleration.
- Based on the current research and the corresponding results, the negative mass balance trends cannot be simply attributed to the direct response of global warming. Hence, we emphasize that future investigations should focus on resolving complex and indirect surface-atmosphere interactions (e.g. reflectivity and impurities of glacier surfaces (Naegeli et al. 2019) to more comprehensively understand physical processes driving glacier mass balance variability and change. In particular, the hypsometric evolution of glaciers with continued mass loss warrants for

considering dynamic modeling approaches to simulate future state of glaciers as we observe glacier hypsometry and morphology playing considerable role in defining the mass balance trends.

### **3 GLACIER FACIES AND DEBRIS-COVERED SURFACES OF BERNESE ALPS – REMOTE SENSING APPLICATION: LANDSAT 8 OLI & TIRS**

#### **3.1 Introduction**

Glacier surfaces are spatiotemporally dynamic owing to variability and change in meteorological parameters including type and amount of precipitation, air temperature, and insolation, as well as presence of supraglacial debris cover during a mass balance year (Williams et al. 1991; Bhardwaj et al. 2015). The supraglacial debris cover moves with the glacier flow towards the ablation area and is an important part of the sediment transportation system. This thick layer includes all groups of mass movements from debris flows to rockfalls, snow/ice avalanches from the surrounding steep slopes, and rock outbreaks. Some studies have also revealed the role of this layer in supraglacial lake formation, decreasing the melt rate and the consequent delay in glacier feedbacks to climate impacts (Fountain et al. 2000; Reid and Brock 2010; Banerjee 2017; Nicholson et al. 2018; Fyffe et al. 2019). Therefore, monitoring and updating records of dynamic glacier facies can improve the accuracy of studies related to mass balance modelling, lake formation, and glacier response to meteorological and climate variables.

Advances in remote sensing technologies, including improved spatial and radiometric resolutions as well as improvements in high-resolution Digital Elevation Models (DEMs) since the 1970s has facilitated characterization and monitoring of remote areas. Several automated and semi-automated techniques have been developed and assessed for mapping glacier facies. Although these methods have been successful in mapping clean ice and snow, they lack accuracy when delineating debris-covered surfaces due to similar spectral response with the valley rock materials. Hence, the commonly

applied methods can be categorized into: i) manual digitization from satellite images (Paul et al. 2002); ii) automatic classification of multispectral images (Bishop et al. 1999); iii) thermal-based methods (Ranzi et al. 2004); vi) geomorphometric-based methods (Bolch and Kamp 2005); and v) a combination of methods i-vi (Karimi et al. 2012; Alifu et al. 2015; Bhardwaj et al. 2015). The manual method is the most accurate method, but is time-consuming, and the accuracy is highly dependent on the image quality. Moreover, manual delineation is subjective and relies on expert knowledge of accurate identification and facies classification. Using multispectral imagery also presents some limitations for mapping glacier facies, particularly regarding band saturation in high albedo regions which has resulted in misdetection of sub-surface facies (including wet/dry snow as well) (Bhardwaj et al. 2015). Williams et al. (1991) investigated the capability of Landsat in terms of glacier facies classification with details about the sub-surface information, and Bhardwaj et al. (2015) built upon Williams et al. (1991) to create a new Landsat 8 band ratio based on the reflective and emitted spectral characteristics of glacier facies.

Another challenge related to mapping temperate alpine glaciers, is the spatial extent and supraglacial debris, due to similar spectral response of this class to periglacial debris. Temperate glaciers are the glaciers at melting point implying the flow of water through crevasses and moulins with minimal freezing reaching to glacier bed where it comes to the contact with debris cover of glacier surface (Fountain 2011). To overcome these challenges, Alifu et al. (2015) proposed a new ratio band for mapping supraglacial debris using Landsat Enhanced Thematic Mapper Plus, Landsat Thematic Mapper imagery and Shuttle Radar Topography Mission (SRTM) data. They proposed a band ratio of (Thermal Infrared/ (Near Infrared/Short Wave Infrared)) as an initial product to map facies. They

then applied a threshold to the index and overlaid it on a binary slope map, which resulted in high accuracy and a good agreement with the reference data (only 0.34-2% difference between the reference glacier outlines and the mapped ones).

Remote sensing techniques have been also established for differentiating ice and snow surfaces. Rabatel et al. (2013) used the relationship between snowline and equilibrium line altitude at the end of summer to reconstruct the annual mass balance series for glaciers located in France. In this study, the equilibrium line altitude (May-August) calculated from field measurements was compared with snow line extracted from satellite images. They concluded that measured snow line during the dry season (May to August) provides a good assessment of the annual equilibrium line altitude for glaciers in temperate regions. Rango et al. (1975) used Landsat 1 Multi-spectral Scanner (MSS), including band 5 (Red) and band 7 (Near-Infrared (NIR)), and delineated snow-cover by means of manual transparent overlay.

Hall et al. (1987) applied a band ratio (band 4/band 5) on Landsat 5 Thematic Mapper (TM) for enhancement of snow and ice surfaces due to large spectral response differences between these two, where band 4 (NIR) recorded high digital numbers (DNs) over ice and snow areas and band 5 (SWIR (Short-wave Infrared)) low DN.

Although the utility of Landsat 7 data to map glacier facies has been addressed in previous studies, this study aims at investigating limitations and strengths of Landsat 8 Operational Land Imager (OLI) and Thermal Infrared Sensor (TIRS) data for classification of glacier facies, particularly debris-covered areas of alpine valley glaciers located in the Bernese Alps, Switzerland, in order to be used as an input for future assessment of lake formation and associated hazards and risks.

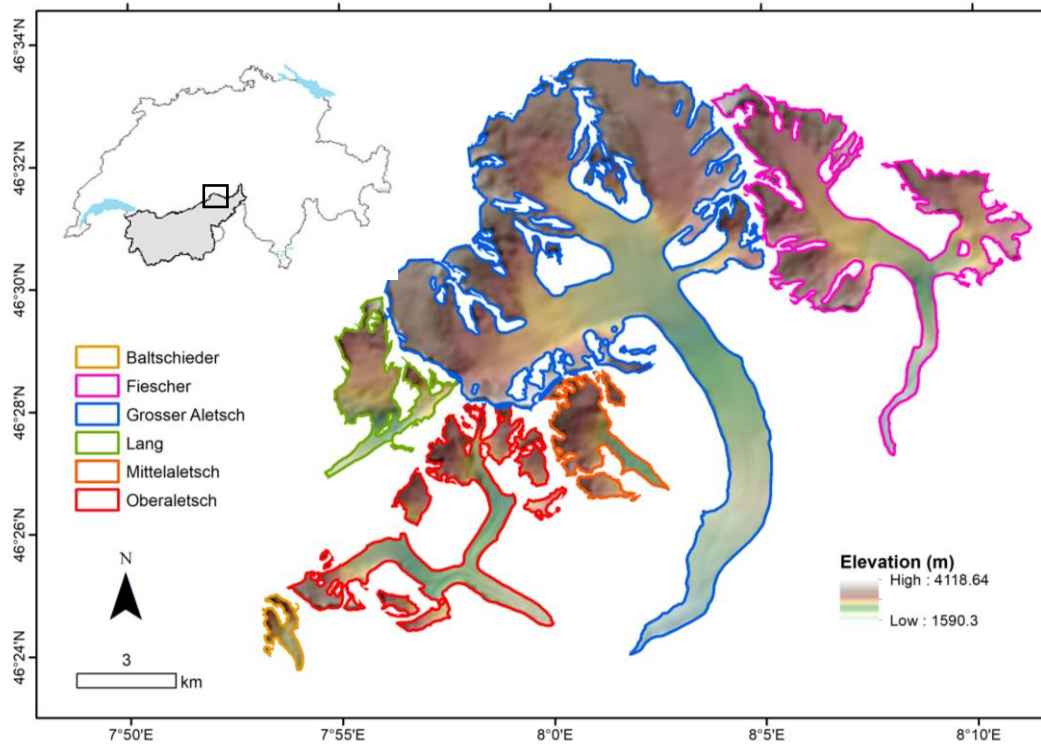


**Figure 3-1** The six selected glaciers of the Bernese Alps are located in Rhone catchment, southwestern Switzerland (Source: SGI 2010 and swissALT<sup>3D</sup>).

### 3.2 Case study

Six glaciers of Bernese Alps in the Rhone catchment, located in the canton of Valais in southwestern Switzerland, were selected for mapping the glacier facies and the debris-covered area. Despite different geo-morphometric parameters (e.g. slope, aspect, and curvature) and altitudinal bands, similar climatic conditions are found at each glacier. The elevation of corresponding glaciers ranges from 1600 to 4120 m a.s.l. The largest glacier in this group is Grosser Aletsch, which covers 77.32 km<sup>2</sup>, with a length of 23 km.

Spectral characteristics of these surfaces were investigated along the western arm of Oberaletsch Glacier (Fig 3-1 & Fig 3-3). The glacier extends from 46° 23' 45" N to 46° 33' 44" N and 7° 53' 6" E to 8° 11' 22" E, in which the western and eastern arms join at the

eastern base of Nesthorn and then flows to the south-east, where the terminus region ends at 2,156 m a.s.l. before reaching Aletsch.

### 3.3 Data and methodology

#### 3.3.1 Landsat data processing

Landsat 8 data were acquired at the end of summer season, to prevent the seasonal snow or cloud cover over the glacier areas. Level 1 data were ordered from the USGS EarthExplorer (USGS; <http://earthexplorer.usgs.gov/>). The 25 August 2016 scene was nearly cloud free with 5.59% cloud cover (Table 3-1).

**Table 3-1** Details of Landsat 8 data

Landsat scene ID: LC81940282016238LGN01			
Date/time of acquisition: 08.25.2016/10:10:52.2244400Z			
WRS path: 194; WRS row: 28			
Cloud Cover: 5.59; Image quality OLI: 9; Image quality TIRS:9			
Sun azimuth: 149.74989698°; Sun elevation: 51.05758564°			
<b>Operational land imager (OLI)</b>			
Band	Name	Wavelength ( $\mu$ )	Spatial resolution (m)
1	Coastal/aerosol	0.43-0.45	30
5	Near infrared	0.85-0.88	30
6	Short wave infrared	1.57-1.65	30
8	Panchromatic	0.50-0.68	15
9	Cirrus cloud	1.36-1.38	30
<b>Thermal infrared sensor (TIRS)</b>			
10	Thermal band 1	10.6 - 11.19	100

The glacier outlines were obtained from the new Swiss Glacier Inventory 2010 (SGI2010), which was derived by manual digitization of high-resolution (25cm) aerial orthophotographs acquired between 2008 and 2011 (Fischer et al. 2014). Higher resolution imagery with the same acquisition date of the Landsat scene was available on Google Earth in order to update the glacier boundaries and validate the results.

The applied methodology for mapping the glacier facies is illustrated in Figure 3-2. The OLI DNs were converted into top-of-atmosphere (TOA) reflectance and TIRS, band 10, into ‘at-satellite brightness temperature in degrees’ in Kelvin given the equations provided on the USGS website (<https://www.usgs.gov/land-resources/nli/landsat/using-usgs-landsat-level-1-data-product>) and included in the model (Eq. (1&2)):

$$\rho_{\lambda} = M_{\rho}Q_{cal} + A_{\rho} / (\sin(\theta_{SE})) \quad 1)$$

$$T = K_2 / \ln (K_1 / (M_L Q_{cal} + A_L) + 1) \quad 2)$$

where:  $\rho_{\lambda}$  = TOA planetary reflectance;  $M_{\rho}$ ,  $M_L$  = Band-specific multiplicative rescaling factor from the metadata (REFLECTANCE\_MULT\_BAND\_x), where x is the band number);  $Q_{cal}$  = Quantized and calibrated standard product pixel values (DN);  $A_{\rho}$  and  $A_L$ =Band-specific additive rescaling factor from the metadata (REFLECTANCE\_ADD\_BAND\_x), where x is the band number); and  $\theta_{SE}$  = local sun elevation angle of scene center in degrees; T = at-satellite brightness temperature in degrees Kelvin; and  $K_1$ ,  $K_2$ =Band-specific thermal conversion constant from the metadata.

### 3.3.2 Delineation and clipping glacier extent

The Google Earth imagery and the recent Swiss Glacier Inventory (SGI2010) were used to delineate the glacier extent. Due to high accuracy of the SGI2010 database and the recent updates of glacier boundaries, the manual delineation of the glaciers in the study area was avoided. However, Google Earth images with similar month dates to the Landsat image were used for the manual updates on the glacier boundaries. The glaciers (Fig 3-2) were then clipped based on the modifies boundaries, including only glaciers from the

Landsat satellite scene and delimiting the non-glacier areas. Next, the output was used to select the bands and band ratios for mapping the facies and debris-covered surfaces (Fig 3-2).

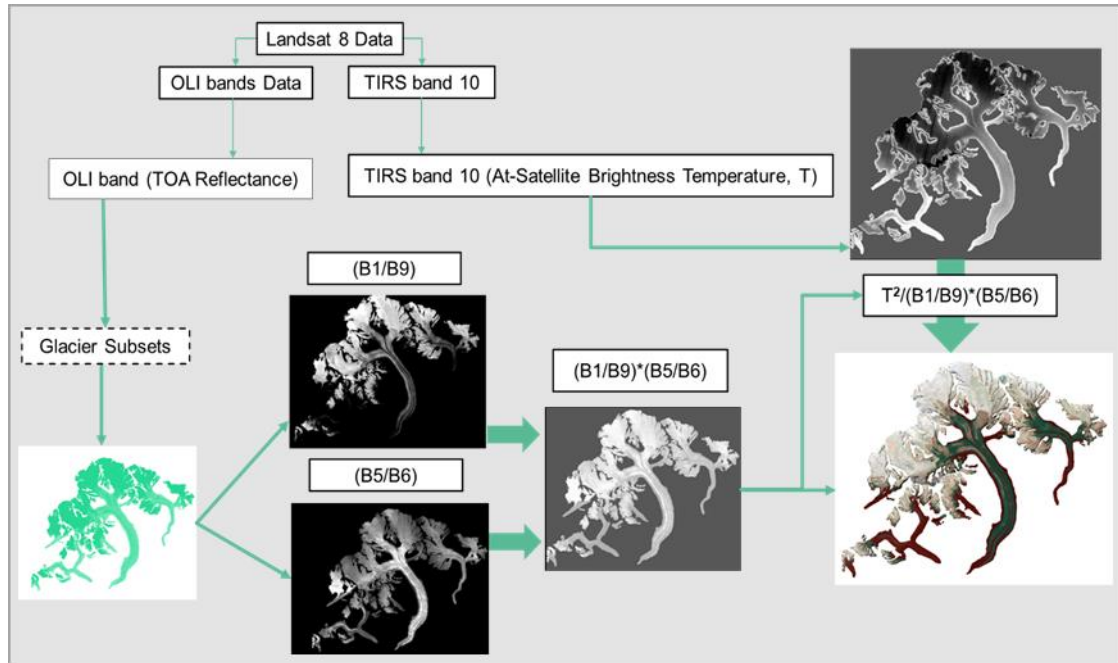


**Figure 3-2** A flow chart of processing steps for mapping the glacier facies and debris cover area.

### 3.3.3 Band selection and image thresholding

To determine the best bands/band ratios for facies classification, a line transect representing all types of facies (snow, clean ice, mixed ice, slush zones and debris-covered surfaces) were generated over the western arm of Oberaletsch Glacier, using ‘Creating a spatial profile’ tool in ERDAS IMAGINE. The corresponding spectral profiles and histograms were also created, and the spectral characteristics of facies and debris-covered areas were visually and quantitatively compared for the band selection.

### **3.3.4 Classification of glacier surface**

The glaciers were classified by thresholding the new imagery resulted from the band ratios processing (Fig 3-2). We applied the density slicing method to determine the class ranges for glacier classification. The density slicing method combines DN values of various values within a range into a single class. This method is effective, especially when DN values over a given surface form a unique and typically narrow set (Short, 1999). If there are several surfaces with different discrete DN values, then several level slices are established, in which each slice classifies the spatial distribution of its corresponding feature (Short 1999). Accordingly, the entire pixels within a 'slice' are assumed to correspond to the same class (i.e. 'snow', 'clean ice', 'supraglacial debris cover', etc.).

### **3.3.5 Accuracy assessment**

The Google Earth images with the same acquisition date of the Landsat scene, and SGI2010, which was obtained from the manual delineations of the high-resolution aerial orthophotographs, were utilized to assess the validation of the results from this study. The vector format of all classes was overlaid onto Google Earth images providing a visual comparison.

## **3.4 Results and discussion**

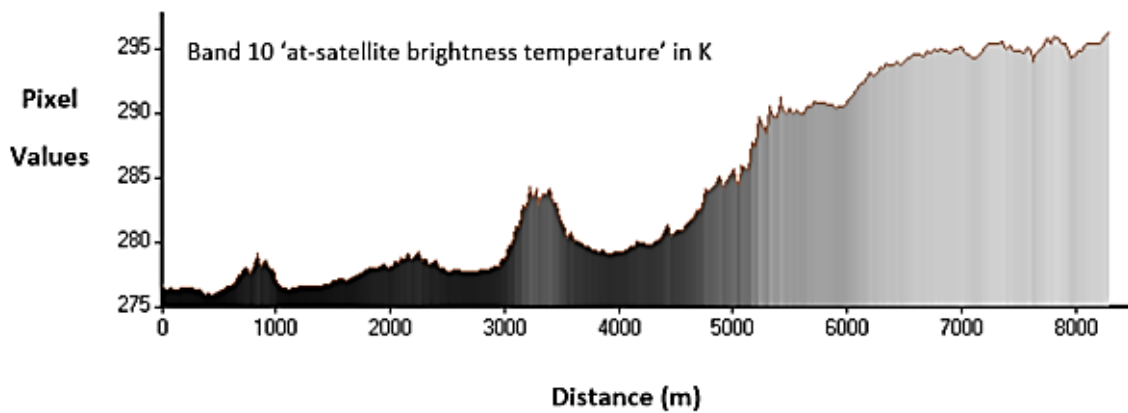
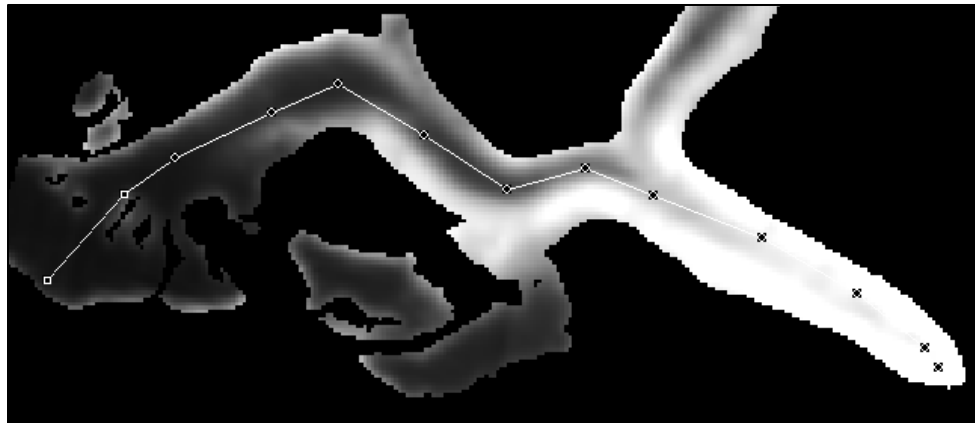
### **3.4.1 Results of band/ratioing selection**

From the histogram comparison, Band 1 (coastal aerosol, 0.43-0.45( $\mu$ )) was selected over Band 2 (blue, 0.45-0.51( $\mu$ )) due to the sharp changes and capability to capture similar reflectance characteristics. From the histogram visualization of Band 1, it showed a low

reflectance for debris-covered area compared to the other bands. The histograms of Band 3 (green, 0.53-0.59 ( $\mu$ )) and Band 4 (red, 0.64-0.67( $\mu$ )) were similar, but Band 5 (NIR, 0.85-0.88 ( $\mu$ )) could detect ice beyond the snow line, where a peak appeared after 0.6. Therefore, it was selected as a band to differentiate the pure ice from the mixed ice. According to William et al. (1991), SWIR bands are very sensitive to snow grain size. As Band 6 (SWIR1, 1.57-1.65( $\mu$ )) and 7 (SWIR2, 2.11-2.29 ( $\mu$ )) showed a higher reflectance in debris-covered areas and very low reflectance over snow/ice surfaces (Fig 3-4). Thus, Band 5 and 6 ratios were selected to differentiate snow and ice from other surfaces (Fig 3-5). Band 9 is the narrowest SWIR band which is added in OLI of Landsat 8. Since it falls within the electromagnetic spectrum, the atmospheric transmission is almost zero, and the reflectance of almost all land features shows a sharp drop (Bhardwaj et al., 2015). Therefore, due to the high reflectance of snow and ice versus the debris-covered surfaces in this Band, snow and ice can be distinguished. From this observation of a narrow bandwidth, Band 1 and 9 were used to for detecting debris surfaces. Figure 3-4 characterizes the spectral reflectance of three different bands of Landsat 8 along a selected transect. Visible and NIR bands showed small variations in the parts of glacier than supraglacial debris. While SWIR bands 6 and 7 showed large variations for debris-covered areas. Band 9 (SWIR) featured a smooth profile for most of the zones, and was therefore, employed for normalization of Band 1 and a smooth thresholding classification map. The spectral profile of 'at-satellite brightness temperature' revealed a clear difference between various facies (Figure 3-4). In this regard, it was added to the final equation as a base for different zones divided by the selected ratios to enhance the OLI bands.



**Figure 3-3** An overview of the glacier facies a) Snow in accumulation area b) Crevasses/slush zone c) Clean ice d) Mixed ice with debris; and e) Debris-covered surface.



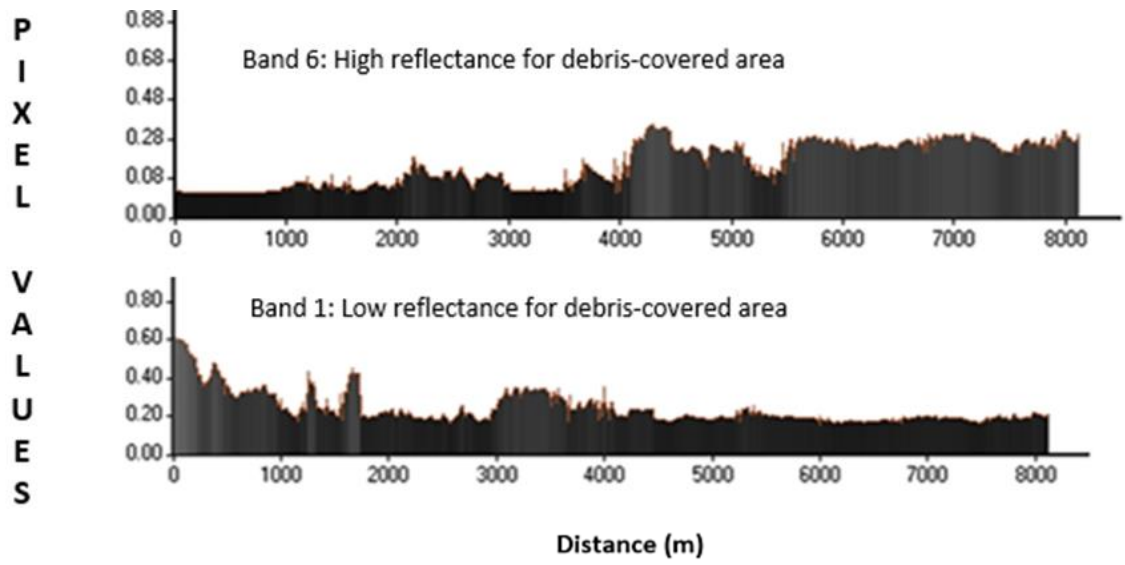


**Figure 3-4** Spatial profiles of Landsat 8 band 10, 6 and 1 for the selected glacier area (see Fig 3-3), the Y-axis shows the TOA reflectance of each pixel.





**Figure 3-5** a) Band 5, showing low reflectance, versus b) Band 6, showing high reflectance of debris-covered surfaces.

### 3.4.2 Glacier facies classification

Figure 3-6 is a modification of glacier-facies concepts defined by Müller (1962), Benson and Motyka (1979), and Williams et al. (1991), presenting the various components of glacier facies. According to this, the glacier facies within accumulation and ablation areas are separated by the equilibrium line. In temperate glaciers, the position of snow line at the end of mass balance year coincides with the equilibrium line, whereas in polar glaciers a superimposed ice zone, where ice forms from snow melt and refreezes over glacier ice, emerges between the snow line and equilibrium line. We adjusted William's approach for the Swiss Alps and defined the classes according Figure 3-7. From the applied ratio technique, we were able to distinguish four glacier facies including snow, clean ice, slush/crevasses, and mixed ice. Figure 3-8 represents the classified map showing glaciers

surface types and facies. Figure 3-8a shows these classes over the western arm of Oberaletsch Glacier and Table 3-2 shows the chosen pixel ranges for each surface. It is clear that mixed ice constitutes a large area of Great Aletsch glacier.



**Figure 3-6** Sequence in glacier facies (modified from Williams et al. 1991).

The slush zone, a transition zone between snow and glacier ice (Fig 3-3), have been extracted on the glacier surface at the time of image acquisition, during the ablation season of glaciers. This zone is a mixture of fresh snow and ice which generally results in a wet area and follows the snow line altitude. The presence of this zone is short and shifts with climate condition and can be mixed and misclassified by seasonal snow owing to quick melting with rising temperature.

The result of density slice, shown in Figure 3-8, was able to capture the debris-covered areas but contains several misclassifications for the ‘snow’ class into ‘dirt ice’ or ‘slush/crevasses’ in areas where bedrock outcrops of valley walls were present in shade or/and in higher altitudes (Figure 3-8b). This can be explained by the lower temperature of these outcrops in shade area compared to the surrounding pixels resulting in less spectral information. More particularly, supraglacial debris pixels in proximity to the accumulation zone illuminate lower temperatures, which can be explained by the position of these pixels at higher elevations. Further, the shadows on the original image (Figure 3-8b) should be taken into account as another source of errors in this classification. On the other hand, a

large area of debris-covered surface for Great Aletsch (Figure 3-1 & Figure 3-8), as the greatest and thickest glacier in the Swiss Alps, was correctly captured and validated through historical Google Earth imagery.



**Figure 3-7** Google Earth image of the western arm of Oberaletsch Glacier: a) Snow facies close to an arête in the accumulation zone, b) Crevasses over steep slopes turning clean snow into dark slush, c) Clean ice, d) Mix of ice and debris, e) Supraglacial debris cover with red arrow showing the position of ice wall at the tongue.

Many factors need to be considered in classification of glacier facies and debris-covered surfaces. The presence of any precipitation type can affect the accurate classification, especially for the crevasses and debris covered areas. Atmospheric conditions and the time of data acquisition are also regarded to impair the correct reflectance for differentiating snow and ice facies. Availability of the images free of clouds and seasonal snow, particularly in this subject that the time is constrained to August and September, is another challenging part of this research for obtaining high accurate results from the combination of optical and thermal bands. In addition, field observations for

validating the results was another limitation in order to reduce the mapping misclassification.

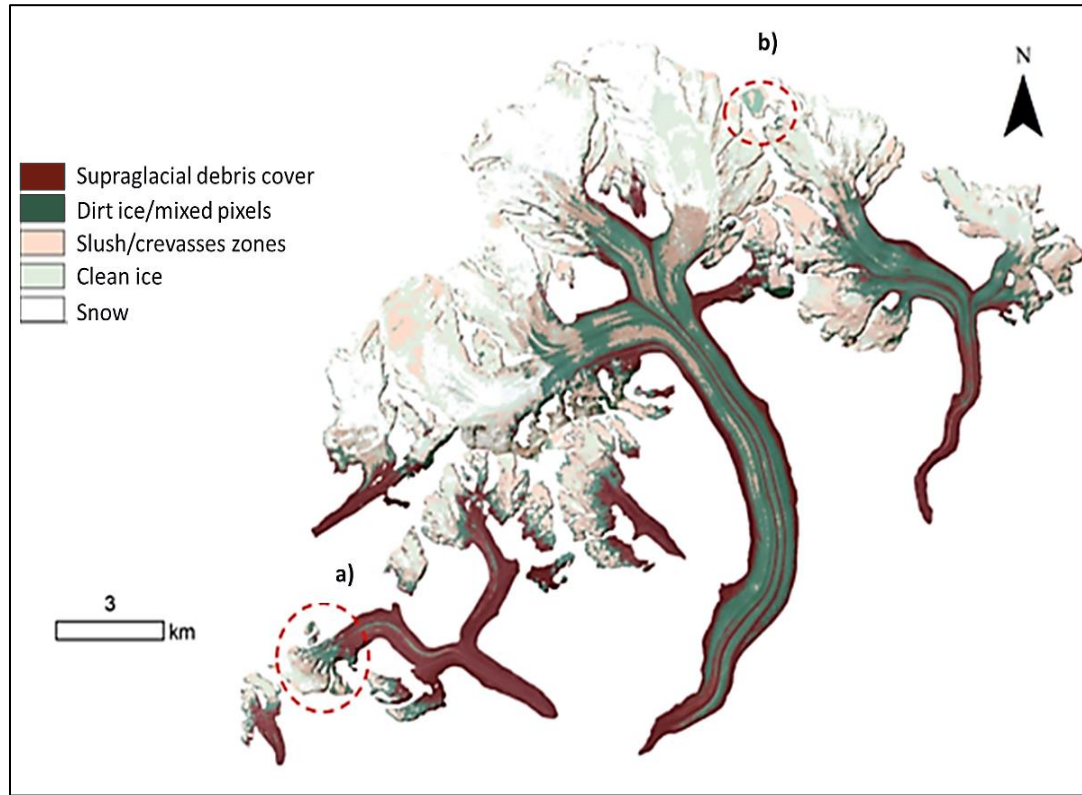


**Figure 3-8** b) The classified map with five surface types; a) Red ellipse shows a correct classification corresponding to the western arm of Oberaletsch Glacier (Fig 3-3); and b) shows misclassified snow class examples.

**Table 3-2** Pixel ranges for mapping glacier surfaces.

Class No.	Pixel ranges	Glacier surface class	Facies type
1	< 10.60	Supraglacial debris cover	-
2	10.60 – 13.80	Dirt ice	Ice
3	13.80 – 45.00	Slush/Crevasses	Transition zone from ice/snow
4	45.00 – 104.20	Clean ice	Ice
5	>104.20	Snow	Snow

The obtained results here used the methodology from the application on Himalayan mountains with field validation (Bhardwaj et al. 2015), but the classification was adjusted based on this research study area. According to the classified facies, optical and thermal bands of Landsat 8 with improved bandwidths could enhance the mapping of subtle features where both spatial and spectral resolutions are required.

### **3.5 Conclusion**

This study applied a ratio method from the available spectral and thermal data of Landsat 8, in order to classify the glacier facies for the selected glacier boundaries in Rhone catchment in Switzerland. The main purpose of this research was to apply the concept of glacier facies to address the capability of Landsat 8 with two narrow SWIR bands and one added thermal band. With observation of histograms and spectral profiles of OLI and TIRS bands, the reflectance and radiance of bands and ratios was monitored to examine the appropriate band ratios. The classification range was adjusted to capture the glacier surface type for this specific region. This method in comparison with recently developed approaches, has mixed both spectral and thermal characteristic of Landsat 8 to increase the contrast within the bands and accordingly enhance the classification. The method can be adjusted and enhanced based on the local conditions by considering geomorphometric parameters such as slope and elevation. Also delineating snow line as the 0°C temperature line can be a help in reducing the error within the misclassified area, especially the snow and slush zones. The previous research could capture the crevasses as a separate class from the slush zone, but we were not able to separate the class, therefore the slush zone and crevasses were categorized into one class.

The outcome is in good agreement for classification debris-covered areas and slush/crevasses zones. This approach applied here, requires a good understanding of the study area, the data and the applied reasoning. The free availability such datasets is noteworthy to expand the horizons of remote sensing application in geomorphology of glaciers and cryosphere environments. The results from this study can be used for modeling the mountain landscapes without glaciers and the potential lake formation sites for early monitoring of glacier hazards, especially the two classes, crevasses and debris-covered surfaces, that have impacts on lake formation and evolution. The output classes are robust for such applications, however, there is still room for optimization of this approach in future studies (i.e. including surface slope of glaciers, contour lines and the 0°C surface temperature line in the classification process).

## **4 POTENTIAL SITES OF FUTURE LAKES IN SWISS SOUTHWESTERN ALPS WITH VOLTA**

### **4.1 Introduction**

High-mountain regions are dominated by glacial and periglacial processes that are governed by climate conditions. Aside from the retreat of glaciers since the end of the Little Ice Age (1850), accelerated ice loss has been one of the most pronounced signs of changing climate in alpine environments around the world (Frey et al. 2010). According to climate change projections, this process is most likely to continue due to the late response of glaciers to climate and the ongoing rise in air temperature (Jawaid 2017). In response to temperature and precipitation fluctuations, it is also expected that glacier mass loss will continue to alter the geomorphic agents and the stability of slopes in high mountain areas (Huggel et al. 2004). As a result, high-mountain landscapes are transforming from glacial environments into new landscapes with rocks, debris, sparse vegetation, and lakes. The combination of these features can form a highly dynamic and hazardous condition for the population and assets downstream (e.g. lake outburst and dam failure by flood or debris flow events). Despite this fact, these proglacial lakes also have the potential to serve as geotourism attraction sites and water reservoirs (Maanya et al. 2016). Therefore, modeling the potential location of future lakes provides the responsible authorities with essential knowledge for timely water resource and hazard management in these areas.

Glacial lake formation is being observed in the majority of glaciated mountains in the world (Watanabe et al. 1994; Wang et al. 2013; Vilímek et al. 2014; Emmer 2017). Along with this process, the European Alps have also experienced the temperature increases two to three times greater than other ecosystems over the past several decades

(Auer et al. 2007; Ilyashuk et al. 2011). Additionally, other variables such as precipitation have also increased nonlinearly, with significant regional differences and seasonal shifts due to retreat of glacier extent, snow cover, and degradation of permafrost (Vavrus 2007; Stoffel et al. 2014). From these changes, the number of new lakes that develop upon unstable slopes has increased in Europe. Therefore, for timely monitoring and response to arising glacier hazards from these lakes and the surrounding environment, a rough estimation of lake areas and volumes is essential.

With improvements in the spatial resolution of satellite images, geomorphometry-related approaches, and the production of Digital Elevation Models (DEMs), modeling glacier beds and ice thickness estimation is possible for remote mountain environments (Huggel et al. 2003). The primary application of such detailed models is the projection of future ice-free mountain landscapes where the erosive power of former glacial landforms develops depressions susceptible to future lake development (Jawaid 2017).

Despite the high level of uncertainty in glacier thickness estimation, the resulting bed topography is in good agreement with historical maps of deglaciated areas (Linsbauer et al. 2012). Ice thickness estimation of glaciers has a long history of empirical relations between the surface slope and the base points. For example, Haeberli and Hoelzle (1995) applied a scalar approach to all glaciers in the Swiss Alps for glacier areas greater than 0.2 km<sup>2</sup>. A drawback of their methodology was that glaciers with the same size could have different ice thickness values. This shortcoming has been addressed with satellite improvements to glacial monitoring including the availability of digital terrain data, which provides topographic information for the detection of glacier outlines, elevation ranges, slope and ice thickness within the boundaries. From these advancements, the accuracy of

estimates using slope-dependent models increased compared to the area-dependent models applied in previous research (for technical details see (Frey et al. 2014)).

Slope-related models using DEMs and glacier boundaries for ice thickness estimation have been employed in previous studies (Müller et al. 1976, Masich and Heaberli, 1982, Maisch et al. 2000). Developing such approaches has become popular recently with the enhancement in both input data (e.g. high-resolution DEMs and satellites imagery), computer models, and machine learning techniques. For example, Clarke et al. (2009) applied an Artificial Neural Network to simulate glacier beds from the deglaciated areas in Canada. This method determines the ice-thickness for the subglacial topography based on the simulation of ice-free topography. The model resulted in a bed topography with a  $\pm 70\text{m}$  accuracy, which is promising for regional ice-volume estimation, despite significant errors in local ice thickness estimation.

Glacier ice thickness can also be measured by numerical glacier flow models using additional data from glacier mass balance and ice flow. Accordingly, ITEM (Ice Thickness Estimation Method) model uses the same approach to calculate the ice thickness of the Swiss glaciers (Farinotti et al. 2009a). Since this model requires physical parameters (e.g., surface accumulation, mass balance rate factors of ice flow and basal velocity), the model was further refined by Farinotti (2009b). The new model determines ice thickness based on the glacier mass balance rather than velocity observations, although such data is difficult to collect for large glaciers. The evaluation of the model with Ground Penetrating Radar (GPR) data revealed a high level of accuracy, however, it still requires a large amount of input data.

Presently, most models require manual delineation of glacier flowlines, which limits the regional application of such methods. Frey et al. (2014) applied a new version of GlabTop model in which ice thickness is calculated for randomly selected DEM cells. James et al. (2016) developed an automated approach in which flowlines are generated and the basal shear stress can be estimated for each glacier individually.

These models have been used in a few studies in Switzerland, Himalayas, and Peru for site detection of future glacier lake formation. Frey et al. (2010), developed a multi-level strategy for future lake formation and the runout distance in a worst-case scenario for the Swiss Alps using the bed-topography detection model by Linsbauer et al. (2009) and the Modified Single Flow (MSF) model developed by Huggel et al. (2003). A critical threshold of 2 degrees slope of debris-covered glaciers were defined as an indicator for future glacial lakes in the Himalaya (Fountain 2000). From a geomorphic perspective, Colonia et al. (2017) identified the spatial and temporal aspects of lake formation using the equilibrium concepts and numerical models.

This study employs the approach of James et al. (2016), which is more complex considering variations in side drag (Li et al., 2012) and can efficiently analyze the volume of multiple glaciers at a regional scale. To date, this approach has not been applied to the Swiss Alps. The estimation of total ice volume for the Swiss glaciers is scarce and based on the outlines of Swiss Glacier Inventory (SGI) of 1973 and 2000. Therefore, we use this model incorporating the most recent SGI and high-resolution DEM, and to compare the results with other methods in order to compare the automated model versus a manual extraction of glacier centerlines. Therefore, the objectives of this chapter are to: i) estimate mean glacier thickness for glaciers within the Rhone catchment, ii) create an ice-free DEM

of the glacier beds, iii) model and visualize glacier bed after glacier decline, iv) predict future lake sites, v) calculate the area and the volume of potential lakes, and vi) validate and compare the performance of Volume and Topography Automation (VOLTA), with the ITEM and Glacier Bed Topography (GlabTop) models.

## 4.2 Case study

We studied the two groups of glaciers, Bernese and Valais, within Rhone catchment (Fig 1-1). According to the Swiss Glacier Inventories (Fischer et al., 2014), the Rhone catchment has lost 152 km<sup>2</sup> of the glacierized area since 1973 with a mean geodetic mass balance change of -0.59 m w.e. yr<sup>-1</sup> from 1980 to 2010 (Fischer et al., 2015). Based on the recent inventory, there are 37 glacier bodies with areas larger than 3 km<sup>2</sup> that contribute to 69% of the total glacierized area but only 4.3% of the total number of glaciers in the Rhone catchment. Glaciers smaller than 1 km<sup>2</sup> comprise 90% of the total number of glaciers, however, they only cover 15% of the area.

Here, we calculated the ice thickness for 849 glaciers within Bernese and Valais Alps, however, for the detection of possible future lakes, only glaciers larger than 0.01 km<sup>2</sup> were considered. The elevation range of glaciers with an area between 1 km<sup>2</sup> and 5 km<sup>2</sup> ranges from 500 to 1300 m.a.s.l. ; glaciers with an area of 5 to 10 km<sup>2</sup> extend from 1104 to 1916 m.a.s.l.; glaciers within 10 to 15 km<sup>2</sup> total area occur within an elevation range of 1200 to 1950 m.a.s.l., and glaciers with areas greater than 15 km<sup>2</sup> are located between 2000 to 2500 m.a.s.l. (Fig 4-1). The latter class includes four glaciers, including Grosser Aletschgletscher, which is the largest with an area of 77.32 km<sup>2</sup>.

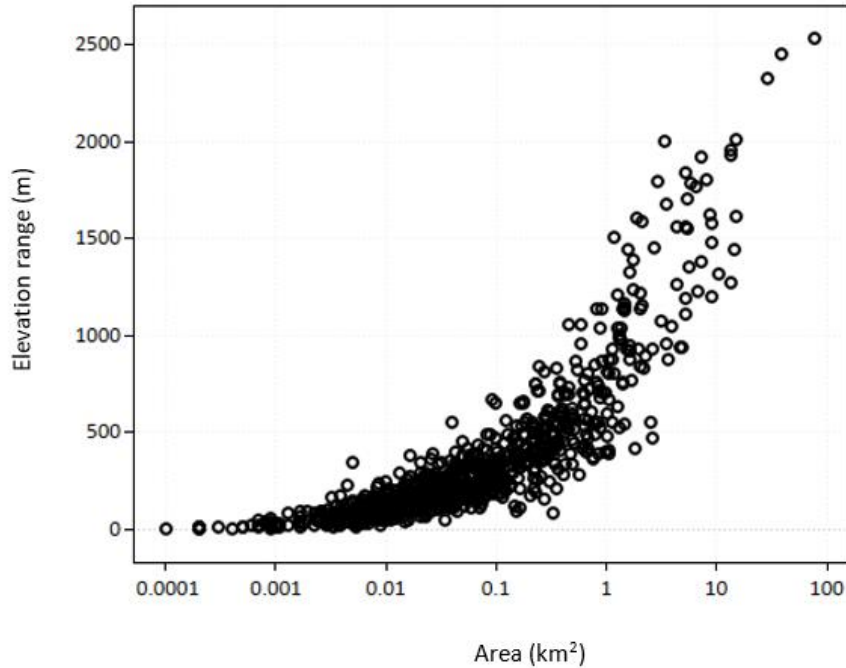


**Figure 4-1** Linear-log plot illustrating the relationship between the area of glaciers and the elevation bands within the Rhone catchment.

### 4.3 Data

We selected the Swiss Alps due to the quality and availability of data, which includes a high-resolution DEM, historical maps, and a long record of glacier inventories. The VOLTA model requires only two input data sets: 1) glacier outlines and 2) a DEM. With the rapid and accelerating glacier retreat observed in the European Alps during the last several decades, glacier outlines have been consistently updated.

Here, we used two different sources of glacier boundaries. The latest glacier inventory for the entire Swiss Alps (SGI2010) was derived by Fischer et al. 2014. The accuracy of the inventory was assessed by comparing the extents of clean, snow and/or debris-covered glaciers derived from multiple digitizations by several experts. The second

glacier outlines were extracted from SGI2000, which was created by Paul (2008) using Landsat Thematic Mapper (TM) corresponding to years 1998 and 1999.

Two versions of DEMs were obtained from the Swiss Federal Office of Topography (Swisstopo) and used in this study. The first DEM, Digital Height Model (DHM25) Level 2, was derived from the Swiss National Map 1:25,000 around 1995. The model corresponds best to the glacier outlines of 1992 and consists of digitized lakes, break lines, and spot heights available in an asymmetric 25-m grid. According to Swisstopo documents, the accuracy of the dataset was determined by comparison with surveyed ground control points and has a reported vertical accuracy of 1.5 m for flat areas and 3 m for the Alps.

The second, and more recent DEM is the swissALTI<sup>3D</sup> digital elevation model data set, which represents the surface of Switzerland w at a spatial resolution of 10 m (Swisstopo Online Shop 2019). Compared to the previous version, DHM25, swissALTI<sup>3D</sup> was derived by stereo correlation of 25 cm.

## 4.4 Methodology

### 4.4.1 Glacier ice thickness estimation and distribution

Linsbauer et al. (2012) developed a physically-based model that relates ice thickness to surface slope. The assumption is that the shear stress is constant along the central line of a glacier and the flow is parallel to the bed. Therefore, the ice thickness along this line was calculated using equation 1:

$$h = \frac{\tau_b}{f\rho g \sin\alpha} \quad 1)$$

where  $h$  is ice thickness (m);  $\tau_b$  is basal shear stress in Pa;  $f$  is the shape factor;  $\rho$  is the ice density equal to 900 kg/m<sup>3</sup>;  $g$  is gravitational acceleration (9.81 m/s<sup>2</sup>) and  $\alpha$  refers to

the surface slope along the centerline (degree). In this equation, basal shear stress was derived from:

$$\tau_b = 0.5 + 159.8\Delta H - 0.435\Delta H^2 \quad 2)$$

where  $\Delta H$  is the difference of altitude between the highest and lowest point of glacier in kilometers (Haeberli and Hoelzle 1995; Petrakov et al. 2016) (the result from this equation is in kPa which needs to be converted to Pa).

The shape factor refers to the ratio between the width of a glacier and its perimeter, which defines the friction of the glacier with the edge walls. Based on the empirical evidence of alpine glaciers, the values of 0.7 for glacier tongues and 0.9 for wide accumulation zones have been suggested by Masich and Haeberli (1982). The value of 0.8 is typical for valley glaciers while it can be smaller for other glacier types (Paterson, 1994).

On the other hand, the VOLTA model employs Li et al.'s (2012) model and uses a more physically realistic approach to calibrating  $f$  according to the local width of glaciers:

$$h = \frac{0.9 w \left( \frac{\tau_b}{\rho g \tan \alpha} \right)}{0.9 w - \left( \frac{\tau_b}{\rho g \tan \alpha} \right)} \quad 3)$$

where  $w$  is the half of glacier width at a specific point.

The model then interpolates the calculated ice thickness for basal points to the entire glacier using the ANUDEM algorithm designed by Hutchinson (1989). In this regard, the resulting ice thickness values for basal points are assumed as 'elevation points' and the glacier outlines as the contour lines where the ice thickness values are zero. ANUDEM has the advantage of simulating the concave shape of glacier beds (Linsbauer et al. 2009), which has been frequently referenced as an accepted interpolation method in previous works (Farinotti et al. 2009a; Li et al. 2012; Linsbauer et al. 2012, James et al. 2016).

To validate this model, the resulting volumes were compared with glacier volumes obtained from the Farinotti et al. (2009a) glacier list. We also compared the volumes of three glaciers common between the GlabTop model, presented by Linsbauer et al. (2012) as well as the ITEM, and VOLTA models. Since the values of glacier volume are published for the ITEM and GlabTop models and they were derived from the SGI2000 and DHM25, in which the glacier extent of 2000 corresponds well with the DEM from around 1995, we computed ice thickness and volume using VOLTA and the aforementioned two datasets as input data to make the three models comparable.

#### **4.4.2 Detecting potential future lakes in ArcGIS**

The resulting ice thickness distribution was subtracted from the DEM surface topography to delineate the glacier beds. Afterwards, a zonal statistics function was used to estimate mean and maximum ice thickness values and the total volume for each glacier body. This mean thickness is also used for a comparison with the values derived by the ITEM model (Farinotti et al., 2009a). From the obtained ice-free DEM, sinks in the bed were filled using the “fill” hydrology-tool in ArcGIS and the slopes of the glacier beds were extracted. The lakes were then identified by querying the bed slope with the condition of “< 1 degree”. The results were compared with the visual interpretation of Google Earth imagery, considering three morphological criteria of the glacier surfaces including i) slope increase over the glacier direction, ii) crevasses-free area followed by heavy crevasses formation, and iii) decrease in glacier width. According to Colonia et al. (2017) and Frey et al. (2010), the possibility of future lake sites was determined using the number of fulfilled criteria. The corresponding area and volume of the lakes over each glacier were

estimated from the difference between the filled bed and the initial bed topography DEMs, and maps and longitudinal profiles were compiled in ArcGIS.

## 4.5 Results

### 4.5.1 Ice thickness and glacier volume

The ice thickness and volume of glaciers located in the Rhone catchment were calculated twice; first, VOLTA applied on a 10m swissALTI<sup>3D</sup> DEM and the recent outlines from the Swiss glacier inventory, SGI2010, and the second run used the DHM25 DEM and the SGI2000 glacier outlines. In this section, we focus on the ice thickness distribution and volume of glaciers using VOLTA and volumes extracted from the glacier list provided in Farinotti et al. (2009a) produced using the ITEM approach. Figure 4-2a shows the ice thickness distribution for all glaciers located in Rhone catchment, in which ice thicknesses below 100m are dominant. As reported in Table 4-1, over 62% of the area (354 km<sup>2</sup>) is comprised of glaciers with ice thickness less than 50 m, and 16.6% (94.5 km<sup>2</sup>) falls within 50-100 m class. On the other hand, glaciers with ice thickness values between 100 m and 200 m occupy nearly 81 km<sup>2</sup>, and the glaciers with ice thickness greater than 200 m make up only 6.5% (37.3 km<sup>2</sup>) of the glacierized area.

From the total glacierized area, Aletsch covers 77.32 km<sup>2</sup> area, including 10.7% of the total volume of 28.6 km<sup>3</sup>. The average ice thickness for the Rhone catchment is approximately 68 m using outlines from 2010 and 70.48m for the outlines from 2000, which is equal to a decrease of 3.52% (Table 4-2).

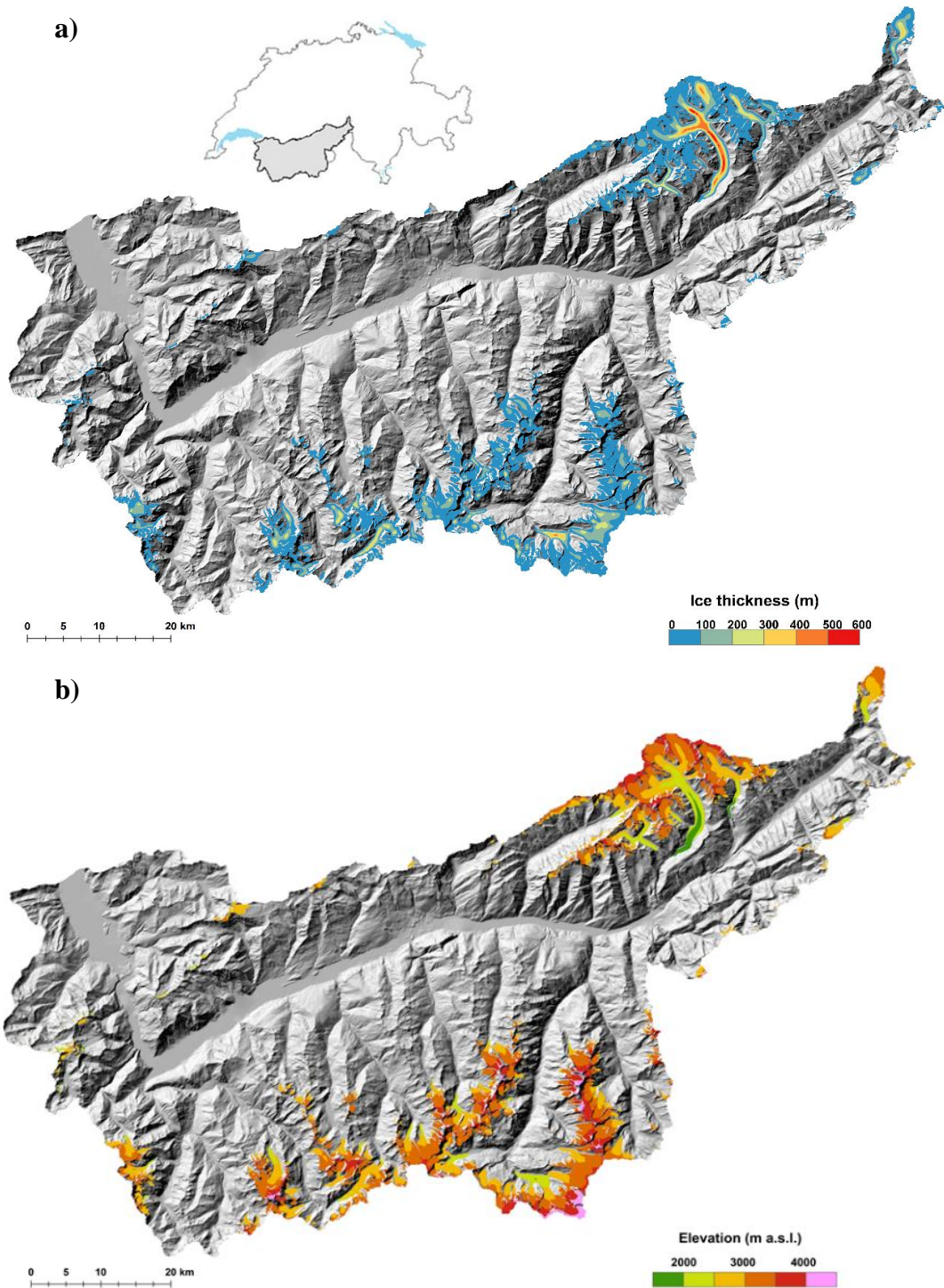


**Figure 4-2** Ice thickness distribution (a) and bed elevation (b) of glaciers using VOLTA model and SGI2010.

**Table 4-1** Ice thickness classes and the corresponding area and ice volume resulted from VOLTA model and SGI2010.

Ice thickness (m)	Area (km <sup>2</sup> )	%	Volume (km <sup>3</sup> )	%
0-50	354.20	62.20	7.69	20.70
50-100	94.50	16.60	6.80	18.20
100-200	81.30	14.30	11.32	30.40
>200	37.80	6.50	11.35	30.50
Total	577	100	37.16	100

**Table 4-2** Total area and volume of glaciers using different elevation models and outlines as input into the VOLTA model. The total volume of glaciers for the year of 2000 using ITEM is also included.

Inventory	DEM	Area (km <sup>2</sup> )	VOLTA		ITEM
			$h_{mean}(m)$	V(km <sup>3</sup> )	V(km <sup>3</sup> )
SGI2000	DHM25	393.54	70.48	32.70	44.95
SGI2010	swissALTI <sup>3D</sup>	346.95	68.00	28.63	-

Excluding the three largest glaciers (Aletsch, Gorner and Fiescher) the ice thickness values decrease to 64.8 m and 67.2 m, respectively. The comparison of mean and maximum ice thickness indicates that the maximum ice thickness for the glaciers in the Rhone catchment is four times more than the average mean ice thickness (referring to the linear regression  $y=3.95x$  with intercept of 0). The relationship between the average ice thickness and the glacier area visualized in a double logarithmic x-axis demonstrate a wide range of ice thicknesses produced by VOLTA model for glaciers exceeding an area of 1 km<sup>2</sup>.

We also calculated the ice thickness and volume of glacierized areas using different input data. VOLTA estimated the total ice volume of 32 km<sup>3</sup> and average ice thickness of 70 m for the total glacierized area of 393 km<sup>2</sup> (Table 4-2).

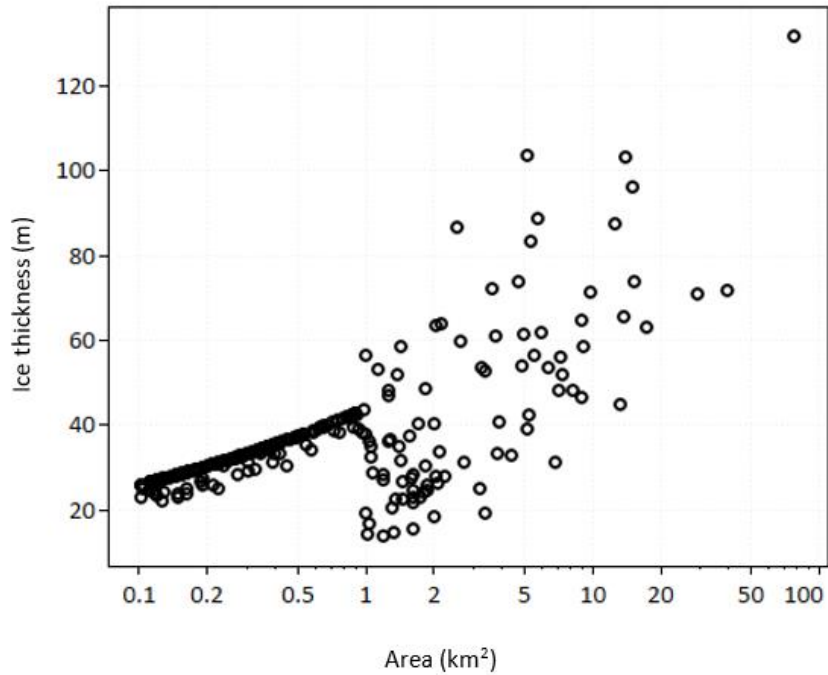


**Figure 4-3** Linear-log plot showing the relation between average ice thickness and area of glaciers.

The corresponding values declined to 28 km<sup>3</sup> and 68 m, respectively, for the total area of 346 km<sup>2</sup> within a decade time-period. Comparing the total volume of glaciers with ITEM model outputs for the glacier inventory of 2000, suggests a good agreement with a total  $\pm 12.84$  km<sup>3</sup> difference (Table 4-3).

#### 4.5.2 Glacier bed topography

The ice-free topography for the glaciers modeled using the VOLTA algorithm, and a 10m DEM is provided in Figure 4-2b. According to glacier bed elevation and the central flowline profiles of four large glaciers in Rhone catchment (Fig 4-4), the largest ice thicknesses and volumes are associated with the low and flat areas, and tongues; and the thinner ice thicknesses are located on steep slopes.

The modelled tongue of these glaciers shows an elevation range from 1700 m a.s.l. (Aletsch and Fiescher) to just below 2500 m a. s.l. (Gorner and Corbassière).

Regarding the ice thickness distribution of these glaciers, Fiescher reveals a different pattern possessing a thin tongue, which is due to a steep terminus area and flat accumulation area. For the other glaciers, ice thickness is low in higher elevations within the accumulation area and increases over the terminus area in the ablation zone (Fig 4-4).

**Table 4-3** The glacier parameters including area (km<sup>2</sup>), elevation range ( $\Delta H$  (m)), mean slope ( $\alpha$  (°)), for glaciers > 5 km<sup>2</sup> located in Rhone catchment, and comparison of the individual glacier mean ice thickness ( $h_{mean}$  (m)), maximum ice thickness ( $h_{max}$  (m)) using VOLTA model with ITEM for SGI2000 outlines.

Glacier Name	Area <sub>2000</sub> (km <sup>2</sup> )	$\Delta H$ (m)	$\alpha$ (°)	Aspect	$h_{mean}$	$h_{max}$	Volume (km <sup>3</sup> )	
							VOLTA	ITEM
Grosser Aletschgletscher*	82.15	2477	14.60	SE	132.93	584.13	10.92	15.36 ± 4.52
Gornergletscher*	55.80	2373	20.46	NW	71.85	468.3	3.97	6.14 ± 1.97
Oberaletschgletscher	19.28	1622	23.9	S	58	276.3	1.11	2.05 ± 0.56
Fieschergletscher VS	31.30	2272	20.00	SE	77.4	403.7	2.35	3.70 ± 0.97
Corbassière Glacier de*	16.70	2012	19.40	NW	79.88	290.7	1.32	1.48 ± 0.66
Rhonegletscher*	15.76	1405	15.19	SW	104.41	370.55	1.60	2.23 ± 0.41
Zmuttgletscher	15.32	1893	19.86	NE	69.4	272	1.06	1.52 ± 0.40
Findelengletscher	14.30	1277	13.72	NW	113.12	333.5	1.61	1.84 ± 0.48
Zinal Glacier de*	14.02	1960	24.00	NE	50.2	219.9	0.70	1.00± 0.24
Otemma Glacier d'	11.60	1291	15.30	NW	89.79	345.17	1.03	1.37± 0.36
Allalengletscher	9.27	1455	18.89	NE	50.24	260.58	0.46	0.90± 0.23
Ferpèche Glacier de	9.17	1500	17.38	NW	64.81	234.8	0.59	0.94± 0.24
Mont Miné Glacier du	8.98	1688	15.90	W	73.61	241.27	0.65	0.86 ± 0.22
Oberer Theodulgletscher	6.70	876	16.57	NW	77.76	287.22	0.52	0.46 ± 0.12
Langgletscher	9.36	1804	21.64	S	51.96	214.47	0.48	0.61± 0.16
Feegletscher	15.50	2018	24.17	NE	38.11	199.38	0.80	0.84 ± 0.22
Riedgletscher	7.60	2134	21.39	NW	61.4	200.39	0.46	0.43± 0.11
Brenay Glacier du	7.23	1224	19.93	S	48.37	257.16	0.34	0.59± 0.15
Saleina Glacier de	6.90	2021	23.25	NE	56.24	209.93	0.38	0.41 ± 0.11
Mont Durand Glacier du	5.94	1816	20.34	E	72.06	224.67	0.49	0.45 ± 0.12
Trient Glacier du	5.99	1446	17.74	NW	79.64	232.20	0.47	0.43 ± 0.10
Mittelaletschgletscher	7.42	1661	26.84	E	29.44	200.63	0.21	0.45± 0.12
Bruneggletscher	5.70	1473	18.21	NW	66.03	219.42	0.37	-
Moming Glacier de	6.13	1733	27.18	NW	41.67	175.67	0.25	0.39 ± 0.10
Giétro Glacier du*	5.42	1262	14.50	NW	103.75	270.29	0.56	0.50 ± 0.09

\*Glaciers with direct ice thickness measurements from radio-echo sounding for estimating uncertainty of ITEM (Farinotti et al. 2009a).

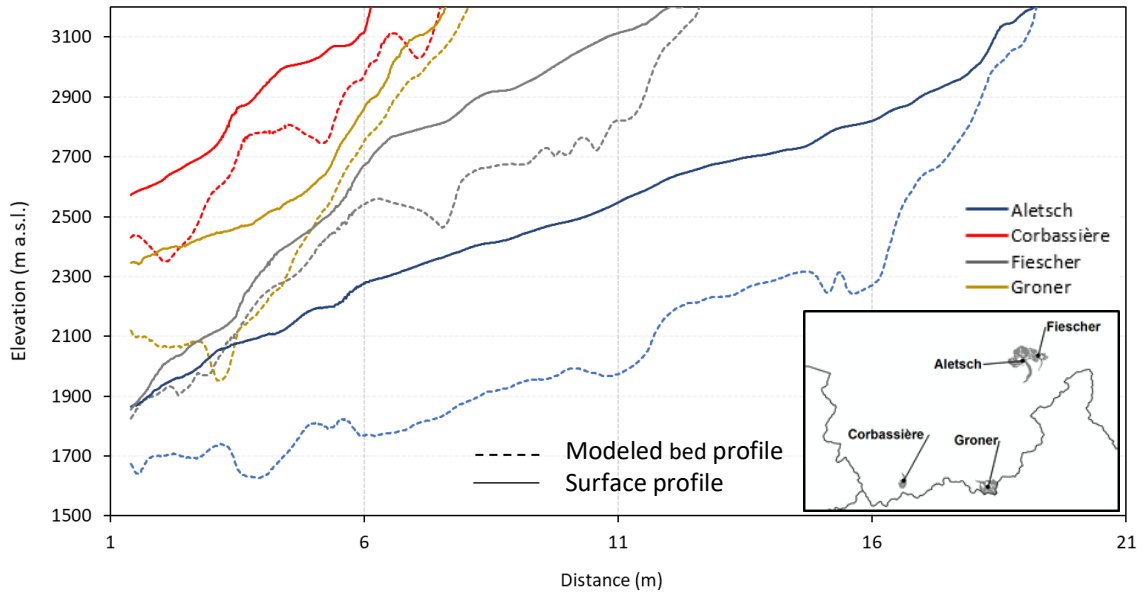


**Figure 4-4** Profile of modelled beds (dashed line) and surfaces (solid line) of four large glaciers in Rhone catchment for the outlines of SGI2010. The inset map shows the location of these glaciers.

The hypsometry of area mean ice thickness and volume of glaciers is represented in Figure 4-5 for the year 2010. Although the highest mean ice thicknesses are associated with the elevation band of 1500 to 2000 m a.s.l., the volume and the area of glaciers show a normal distribution over 3000 m a.s.l. Such differences between ice thickness, area, and volume can be due to the convergence of several tributaries creating a flat area with higher ice thickness values in large glaciers (i.e., Aletsch), or due to the presence of large depressions within the terminus zones of the glaciers. On the other hand, volume distribution and surface area follow the same pattern over the elevation bands; however, the volume slightly shifts upward within the elevation range of 1500 to 2500 m a.s.l. where the glacier areas approach to zero.

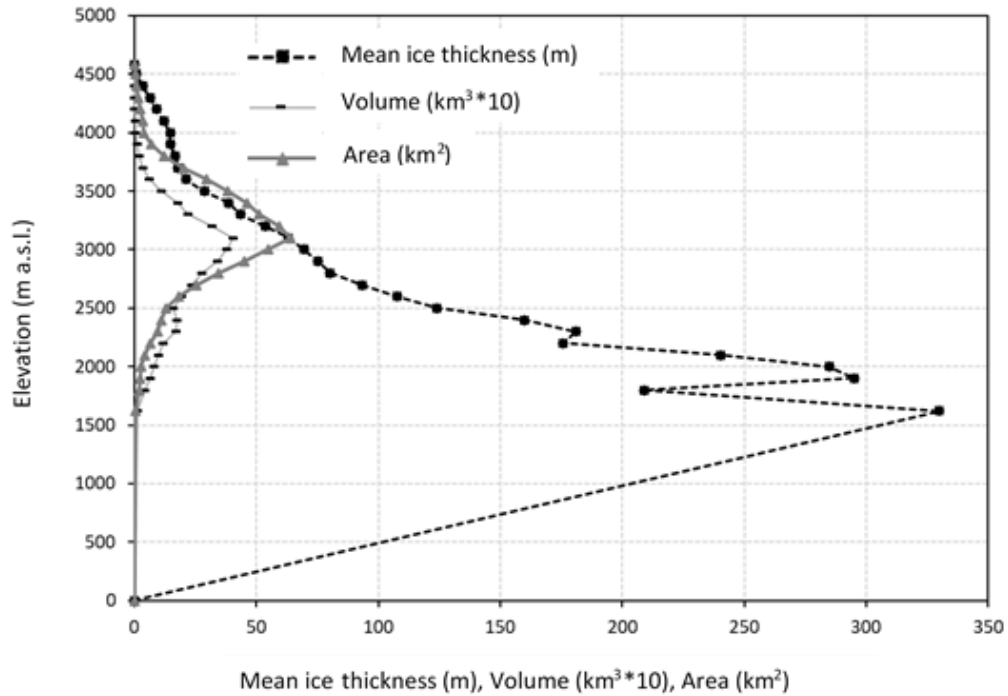


**Figure 4-5** The hypsometric curves of glacier mean ice thickness, area and volume for SGI 2010.

### 4.5.3 Location of future lakes

The depressions over the glacier bed were detected (Fig 4-8a&b) and the possibility of future lakes was determined (Table 4-4) (Frey et al. 2010; Colonia et al. 2017) based on the methods described in section 4.4.2. Figure 4-6 depicts the modelled overdeepenings over Mont Miné Glacier considering the three associated morphological criteria (overdeepenings, slope, and glacier width) to determine the potential future lake sites.

The application of these three morphological criteria on topographic maps, show that lakes are likely to form where all three criteria are present with a probability of 75% (Haerberli et al. 2016).

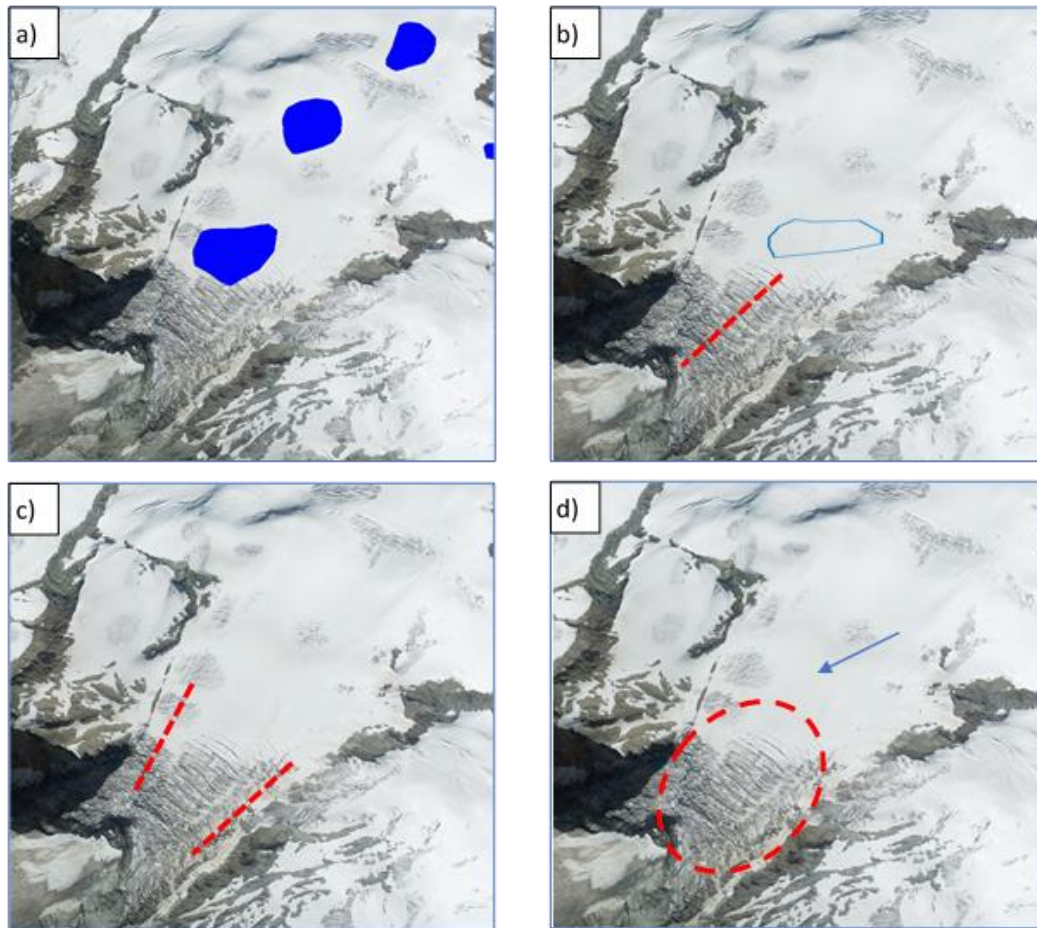


**Figure 4-6** Morphological criteria that determines the possibility of sites for future lakes: a) the modelled overdeppenings over Mont Miné Glacier in Valais Alps using VOLTA and SGI2010, b) slope increase over the glacier direction, c) decrease in glacier width, and d) crevasses-free area followed by heavy crevasses formation (Frey et al. 2010; Colonia et al. 2017).

**Table 4-4** Modelled future lakes and their corresponding possibility based on the morphological criteria. The total area, volume and mean of depth for each possibility class is also calculated.

No. Criteria	Possibility	No. potential lakes	Area (km <sup>2</sup> )	Volume(km <sup>3</sup> )	depth <sub>mean</sub> (m)
1	Low	55	5.76	1.17	19.08
2	Medium	18	3.19	0.83	23.36
3	High	81	11.84	2.39	22.06

Accordingly, we delineated a total of 154 potential sites with an area greater than 0.01 km<sup>2</sup>, in which 81 of these sites indicated a high potential to be the location of lakes in future. The total volume of the class with the high potential formation is 2.39 km<sup>3</sup> and average depth of 22 m.

The largest overdeepening in the Rhone catchment with an area of 1.46 km<sup>2</sup> is located in the terminus area of Gorner glacier. This depression is partially covered by debris deposits and the calving processes have been initiated within the end of the tongue (Figure 4-7). The corresponding total volume of the site is approximately 0.43 km<sup>3</sup> with a mean depth of 290 m and max depth of 500 m. The second largest overdeepening is situated in Aletsch tongue in Bernese Alps. It has an area of 1.2 km<sup>2</sup>, mean depth of 288 m, max depth of 477 m, and total volume of 0.36 km<sup>3</sup>.



**Figure 4-7** Gorner glacier tongue, where the ice calving process has been initiated at the end (Source: Google Earth Imagery, 09/29/2016).

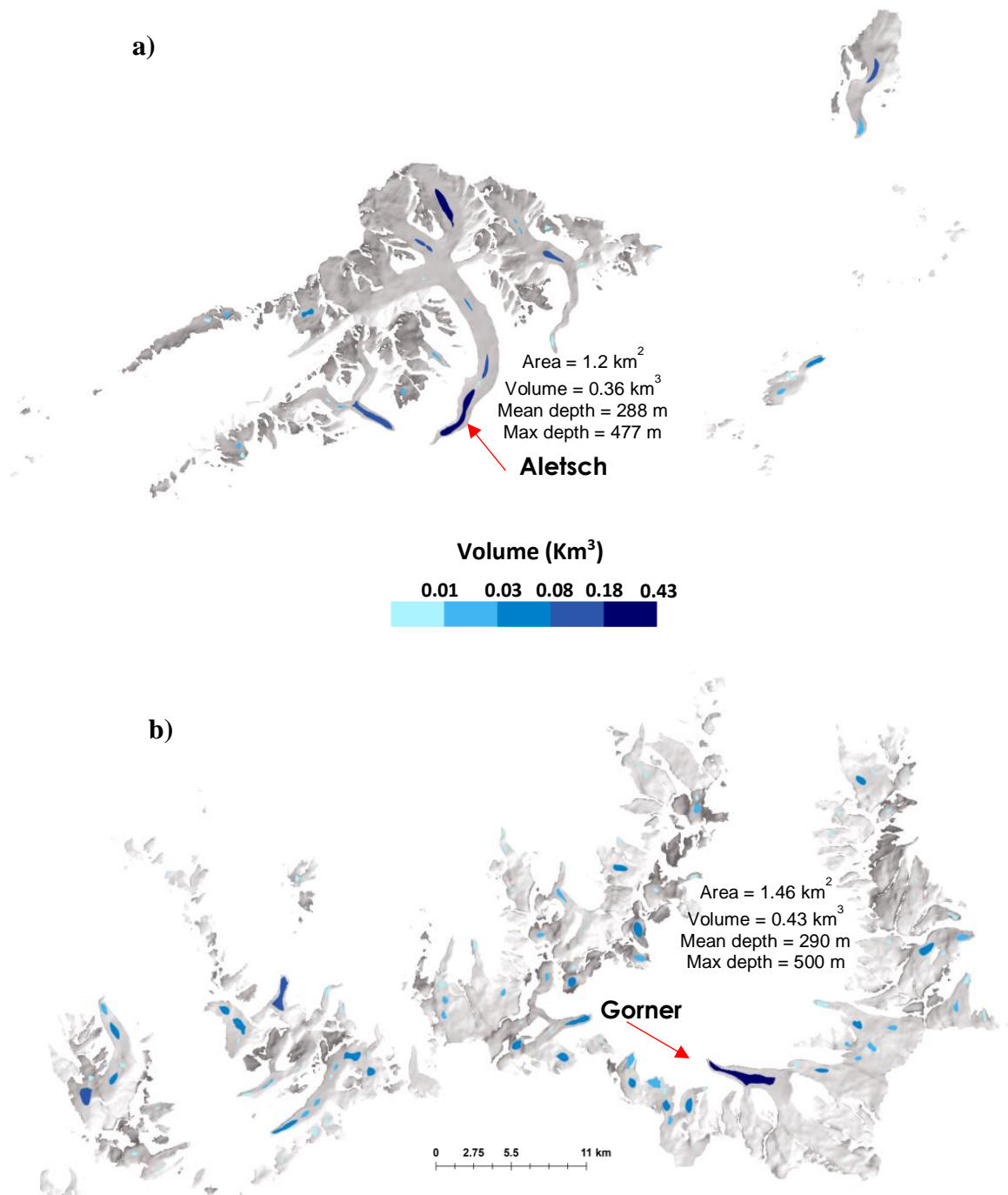


**Figure 4-8** The spatial distribution of overdeepenings with the corresponding total volumes: a) Bernese Alps, b) Valais Alps.

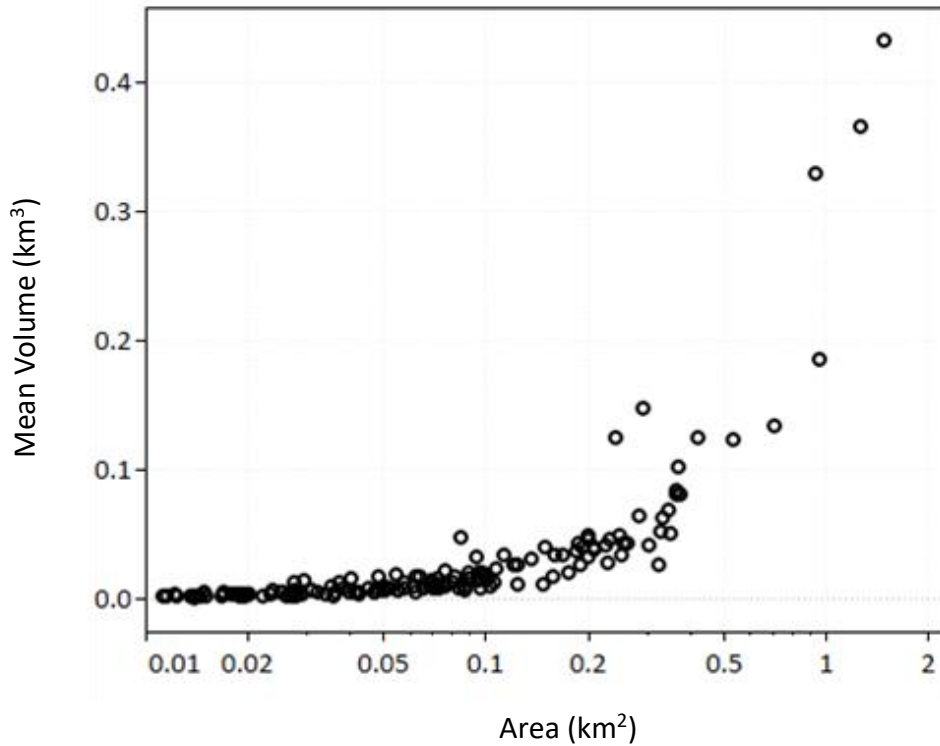


**Figure 4-9** The linear-log plot showing the distribution of mean volume of potential lakes against the corresponding areas for SGI2010.

About 93% (144 out of 154) of these overdeepenings have a volume of less than 0.1 km<sup>3</sup>, only three overdeepenings hold a volume of greater than 0.3 km<sup>3</sup> (Figure 4-9). The estimated total volume of overdeepenings in Rhone catchment is about 4 km<sup>3</sup>, about 11% of the total ice volume in the Rhone catchment, using estimates from the VOLTA model and SGI2010.

## 4.6 Discussion

### 4.6.1 Model performance of ice thickness and total volume

The performance of the VOLTA model corresponding to SGI2000 and HDM25 for individual glaciers is compared with output from the ITEM model in Table 4-3. Glaciers with available field measurements (i.e., radio-echo sounding) are indicated. The

uncertainty of ITEM ice volume for individual glaciers is estimated from the ice thickness distribution which is expressed as  $\sigma_h / h$ , where  $\sigma_h$  is the standard deviation of ice thickness  $h$  and accuracy of glacier outlines,  $\sigma_A / A$  (Farinotti et al., 2009a).

**Table 4-5** Mean ice thickness (m) for three glaciers using SGI2000 and three different models.

Glacier	VOLTA	GlabTop (idw/ttr)	ITEM
Zinal	50.20	58/61	66
Rhone	104.41	101/105	132
Corbassière	79.88	91/96	93

The results show that VOLTA has underestimated the glacier volumes compared to ITEM, and it is specifically higher for glaciers with larger area and greater mean ice thickness. However, VOLTA results fall within the range of 95% confidence intervals calculated for ITEM model using radio-echo sounding profiles. The total volume of the two models is also presented in Table 4-2.

According to James et al. (2016), the comparison of ice volume returned by VOLTA with GPR field measurements shows a range of 25% underestimation and 16.6% overestimation. Considering the ice thickness distribution, VOLTA is also in good agreement with field measured profiles and the variations are largely matched, especially where the glacier cross-sections are V-shaped. Although VOLTA can estimate maximum ice thickness close to field measured profiles for U-shaped valleys, the V-shaped profiles created by ANUDEM algorithm underestimate the ice thickness towards the valley walls (James et al. 2016) and consequently result in underestimation of total ice volume for these glaciers. This corresponds to the underestimation of VOLTA compared to the other two models, ITEM and GlabTop (IDW and TopoToRaster interpolation methods) (Table 4-5).

For Corbassière Glacier, the derived value by VOLTA is 16 m smaller with GlabTop which is due to U-shape of valley in most part of the glacier.

#### **4.6.2 Glacier bed topography and future lakes**

The resulting bed topography is highly dependent on the accuracy of the DEM used in the model. In general, the higher quality data and DEM resolution allow for accurate calculation of surface slope, which can capture the robust location of overdeepenings. The sensitivity test of VOLTA shows higher sensitivity of ice thickness and volume to slope degree, which means the increases of slope causes a reduction in point ice thickness estimations and the interpolation of ice thickness approaches to zero values, mainly for the smaller glaciers (Figure 4-3) (James et al., 2016). Overall, small glaciers with extreme slope values, whether low or high, are highly sensitive to the VOLTA input data.

Frey and Paul (2012) also confirm that a coarser DEM resolution decreases maximum and increases minimum elevation since these two parameters depend on individual cell values which are strongly influenced by the resolution of DEM. In addition, the authors recommend that the acquisition date of the DEM should not be older than the acquisition date of the glacier outlines, especially for the glaciers that are retreating rapidly. Therefore, the present uncertainty in our results can be referred to the uncertainty of the glacier outlines and the time of DEM acquisition, especially for SGI2000 and DHM25.

The location of future lakes appears to be controlled by the location of stagnant ice development during the glacier retreat. According to Small (1995), the hypsometry of valley plays an important role in developing the stagnant ice deposits where the valley margins are retreating quickly. Valley hypsometry and the rate of retreat are determined by the slope and width along the valley centerline. This means stagnation develops where

concave-up form of valley reaches a region of shallow bed slope, whereas steep slopes advance active retreat (Small 1995, Vacco et al., 2010). Another controlling factor in formation of future lakes is the presence of thick debris over the glacier surface, which reduces the rate of ablation and allows a glacier to reach below the ELA, compared to a clean glacier. Therefore, it can be inferred that clean glaciers located on rougher basal beds with lower mean slopes are susceptible to stagnate and create a favorable condition for future lakes as a result of faster reaction to global warming. However, the delineated overdeepenings located in glacier tongues covered by thick debris may transform into outwash plains or the shallow lakes/depressions filled with debris from the surrounding margin valleys (Linsbauer et al., 2016).

#### **4.7 Conclusions**

This study examined the VOLTA model for delineation of bed topography from the estimation of ice thickness using a high-resolution DEM and the most recent Swiss glacier outline. The purpose of this analysis was to find the potential sites for future lake development. This model can be an alternative to models that uses mass balance measurements (Farinotti et al., 2009a; Michel et al., 2013), surface velocity (McNabb et al., 2012), and the models that require manual extraction of centerlines (Linsbauer et al., 2012). The important findings of this chapter derived from the results are listed below:

- The average ice thickness of Rhone catchment is approximately 68m using glacier outlines of 2010 and 70.48m for the glacier outlines of 2000.
- The maximum ice thickness for the glaciers in Rhone catchment is four times more than average mean ice thickness.

- VOLTA estimated total ice volume at 32 km<sup>3</sup> and an average ice thickness of 70 m for the total glacierized area spanning 393 km<sup>2</sup>; there is good agreement between this model and the total volume of glaciers with ITEM model for the glacier inventory of 2000 with a total ±12.84 km<sup>3</sup> difference. However, the sensitivity of volume to the glacier area from different inventories and input DEM (time difference) should be taken into account when comparing the total difference of VOLTA model.
- The largest mean ice thicknesses are associated with the elevation band of 1500 to 2000 m a.s.l.
- A total 154 potential sites were delineated with an area greater than 0.01 km<sup>2</sup>, in which 81 of these sites are classified as locations that are highly likely to form proglacial lakes in future. The total volume of the class with the high potential for formation is 2.39 km<sup>3</sup> and average depth of 22 m.
- The largest overdeepening in Rhone catchment is located in the terminus area of Gorner glacier and has an area of 1.46 km<sup>2</sup>.
- Although VOLTA can estimate maximum ice thickness close to field measured profiles for U-shaped valleys, the V-shaped profiles created by the ANUDEM algorithm underestimate the ice thickness towards the valley walls.
- The accuracy of VOLTA is highly dependent on the shape of valley, therefore, the overall error in ice thickness and volume is not completely related to the model robustness but also varies from one glacier to another.
- Compared to GlabTop model, VOLTA uses an enhanced centerline generation algorithm by including a side drag parameter in the equation, which reduces the

uncertainty from 30% to 26.5% (underestimation) and 16.6% (overestimation) (James et al. 2016).

- Future research should focus on developing algorithms that simulate the shape of valleys accurately, in order to avoid the underestimation of ice thickness adjacent to steep valley sides.

## 5 SUMMARY & LIMITATIONS

### 5.1 Chapter 2

Glacier mass variations are climatic indicators since they represent the amount of received solid precipitation in winter and melt energy in summer. Therefore, it is essential to examine long-term winter and summer mass balance values to address the climate fluctuations. Huss et al. (2015) re-evaluated 19 series of glacier-wide seasonal mass balance for the Swiss Alps based on point observations. This dataset, extending back to 1980s with the seasonal dimension, can therefore be analyzed and glaciological changes can be compared to recent climate variability and change. Using the Huss dataset, we studied the interactions between local meteorological variables and distant large-scale atmospheric and oceanic patterns and glacier mass balance components.

The results show that all selected glaciers have lost their equilibrium condition in the recent decades with the persistent negative annual mass balance trends, and decreasing accumulation area ratios (AARs), accompanied by increasing air temperatures by  $+0.45^{\circ}\text{C decade}^{-1}$ . It is also evident that while the annual balance of larger glaciers, like Aletsch, have fluctuated their mass variations are small and remain close to the equilibrium line in comparison with other glaciers. Most of the observed glaciers are losing accumulation area given that the AAR percent has dropped from approximately 75% in 1970 to 25% in recent years, stressing the rate of melt acceleration. The controlling factor of annual mass balance is mainly attributed to summer mass losses, which are anticorrelated with (warming) June to September air temperatures.

In addition, the interannual variability of summer and winter mass balances is inversely associated to the Atlantic Multidecadal Oscillation (AMO), Greenland Blocking

Index (GBI) and East Atlantic (EA) teleconnections. Forecasting results out to 2030 suggest that the smaller glaciers will continue to melt faster because of their inability to adjust to warming climate conditions as well as increases in longwave heat input from the bare slopes.

Based on the current research, the negative mass balance trends cannot be simply attributed to the direct response of global warming. Hence, we emphasize that future investigations should focus on resolving complex and indirect surface-atmosphere interactions (e.g. reflectivity and impurities of glacier surfaces) to more comprehensively understand physical processes driving glacier mass balance variability and change.

## **5.2 Chapter 3**

This chapter investigated the capability of the Landsat 8 Operational Land Imager (OLI) and Thermal Infrared Sensor (TIRS) for mapping glacier facies and debris-covered surfaces in the Rhone catchment. The spectral profiles and histograms of different bands along a selected glacier profile, the western arm of Oberaletsch Glacier, were examined to determine the bands that provided optimal contrast. The reflectance characteristics of visible and Near Infrared (NIR) of OLI bands for glacier facies showed a distinctive contrast with those in Short-wave Infrared (SWIR) bands. According to the different thermal regime of glacier surfaces, the obtained ‘at-satellite brightness temperature’ from TIRS used as a base layer class range detection. The surfaces in glacier boundaries were then generated by thresholding the enhanced image and were validated using Google Earth imagery dataset. We were able to distinguish four glacier facies including snow, clean ice, slush/crevasses, and mixed ice.

The applied method captured the debris-covered areas accurately, however, several misclassifications for the 'snow' class into 'dirt ice' or 'slush/crevasses' in areas where bedrock outcrops of valley walls were present in shade or/and in higher altitudes, were detected. Furthermore, the shadows on the original image were considered as another source of error in the classification process. The current method could not also separate the slush zone and crevasses; therefore, they were categorized into one class. Due to the presence of such limitations, future research should focus on optimization of this approach by including surface slope of glaciers, contour lines and the 0°C surface temperature line in the classification process.

### **5.3 Chapter 4**

Understanding the bed topography of glaciers is essential for understanding lake formation, the impacts of climate change, and the erosive power of glacier activity in the past. This study aims to predict potential sites for future lake formation with the combination of most recent glacier outlines and a high-quality digital elevation model. Unlike ice thickness models presented in the past, Volume and Topography Automation (VOLTA) calculates the distribution of ice thickness based on automatically-derived glacier flowlines and includes a valley side drag parameter in the force equation. Here, we used VOLTA in the Swiss Alps and estimated the present total ice volume of 32 km<sup>3</sup> and average ice thickness of 70 m for the total glacierized area of 393 km<sup>2</sup>. Comparison of the total volume of glaciers with the Ice Thickness Estimation Method (ITEM) for the glacier inventory of 2000, indicates good agreement with a total ±12.84 km<sup>3</sup> uncertainty.

Using VOLTA to analyze bed topography of glaciers, 154 potential lake sites with an area greater than 0.01 km<sup>2</sup> were detected. Considering three-morphological criteria, 81 of these sites were identified as highly possible locations of future lakes, with a total volume of 2.39 km<sup>3</sup> and average depth of 22 m.

These results highlight the importance of combined datasets and parameters for projecting the future glacier landscapes and providing planners with essential knowledge for water resource and hazard management in these areas. Future research should focus on developing algorithms that simulate the shape of valleys the way that underestimation of ice thickness adjacent to steep valley sides are minimized.

#### **5.4 Implications for hazard and risk management and future research**

The principals of multi-hazard and risk management was outlined in the beginning of this dissertation (Chapter 1). The previous chapters were concerned with the factors influencing glacier mass imbalance, consequent glacier surface changes connected to the future lakes that are potential to develop into future process chain of lake-outburst flows threatening the downstream settlements in high-mountain regions of Switzerland.

Disregarding the equivalent water preserved in glaciers, the information on topography of glacier surface and future ice-free bed was necessary for locating the future lakes. Here, we predicted and constructed changes on surface topography and characteristics of glaciers linked to ongoing climate change, which are presently needed for discovering the hotspots and prioritizing future multi-hazard and risk management in cold regions.

A solid understanding of dynamic evolution of the lakes and the interplay role between climate change impacts on glaciers and glacial lake formation at spatio-temporal scales that addressed here, would assist the scientists and planners through the challenging task of future physical hazards and future damages integration. Further, thanks to difficulties regarding the access to freezing rugged remote alpine environments, remote sensing techniques, which is an urgent need in future multi-hazard studies for monitoring glacier dynamics and designation of early warning systems, especially in densely populated valleys of Switzerland, were demonstrated and discussed in this dissertation as well.

Following to this study, future research should focus on the dynamics of supraglacial lakes and lake expansion linked to the findings from Chapter 2 due to the impacts of the glacial lakes and glacier surfaces have on ablation acceleration through ice cliff calving. Also, the conversion of glacial lake types by glacier decline, e.g. from supraglacial lakes to moraine/ice-core-dammed lakes, needs to be taken into account for studying future hazard and risk evolution of GLOFs in high-mountain regions around the world.

## REFERENCES

- Abermann, J., A. Lambrecht, A. Fischer, and M. Kuhn. 2009. Quantifying changes and trends in glacier area and volume in the Austrian Ötztal Alps (1969-1997-2006). *The Cryosphere* 3 (2):205–215.
- Alcántara-Ayala, I., and A. S. Goudie eds. 2010. *Geomorphological Hazards and Disaster Prevention*. Cambridge: Cambridge University Press.
- Alifu, H., R. Tateishi, and B. Johnson. 2015. A new band ratio technique for mapping debris-covered glaciers using Landsat imagery and a digital elevation model. *International Journal of Remote Sensing* 36 (8):2063–2075.
- Anaconda, P. I., A. Mackintosh, and K. Norton. 2015. Reconstruction of a glacial lake outburst flood (GLOF) in the Engaño Valley, Chilean Patagonia: Lessons for GLOF risk management. *Science of The Total Environment* 527–528:1–11.
- Andrews, D.W.K., and W. Ploberger. 1994. Optimal Tests when a Nuisance Parameter is Present Only Under the Alternative. *Econometrica* 62 (6):1383–1414.
- Auer, I., R. Böhm, A. Jurkovic, W. Lipa, A. Orlik, R. Potzmann, W. Schöner, M. Ungersböck, C. Matulla, K. Briffa, P. Jones, D. Efthymiadis, M. Brunetti, T. Nanni, M. Maugeri, L. Mercalli, O. Mestre, J.-M. Moisselin, M. Begert, G. Müller-Westermeier, V. Kveton, O. Bochnicek, P. Stastny, M. Lapin, S. Szalai, T. Szentimrey, T. Cegnar, M. Dolinar, M. Gajic-Capka, K. Zaninovic, Z. Majstorovic, and E. Nieplova. 2007. HISTALP—historical instrumental climatological surface time series of the Greater Alpine Region. *International Journal of Climatology* 27 (1):17–46.
- Bai, J. 1997. Estimation of A Change Point In Multiple Regression Models. *The Review of Economics and Statistics* 79 (4):551–563.
- Bai, J., and P. Perron. 2003. Computation and analysis of multiple structural change models. *Journal of Applied Econometrics* 18 (1):1–22.
- Banerjee, A. 2017. Brief communication: Thinning of debris-covered and debris-free glaciers in a warming climate. *The Cryosphere* 11 (1):133–138.
- Barnston, A. G., and R. E. Livezey. 1987. Classification, Seasonality and Persistence of Low-Frequency Atmospheric Circulation Patterns. *Monthly Weather Review* 115 (6):1083–1126.
- Beniston, M. 1997. Variations of snow depth and duration in the swiss alps over the last 50 years: Links to changes in large-scale climatic forcings. *Climatic Change* 36 (3/4):281–300.
- . 2005. Mountain Climates and Climatic Change: An Overview of Processes Focusing on the European Alps. *Pure and Applied Geophysics* 162 (8–9):1587–1606.

- Benson, C. S., and R. J. Motyka. 1979. Glacier-volcano interactions on Mt. Wrangell, Alaska: University of Alaska Geophysical Institute Annual Report 1977-78, p. 1-25.
- Bhardwaj, A., P. Joshi, Snehmani, L. Sam, M. K. Singh, S. Singh, and R. Kumar. 2015. Applicability of Landsat 8 data for characterizing glacier facies and supraglacial debris. *International Journal of Applied Earth Observation and Geoinformation* 38:51–64.
- Bishop, M. P., J. F. Shroder, and B. L. Hickman. 1999. SPOT Panchromatic Imagery and Neural Networks for Information Extraction in a Complex Mountain Environment. *Geocarto International* 14 (2):19–28.
- Bischof, N., H. Romang, and M. Bründl. 2009. Integral risk management of natural hazards - A system analysis of operational application to rapid mass movements. In *Safety, Reliability and Risk Analysis: Theory, Methods and Applications*, 2789–2795.
- Bolch, T., and U. Kamp. 2005. *Glacier mapping in high mountains using DEMs, Landsat and ASTER data*. In: 8<sup>th</sup> International Symposium on High Mountain Remote Sensing Cartography, La Paz (Bolivien), 20 March 2005 - 27 March 2005, 37-48.
- Braithwaite, R. J., and Y. Zhang. 2000. Sensitivity of mass balance of five Swiss glaciers to temperature changes assessed by tuning a degree-day model. *Journal of Glaciology* 46 (152):7–14.
- Braithwaite, R. J. 2002. Glacier mass balance: the first 50 years of international monitoring. *Progress in Physical Geography: Earth and Environment* 26 (1):76–95.
- Brown, R. L., J. Durbin, and J. M. Evans. 1975. Techniques for Testing the Constancy of Regression Relationships over Time. *Journal of the Royal Statistical Society. Series B (Methodological)* 37 (2):149–192.
- Bründl, M., H. E. Romang, N. Bischof, and C. M. Rheinberger. 2009. The risk concept and its application in natural hazard risk management in Switzerland. *Natural Hazards and Earth System Sciences* 9 (3):801–813.
- Brunsdon, D. 2001. A critical assessment of the sensitivity concept in geomorphology. *CATENA* 42 (2–4):99–123.
- Butler, D. R. 1989. Glacial Hazards in Glacier National Park, MONTANA. *Physical Geography* 10 (1):53–71.
- Cantonal Office of Statistics and Equalization - <https://www.vs.ch/web/acf/statistique> (last accessed 17 November 2019).
- Carey, M. 2010. *In the shadow of melting glaciers: climate change and Andean society*. New York: Oxford University Press.

- Carturan, L., R. Filippi, R. Seppi, P. Gabrielli, C. Notarnicola, L. Bertoldi, F. Paul, P. Rastner, F. Cazorzi, R. Dinale, and G. Dalla Fontana. 2013. Area and volume loss of the glaciers in the Ortles-Cevedale group (Eastern Italian Alps): controls and imbalance of the remaining glaciers. *The Cryosphere* 7 (5):1339–1359.
- Carturan, L., C. Baroni, M. Brunetti, A. Carton, G. Dalla Fontana, M. C. Salvatore, T. Zanoner, and G. Zuecco. 2016. Analysis of the mass balance time series of glaciers in the Italian Alps. *The Cryosphere* 10 (2):695–712.
- Chevallier, P., B. Pouyaud, W. Suarez, and T. Condom. 2011. Climate change threats to environment in the tropical Andes: glaciers and water resources. *Regional Environmental Change* 11 (S1):179–187.
- Chorley, R. J. 1973. *Directions in Geography*. Methuen [Distributed by Barnes & Noble, New York].
- Chow, G. C. 1960. Tests of Equality Between Sets of Coefficients in Two Linear Regressions. *Econometrica* 28 (3):591–605.
- Clague, J. 2000. A review of catastrophic drainage of moraine-dammed lakes in British Columbia. *Quaternary Science Reviews* 19 (17–18):1763–1783.
- Clague, J. J., C. Huggel, O. Korup, and B. McGuire. 2012. Climate change and hazardous processes in high mountains. *Revista de la Asociación Geológica Argentina* 69(3):328–338.
- Clarke, G. K. C., E. Berthier, C. G. Schoof, and A. H. Jarosch. 2009. Neural Networks Applied to Estimating Subglacial Topography and Glacier Volume. *Journal of Climate* 22 (8):2146–2160.
- Clarvis, M. H., S. Fatichi, A. Allan, J. Fuhrer, M. Stoffel, F. Romerio, L. Gaudard, P. Burlando, M. Beniston, E. Xoplaki, and A. Toreti. 2014. Governing and managing water resources under changing hydro-climatic contexts: The case of the upper Rhone basin. *Environmental Science & Policy* 43:56–67.
- Colonia, D., J. Torres, W. Haeberli, S. Schauwecker, E. Braendle, C. Giraldez, and A. Cochachin. 2017. Compiling an Inventory of Glacier-Bed Overdeepenings and Potential New Lakes in De-Glaciating Areas of the Peruvian Andes: Approach, First Results, and Perspectives for Adaptation to Climate Change. *Water* 9 (5):336.
- Comas-Bru, L., and F. McDermott. 2014. Impacts of the EA and SCA patterns on the European twentieth century NAO–winter climate relationship. *Quarterly Journal of the Royal Meteorological Society* 140 (679):354–363.
- Cuffey, K., and W. S. B. Paterson. 2010. *The physics of glaciers* 4th ed. Burlington, MA: Butterworth-Heinemann/Elsevier.

- Cutter, S. L. ed. 2001. *American hazardscapes: the regionalization of hazards and disasters*. Washington, D.C: Joseph Henry Press.
- Demiroglu, O. C., H. Dannevig, and C. Aall. 2018. Climate change acknowledgement and responses of summer (glacier) ski visitors in Norway. *Scandinavian Journal of Hospitality and Tourism* 18 (4):419–438.
- Emmer, A. 2017. Glacier Retreat and Glacial Lake Outburst Floods (GLOFs). In *Oxford Research Encyclopedia of Natural Hazard Science*. Oxford University Press.
- Enfield, D. B., A. M. Mestas-Nuñez, and P. J. Trimble. 2001. The Atlantic Multidecadal Oscillation and its relation to rainfall and river flows in the continental U.S. *Geophysical Research Letters* 28 (10):2077–2080.
- Farinotti, D., M. Huss, A. Bauder, and M. Funk. 2009a. An estimate of the glacier ice volume in the Swiss Alps. *Global and Planetary Change* 68 (3):225–231.
- Farinotti, D., M. Huss, A. Bauder, M. Funk, and M. Truffer. 2009b. A method to estimate the ice volume and ice-thickness distribution of alpine glaciers. *Journal of Glaciology* 55 (191):422–430.
- Fernández, A., and B. G. Mark. 2016. Modeling modern glacier response to climate changes along the Andes Cordillera: A multiscale review. *Journal of Advances in Modeling Earth Systems* 8 (1):467–495.
- Fischer, M., M. Huss, C. Barboux, and M. Hoelzle. 2014. The New Swiss Glacier Inventory SGI2010: Relevance of Using High-Resolution Source Data in Areas Dominated by Very Small Glaciers. *Arctic, Antarctic, and Alpine Research* 46 (4):933–945.
- Fischer, M., M. Huss, and M. Hoelzle. 2015. Surface elevation and mass changes of all Swiss glaciers 1980–2010. *The Cryosphere* 9 (2):525–540.
- Fountain, A. 2011. Temperate Glaciers. In *Encyclopedia of Snow, Ice and Glaciers*, eds. V. P. Singh, P. Singh, and U. K. Haritashya, 1145–1145. Dordrecht: Springer Netherlands.
- Fountain, A., C. F. Raymond, and M. Nakao. 2000. Debris-covered Glaciers: Proceedings of an International Workshop Held at the University of Washington in Seattle, Washington, USA, 13-15 September 2000. IAHS.
- Frey, H., W. Haeberli, A. Linsbauer, C. Huggel, and F. Paul. 2010. A multi-level strategy for anticipating future glacier lake formation and associated hazard potentials. *Natural Hazards and Earth System Science* 10 (2):339–352.
- Frey, H., and F. Paul. 2012. On the suitability of the SRTM DEM and ASTER GDEM for the compilation of topographic parameters in glacier inventories. *International Journal of Applied Earth Observation and Geoinformation* 18:480–490.

- Frey, H., H. Machguth, M. Huss, C. Huggel, S. Bajracharya, T. Bolch, A. Kulkarni, A. Linsbauer, N. Salzmann, and M. Stoffel. 2014. Estimating the volume of glaciers in the Himalayan-Karakoram region using different methods. *The Cryosphere* 8 (6):2313–2333.
- Fuchs, S., M. Keiler, S. Sokratov, and A. Shnyparkov. 2013. Spatiotemporal dynamics: the need for an innovative approach in mountain hazard risk management. *Natural Hazards* 68 (3):1217–1241.
- Fuchs, S., V. Röthlisberger, T. Thaler, A. Zischg, and M. Keiler. 2017. Natural Hazard Management from a Coevolutionary Perspective: Exposure and Policy Response in the European Alps. *Annals of the American Association of Geographers* 107 (2):382–392.
- Fyffe, C. L., B. W. Brock, M. P. Kirkbride, D. W. F. Mair, N. S. Arnold, C. Smiraglia, G. Diolaiuti, and F. Diotri. 2019. Do debris-covered glaciers demonstrate distinctive hydrological behaviour compared to clean glaciers? *Journal of Hydrology* 570:584–597.
- Gallina, V., S. Torresan, A. Critto, A. Sperotto, T. Glade, and A. Marcomini. 2016. A review of multi-risk methodologies for natural hazards: Consequences and challenges for a climate change impact assessment. *Journal of Environmental Management* 168:123–132.
- Gares, P. A., D. J. Sherman, and K. F. Nordstrom. 1994. Geomorphology and natural hazards. In *Geomorphology and Natural Hazards*, 1–18. Elsevier.
- Gill, J. C., and B. D. Malamud. 2014. Reviewing and visualizing the interactions of natural hazards: Interactions of Natural Hazards. *Reviews of Geophysics* 52 (4):680–722.
- . 2017. Anthropogenic processes, natural hazards, and interactions in a multi-hazard framework. *Earth-Science Reviews* 166:246–269.
- Goudie, A. S. 1996. Geomorphological “hotspots” and global warming. *Interdisciplinary Science Reviews* 21 (3):253–259.
- Haeberli, W., and M. Hoelzle. 1995. Application of inventory data for estimating characteristics of and regional climate-change effects on mountain glaciers: a pilot study with the European Alps. *Annals of Glaciology* 21:206–212.
- Haeberli, W., M. Hoelzle, F. Paul, and M. Zemp. 2007. Integrated monitoring of mountain glaciers as key indicators of global climate change: the European Alps. *Annals of Glaciology* 46:150–160.
- Haeberli, W., M. Buetler, C. Huggel, T. L. Friedli, Y. Schaub, and A. J. Schleiss. 2016. New lakes in deglaciating high-mountain regions – opportunities and risks. *Climatic Change* 139 (2): 201–214.
- Haeberli, W., M. Hoelzle, S. Suter, and World Glacier Monitoring Service eds. 1998. *Into the second century of worldwide glacier monitoring - prospects and strategies: a contribution to the International Hydrological Programme (IHP) and the Global Environment Monitoring System (GEMS)*. Paris: UNESCO.

- Hall, D. K., J. P. Ormsby, R. A. Bindschadler, and H. Siddalingaiah. 1987. Characterization of Snow and Ice Reflectance Zones on Glaciers Using Landsat Thematic Mapper Data. *Annals of Glaciology* 9:104–108.
- Hall, M. 1895. II.—Les Variations périodiques des Glaciers. Discours préliminaire. Par F. A. Forel, Président de la Commission Internationale des Glaciers. Archives des sciences physiques et naturelles. Genève. vol. xxxiv, p. 209. *Geological Magazine* 2 (12):569–570.
- Hall, R. J., and E. Hanna. 2018. North Atlantic circulation indices: links with summer and winter UK temperature and precipitation and implications for seasonal forecasting. *International Journal of Climatology* 38 (S1): e660–e677.
- Hanna, E., X. Fettweis, S. H. Mernild, J. Cappelen, M. H. Ribergaard, C. A. Shuman, K. Steffen, L. Wood, and T. L. Mote. 2014. Atmospheric and oceanic climate forcing of the exceptional Greenland ice sheet surface melt in summer 2012. *International Journal of Climatology* 34 (4):1022–1037.
- Hanna, E., T. E. Cropper, R. J. Hall, and J. Cappelen. 2016. Greenland Blocking Index 1851–2015: a regional climate change signal. *International Journal of Climatology* 36 (15):4847–4861.
- Harrison, S., J. S. Kargel, C. Huggel, J. Reynolds, D. H. Shugar, R. A. Betts, A. Emmer, N. Glasser, U. K. Haritashya, J. Klimeš, L. Reinhardt, Y. Schaub, A. Wiltshire, D. Regmi, and V. Vilímek. 2018. Climate change and the global pattern of moraine-dammed glacial lake outburst floods. *The Cryosphere* 12 (4):1195–1209.
- Hawkins, D. M. 2001. Fitting multiple change-point models to data. *Computational Statistics & Data Analysis* 37 (3):323–341.
- Helsel, D. R., and R. M. Hirsch. 1988. “Applicability of the t-Test for Detecting Trends in Water Quality Variables,” by Robert H. Montgomery and Jim C. Loftis. *JAWRA Journal of the American Water Resources Association* 24 (1):201–204.
- Holt, C. C. 2004. Forecasting seasonals and trends by exponentially weighted moving averages. *International Journal of Forecasting* 20 (1):5–10.
- Holzhauser, H.: Die bewegte Vergangenheit des Grossen Aletschgletschers, *Blätter aus der Walliser Geschichte* 41: 103–121.
- Huggel, C., A. Käab, W. Haerberli, and B. Krummenacher. 2003. Regional-scale GIS-models for assessment of hazards from glacier lake outbursts: evaluation and application in the Swiss Alps. *Natural Hazards and Earth System Science* 3 (6):647–662.
- Huggel, C., A. Käab, and N. Salzmann. 2004. GIS-based modeling of glacial hazards and their interactions using Landsat-TM and IKONOS imagery. *Norsk Geografisk Tidsskrift - Norwegian Journal of Geography* 58 (2):61–73.

- Hurrell, J. W. 1995. Decadal Trends in the North Atlantic Oscillation: Regional Temperatures and Precipitation. *Science* 269 (5224):676.
- Huss, M., and A. Bauder. 2009. 20th-century climate change inferred from four long-term point observations of seasonal mass balance. *Annals of Glaciology* 50 (50):207–214.
- Huss, M., R. Hock, A. Bauder, and M. Funk. 2010. 100-year mass changes in the Swiss Alps linked to the Atlantic Multidecadal Oscillation. *Geophysical Research Letters* 37 (10).
- Huss, M., S. Usselman, D. Farinotti, and A. Bauder. 2010. Glacier mass balance in the south-eastern Swiss Alps since 1900 and perspectives for the future. *ERDKUNDE* 2010 (2):119–140.
- Huss, M., L. Dhulst, and A. Bauder. 2015. New long-term mass-balance series for the Swiss Alps. *Journal of Glaciology* 61 (227):551–562.
- Huss, M., and M. Fischer. 2016. Sensitivity of Very Small Glaciers in the Swiss Alps to Future Climate Change. *Frontiers in Earth Science* 4.
- Hutchinson, M. F. 1989. A new procedure for gridding elevation and stream line data with automatic removal of spurious pits. *Journal of Hydrology* 106 (3–4):211–232.
- Ilyashuk, E. A., K. A. Koinig, O. Heiri, B. P. Ilyashuk, and R. Psenner. 2011. Holocene temperature variations at a high-altitude site in the Eastern Alps: a chironomid record from Schwarzsee ob Sölden, Austria. *Quaternary Science Reviews* 30 (1–2):176–191.
- Immerzeel, W. W., L. P. H. van Beek, and M. F. P. Bierkens. 2010. Climate Change Will Affect the Asian Water Towers. *Science* 328 (5984):1382.
- James, W. H. M., and J. L. Carrivick. 2016. Automated modelling of spatially-distributed glacier ice thickness and volume. *Computers & Geosciences* 92:90–103.
- Jawaid, M. 2017. Glacial lake flood hazard assessment and modelling: a GIS perspective. Lund University, Master Thesis.
- Jiskoot, H., C. J. Curran, D. L. Tessler, and L. R. Shenton. 2009. Changes in Clemenceau Icefield and Chaba Group glaciers, Canada, related to hypsometry, tributary detachment, length–slope and area–aspect relations. *Annals of Glaciology* 50 (53):133–143.
- Kaplan, A., M. A. Cane, Y. Kushnir, A. C. Clement, M. B. Blumenthal, and B. Rajagopalan. 1998. Analyses of global sea surface temperature 1856–1991. *Journal of Geophysical Research: Oceans* 103 (C9):18567–18589.
- Kappes, M. Keiler, and T. Glade. 2010. From single- to multi-hazard risk analyses: a concept addressing emerging challenges. In CERG Editions [database online]. Available from <http://www.dx.doi.org/10.7892/boris.71645>.

- Kappes, M.S., K. Gruber, S. Frigerio, R. Bell, M. Keiler, and T. Glade. 2012a. The MultiRISK platform: The technical concept and application of a regional-scale multihazard exposure analysis tool. *Geomorphology* 151–152:139–155.
- Kappes, M. S., M. Keiler, K. von Elverfeldt, and T. Glade. 2012b. Challenges of analyzing multi-hazard risk: a review. *Natural Hazards* 64 (2):1925–1958.
- Karimi, N., A. Farokhnia, L. Karimi, M. Eftekhari, and H. Ghalkhani. 2012. Combining optical and thermal remote sensing data for mapping debris-covered glaciers (Alamkouh Glaciers, Iran). *Cold Regions Science and Technology* 71:73–83.
- Keiler, M., J. Knight, and S. Harrison. 2010. Climate change and geomorphological hazards in the eastern European Alps. *Philosophical Transactions of the Royal Society A: Mathematical, Physical and Engineering Sciences* 368 (1919):2461–2479.
- Kirby, A. ed. 1990. Human Dimensions of Environmental Hazards: Complexity, Disparity, and the Search for Guidance. In *Nothing to fear: risks and hazards in American society*. Tucson, Ariz: University of Arizona Press.
- Kleiber, C., and A. Zeileis. 2008. *Applied Econometrics with R*. New York: Springer.
- Klimeš, J., J. Novotný, I. Novotná, B. J. de Urries, V. Vilímek, A. Emmer, T. Strozzi, M. Kusák, A. C. Rapre, F. Hartvich, and H. Frey. 2016. Landslides in moraines as triggers of glacial lake outburst floods: example from Palcacocha Lake (Cordillera Blanca, Peru). *Landslides* 13 (6):1461–1477.
- Klok, E. J., and J. Oerlemans. 2002. Model study of the spatial distribution of the energy and mass balance of Morteratschgletscher, Switzerland. *Journal of Glaciology* 48 (163):505–518.
- Knight, J. R., C. K. Folland, and A. A. Scaife. 2006. Climate impacts of the Atlantic Multidecadal Oscillation. *Geophysical Research Letters* 33 (17): L17706.
- Koenig, U., and B. Abegg. 1997. Impacts of Climate Change on Winter Tourism in the Swiss Alps. *Journal of Sustainable Tourism* 5 (1):46–58.
- Kropáček, J., N. Neckel, and A. Bauder. 2014. Estimation of Mass Balance of the Grosser Aletschgletscher, Swiss Alps, from ICESat Laser Altimetry Data and Digital Elevation Models. *Remote Sensing* 6 (6):5614–5632.
- Kuan, C.-M., and K. Hornik. 1995. The generalized fluctuation test: A unifying view. *Econometric Reviews* 14 (2):135–161.
- Li, H., F. Ng, Z. Li, D. Qin, and G. Cheng. 2012. An extended “perfect-plasticity” method for estimating ice thickness along the flow line of mountain glaciers: Ice Thickness Estimation. *Journal of Geophysical Research: Earth Surface* 117 (F1).

- Linsbauer, A; F. Paul; M. Hoelzle; H. Frey; and W. Haeberli. 2009. *The Swiss Alps without glaciers – a GIS-based modelling approach for reconstruction of glacier beds*. In: Purves, Ross S; et al. Proceedings of Geomorphometry 2009. Zurich, CH: Department of Geography, University of Zurich, 243-247.
- Linsbauer, A., F. Paul, and W. Haeberli. 2012. Modeling glacier thickness distribution and bed topography over entire mountain ranges with GlabTop: Application of a fast and robust approach: Regional-Scale Modeling of Glacier Beds. *Journal of Geophysical Research: Earth Surface* 117 (F3).
- Linsbauer, A., F. Paul, H. Machguth, and W. Haeberli. 2013. Comparing three different methods to model scenarios of future glacier change in the Swiss Alps. *Annals of Glaciology* 54 (63):241–253.
- Linsbauer, A., H. Frey, W. Haeberli, H. Machguth, M. F. Azam, and S. Allen. 2016. Modelling glacier-bed overdeepenings and possible future lakes for the glaciers in the Himalaya—Karakoram region. *Annals of Glaciology* 57 (71):119–130.
- Liu, B., Y. L. Siu, and G. Mitchell. 2016. Hazard interaction analysis for multi-hazard risk assessment: a systematic classification based on hazard-forming environment. *Natural Hazards and Earth System Sciences* 16 (2):629–642.
- LP DAAC - NASA and METI Release ASTER Global DEM Version 3.  
<https://lpdaac.usgs.gov/news/nasa-and-meti-release-aster-global-dem-version-3/> (last accessed 21 November 2019).
- Maanya, U. S., A. V. Kulkarni, A. Tiwari, E. D. Bhar, and J. Srinivasan. 2016. Identification of Potential Glacial Lake Sites and Mapping Maximum Extent of Existing Glacier Lakes in Drang Drung and Samudra Tapu Glaciers, Indian Himalaya. *Current Science* 111 (3):553.
- Maia, A. L. S., and F. de A. T. de Carvalho. 2011. Holt’s exponential smoothing and neural network models for forecasting interval-valued time series. *International Journal of Forecasting* 27 (3):740–759.
- Maisch, M. and W. Haeberli. 1982. Interpretation geometrischer parameter von Spätglazialgletschern im Gebiet Mittelbünden, Schweizer Alpen. *Physische Geographie Universität Zürich*, 1, 111-126.
- Maisch, M., et al. 2000. Die Gletscher der Schweizer Alpen. Gletscherhochstand 1850, Aktuelle Vergletscherung, Gletscherschwund-Szenarien. Zurich: vdf Hochschulverlag.
- Malanson, G. P., D. R. Butler, and K. P. Georgakakos. 1992. Nonequilibrium geomorphic processes and deterministic chaos. *Geomorphology* 5 (3–5):311–322.
- Marzeion, B., and A. Nesje. 2012. Spatial patterns of North Atlantic Oscillation influence on mass balance variability of European glaciers. *The Cryosphere* 6 (3):661–673.

- Marzeion, B., J. G. Cogley, K. Richter, and D. Parkes. 2014. Attribution of global glacier mass loss to anthropogenic and natural causes. *Science* 345 (6199):919–921.
- McCabe, G. J., A. G. Fountain, and M. Dyurgerov. 2000. Variability in Winter Mass Balance of Northern Hemisphere Glaciers and Relations with Atmospheric Circulation. *Arctic, Antarctic, and Alpine Research* 32 (1):64–72.
- Medwedeff, W. G., and G. H. Roe. 2017. Trends and variability in the global dataset of glacier mass balance. *Climate Dynamics* 48 (9):3085–3097.
- Mergili, M., J.-T. Fischer, J. Krenn, and S. P. Pudasaini. 2017. r.avaflow v1, an advanced open-source computational framework for the propagation and interaction of two-phase mass flows. *Geoscientific Model Development* 10 (2):553–569.
- MeteoSwiss. Precipitation and temperature. <https://www.meteoswiss.admin.ch/home/climate/swiss-climate-in-detail/extreme-value-analyses/high-impact-precipitation-events/9-13-august-2002/precipitation-and-temperature.html?query=RhiresM&topic=0&pageIndex=0> (last accessed 21 November 2019).
- Miller, J. D., W. W. Immerzeel, and G. Rees. 2012. Climate Change Impacts on Glacier Hydrology and River Discharge in the Hindu Kush–Himalayas: A Synthesis of the Scientific Basis. *Mountain Research and Development* 32 (4):461–467.
- Milner, A. M., K. Khamis, T. J. Battin, J. E. Brittain, N. E. Barrand, L. Füreder, S. Cauvy-Fraunié, G. M. Gíslason, D. Jacobsen, D. M. Hannah, A. J. Hodson, E. Hood, V. Lencioni, J. S. Ólafsson, C. T. Robinson, M. Tranter, and L. E. Brown. 2017. Glacier shrinkage driving global changes in downstream systems. *Proceedings of the National Academy of Sciences* 114 (37): 9770–9778.
- Montz, B. E., and G. A. Tobin. 2011. Natural hazards: An evolving tradition in applied geography. *Applied Geography* 31 (1):1–4.
- Möri, A., and M. Wiederkehr. 2013. SwissALTI<sup>3D</sup>: a new tool for geological mapping. *Swiss Bulletin for Applied Geology* 18 (1):61–69.
- Müller, F. 1962. Zonation in the Accumulation Area of the Glaciers of Axel Heiberg Island, N.W.T., Canada. *Journal of Glaciology* 4 (33):302–311.
- Müller, F., Caflisch, G., and Müller, G. 1976. Firn und Eis der Schweizer Alpen, Gletscherinventar. Zurich: ETH Zurich, Publication, 57, 57a.
- Naegeli, K., and M. Huss. 2017. Sensitivity of mountain glacier mass balance to changes in bare-ice albedo. *Annals of Glaciology* 58 (75pt2):119–129.
- Naegeli, K., M. Huss, and M. Hoelzle. 2019. Change detection of bare-ice albedo in the Swiss Alps. *The Cryosphere* 13 (1):397–412.

- Nicholson, L. I., M. McCarthy, H. D. Pritchard, and I. Willis. 2018. Supraglacial debris thickness variability: impact on ablation and relation to terrain properties. *The Cryosphere* 12 (12):3719–3734.
- Oerlemans, J., B. Anderson, A. Hubbard, P. Huybrechts, T. Jóhannesson, W. H. Knap, M. Schmeits, A. P. Stroeven, R. S. W. van de Wal, J. Wallinga, and Z. Zuo. 1998. Modelling the response of glaciers to climate warming. *Climate Dynamics* 14 (4):267–274.
- Oerlemans, J., and B. K. Reichert. 2000. Relating glacier mass balance to meteorological data by using a seasonal sensitivity characteristic. *Journal of Glaciology* 46 (152):1–6.
- Oguchi, T., and D. R. Butler. 2017. Geomorphic Systems. In *International Encyclopedia of Geography: People, the Earth, Environment and Technology*, eds. D. Richardson, N. Castree, M. F. Goodchild, A. Kobayashi, W. Liu, and R. A. Marston, 1–5. Oxford, UK: John Wiley & Sons, Ltd.
- Ohmura, A. 2011. Observed Mass Balance of Mountain Glaciers and Greenland Ice Sheet in the 20th Century and the Present Trends. *Surveys in Geophysics* 32 (4–5):537–554.
- Paul, F., A. Kääb, M. Maisch, T. Kellenberger, and W. Haeberli. 2002. The new remote-sensing-derived Swiss glacier inventory: I. Methods. *Annals of Glaciology* 34:355–361.
- Paul, F., A. Kääb, M. Maisch, and W. Haeberli. 2008. *The new Swiss glacier inventory 2000*. In: Herren, E. R. *The Swiss Glaciers 2001/2002 and 2002/2003*. Zürich: Schweizerisches Gletschermessnetz, 51-58.
- Petrakov, D., A. Shpuntova, A. Aleinikov, A. Kääb, S. Kutuzov, I. Lavrentiev, M. Stoffel, O. Tutubalina, and R. Usubaliev. 2016. Accelerated glacier shrinkage in the Ak-Shyrak massif, Inner Tien Shan, during 2003–2013. *Science of The Total Environment* 562:364–378.
- Phillips, J. D. 1992. Nonlinear dynamical systems in geomorphology: revolution or evolution? *Geomorphology* 5 (3–5):219–229.
- . 2003. Sources of nonlinearity and complexity in geomorphic systems. *Progress in Physical Geography: Earth and Environment* 27 (1):1–23.
- Piot, M. 2017. Wirtschaftlichkeit der Wasserkraft in der Schweiz. *Wasserwirtschaft* 107 (1):33–38.
- Ploberger, W., and W. Krämer. 1992. The Cusum Test with Ols Residuals. *Econometrica* 60 (2):271–285.

Rabatel, A., B. Francou, A. Soruco, J. Gomez, B. Cáceres, J. L. Ceballos, R. Basantes, M. Vuille, J.-E. Sicart, C. Huggel, M. Scheel, Y. Lejeune, Y. Arnaud, M. Collet, T. Condom, G. Consoli, V. Favier, V. Jomelli, R. Galarraga, P. Ginot, L. Maisincho, J. Mendoza, M. Ménégoz, E. Ramirez, P. Ribstein, W. Suarez, M. Villacis, and P. Wagnon. 2013. Current state of glaciers in the tropical Andes: a multi-century perspective on glacier evolution and climate change. *The Cryosphere* 7 (1):81–102.

Rahman, K., A. G. da Silva, E. M. Tejada, A. Gobiet, M. Beniston, and A. Lehmann. 2015. An independent and combined effect analysis of land use and climate change in the upper Rhone River watershed, Switzerland. *Applied Geography* 63:264–272.

Rango, A. S. 1975. Employment of satellite snowcover observations for improving seasonal runoff estimates. [Indus River and Wind River Range, Wyoming]. <https://ntrs.nasa.gov/search.jsp?R=19760009485> (last accessed 17 November 2019).

Ranzi, R., G. Grossi, L. Iacovelli, and S. Taschner. 2004. Use of multispectral ASTER images for mapping debris-covered glaciers within the GLIMS project. In *IEEE International IEEE International IEEE International Geoscience and Remote Sensing Symposium, 2004. IGARSS '04. Proceedings. 2004*, 1144–1147. Anchorage, AK, USA: IEEE.

Rasul, G., and D. Molden. 2019. The Global Social and Economic Consequences of Mountain Cryospheric Change. *Frontiers in Environmental Science* 7:91.

Reid, T. D., and B. W. Brock. 2010. An energy-balance model for debris-covered glaciers including heat conduction through the debris layer. *Journal of Glaciology* 56 (199):903–916.

Rosenfeld, C. L. 1994. The geomorphological dimensions of natural disasters. *Geomorphology* 10 (1–4):27–36.

Rottler, E., C. Kormann, T. Francke, and A. Bronstert. 2019. Elevation-dependent warming in the Swiss Alps 1981–2017: Features, forcings and feedbacks. *International Journal of Climatology* 39 (5):2556–2568.

Schaub, Y. 2015. Outburst Floods from High-Mountain Lakes: Risk Analysis of Cascading Processes under Present and Future Conditions. University of Zurich, PhD Dissertation.

Scheidegger, A. E. 1992. Limitations of the system approach in geomorphology. *Geomorphology* 5 (3–5):213–217.

Scherrer, S., and C. Appenzeller. 2006. Swiss Alpine snow pack variability: major patterns and links to local climate and large-scale flow. *Climate Research* 32:187–199.

Schleiss, A., and F. Oberrauch. 2014. Flexibilisierung der Wasserkraft in der Schweiz für zukünftige Aufgaben im internationalen Strommarkt. *Wasser Energie Luft* 106 (3):175–178.

- Schwarb, M. 2001. The Alpine Precipitation Climate. Evaluation of a High-Resolution Analysis Scheme Using Comprehensive Rain-Gauge Data, *Zuercher Klimaschriften* 80.
- Shahgedanova, M. 2005. Interactions between mass balance, atmospheric circulation, and recent climate change on the Djankuat Glacier, Caucasus Mountains, Russia. *Journal of Geophysical Research* 110 (D4): D04108.
- Short Sr., N. M. 1999. “The Remote Sensing Tutorial: Section 1. Contrast Stretching and Density Slicing.” Online tutorial book. <http://facegis.nuarsa.info/?id=133>
- Slaymaker, O. ed. 1996. *Geomorphic hazards*. Chichester; New York: Wiley.
- Small, E. E. 1995. Hypsometric forcing of stagnant ice margins: Pleistocene valley glaciers, San Juan Mountains, Colorado. *Geomorphology* 14 (2):109–121.
- Spandre, P., H. François, D. Verfaillie, M. Lafaysse, M. Déqué, N. Eckert, E. George, and S. Morin. 2019. Climate controls on snow reliability in French Alps ski resorts. *Scientific Reports* 9 (1):8043.
- Spandre, P., H. François, D. Verfaillie, M. Pons, M. Vernay, M. Lafaysse, E. George, and S. Morin. 2018. Winter tourism and climate change in the Pyrenees and the French Alps: relevance of snowmaking as a technical adaptation. *The Cryosphere Discussions* :1–36.
- Stoffel, M., and C. Huggel. 2012. Effects of climate change on mass movements in mountain environments. *Progress in Physical Geography: Earth and Environment* 36 (3):421–439.
- Stoffel, M., D. Tiranti, and C. Huggel. 2014. Climate change impacts on mass movements — Case studies from the European Alps. *Science of The Total Environment* 493:1255–1266.
- Sullivan, J. H. 2002. Estimating the Locations of Multiple Change Points in the Mean. *Computational Statistics* 17 (2):289–296.
- swisstopo Online Shop.  
[https://shop.swisstopo.admin.ch/en/products/height\\_models/alti3D](https://shop.swisstopo.admin.ch/en/products/height_models/alti3D) (last accessed 21 November 2019).
- Temme, A. J. A. M., M. Keiler, D. Karssenber, and A. Lang. 2015. Complexity and non-linearity in earth surface processes - concepts, methods and applications: Complexity and Non-Linearity. *Earth Surface Processes and Landforms* 40 (9):1270–1274.
- Thibert, E., N. Eckert, and C. Vincent. 2013. Climatic drivers of seasonal glacier mass balances: an analysis of 6 decades at Glacier de Sarennes (French Alps). *The Cryosphere* 7 (1):47–66.

Thibert, E., P. Dkengne Sielenou, V. Vionnet, N. Eckert, and C. Vincent. 2018. Causes of Glacier Melt Extremes in the Alps Since 1949. *Geophysical Research Letters* 45 (2):817–825.

US Department of Commerce, N. ESRL Global Monitoring Division - Global Greenhouse Gas Reference Network. <https://www.esrl.noaa.gov/gmd/ccgg/trends/> (last accessed 9 November 2019).

Vacco, D. A., R. B. Alley, D. Pollard, and D. B. Reusch. 2010. Numerical modeling of valley glacier stagnation as a paleoclimatic indicator. *Quaternary Research* 73 (2):403–409.

Van Westen, C. J. 2013. 3.10 Remote Sensing and GIS for Natural Hazards Assessment and Disaster Risk Management. In *Treatise on Geomorphology*, 259–298. Elsevier.

Vavrus, S. 2007. The role of terrestrial snow cover in the climate system. *Climate Dynamics* 29 (1):73–88.

Vilímek, V., A. Emmer, C. Huggel, Y. Schaub, and S. Würmli. 2014. Database of glacial lake outburst floods (GLOFs)–IPL project No. 179. *Landslides* 11 (1):161–165.

Vincent, C. 2002. Influence of climate change over the 20th Century on four French glacier mass balances. *Journal of Geophysical Research* 107 (D19):4375.

Wallace, J. M., and D. S. Gutzler. 1981. Teleconnections in the Geopotential Height Field during the Northern Hemisphere Winter. *Monthly Weather Review* 109 (4):784–812.

Wang, X., F. Siegert, A. Zhou, and J. Franke. 2013. Glacier and glacial lake changes and their relationship in the context of climate change, Central Tibetan Plateau 1972–2010. *Global and Planetary Change* 111:246–257.

Watanabe, T., J. D. Ives, and J. E. Hammond. 1994. Rapid Growth of a Glacial Lake in Khumbu Himal, Himalaya: Prospects for a Catastrophic Flood. *Mountain Research and Development* 14 (4):329–340.

White, G. F. 1974. *Natural hazards, local, national, global*. New York: Oxford University Press.

Williams, R. S., D. K. Hall, and C. S. Benson. 1991. Analysis of glacier facies using satellite techniques. *Journal of Glaciology* 37 (125):120–128.

World Development Report 2010: Development and Climate Change. <https://openknowledge.worldbank.org/handle/10986/4387> (last accessed 16 November 2019).

World Glacier Monitoring Service (WGMS). 2017. Fluctuations of Glaciers Database. [http://wgms.ch/data\\_databaseversions/](http://wgms.ch/data_databaseversions/) (last accessed 17 September 2019).

Woul, M. D., and R. Hock. 2005. Static mass-balance sensitivity of Arctic glaciers and ice caps using a degree-day approach. *Annals of Glaciology* 42:217–224.

Zeileis, A. 2004. Alternative boundaries for CUSUM tests. *Statistical Papers* 45 (1):123–131.

Zeileis, A., C. Kleiber, W. Krämer, and K. Hornik. 2003. Testing and dating of structural changes in practice. *Computational Statistics & Data Analysis* 44 (1–2):109–123.

Zemp, M., W. Haeberli, M. Hoelzle, and F. Paul. 2006. Alpine glaciers to disappear within decades? *Geophysical Research Letters* 33 (13): L13504.

Zemp, M., H. Frey, I. Gärtner-Roer, S. U. Nussbaumer, M. Hoelzle, F. Paul, W. Haeberli, F. Denzinger, A. P. Ahlstrøm, B. Anderson, S. Bajracharya, C. Baroni, L. N. Braun, B. E. Cáceres, G. Casassa, G. Cobos, L. R. Dávila, H. Delgado Granados, M. N. Demuth, L. Espizua, A. Fischer, K. Fujita, B. Gadek, A. Ghazanfar, J. Ove Hagen, P. Holmlund, N. Karimi, Z. Li, M. Pelto, P. Pitte, V. V. Popovnin, C. A. Portocarrero, R. Prinz, C. V. Sangewar, I. Severskiy, O. Sigurdsson, A. Soruco, R. Usubaliev, and C. Vincent. 2015. Historically unprecedented global glacier decline in the early 21st century. *Journal of Glaciology* 61 (228):745–762.

Zhu, M., T. Yao, W. Yang, B. Xu, G. Wu, and X. Wang. 2018. Differences in mass balance behavior for three glaciers from different climatic regions on the Tibetan Plateau. *Climate Dynamics* 50 (9–10):3457–3484.